

**Computational Fluid Dynamics Simulations of Fully Developed Turbulent Flows
with Newtonian and non-Newtonian Drag Reduction Fluids in the Cylindrical
Geometry**

by

© Xiao Xiong

A Thesis submitted to the School of Graduate Studies in partial fulfillment of
requirements for the degree of

Doctor of Philosophy

Faculty of Engineering and Applied Science

Memorial University of Newfoundland

October 2020

St. John's Newfoundland and Labrador

Acknowledgments

Above all, I would like to express my highest appreciation for my two supervisors, Dr. Mohammad Azizur Rahman and Dr. Yan Zhang, for providing me the opportunity to strive for a Ph.D. degree. Both of them offered me the best advice along the way, without which I will never complete this thesis.

I would also like to express my acknowledgment to Dr. Xin Zhang and Dr. Xili Duan from the Department of Mechanical Engineering, with whom I had very constructive discussions while completing chapter 5 of this thesis, and Dr. Jahrul Alam from the Department of Mathematics and Statistics, who is always helpful whenever approached to for suggestions.

Finally, I am thankful for my wife, Chun, and my parents, who provide me endless support throughout my study.

You truly become stronger on giants' shoulders.

Abstract

While turbulent flows with the dynamic and sinuous flow pattern have a wide variety of engineering applications in enhancing fluid mixing and heat/mass transfer, they unfavorably lead to dramatic increases in friction drags that need to be eased.

The polymer induced drag reduction, first discovered by Toms in 1948, is one of the most efficient techniques to achieve so, which has the capability of reducing the friction drag in turbulent flows by up to 80%. As a result, it has been broadly used for anti-corrosion in oil and gas conduits, energy loss prevention in irrigation, water heating/cooling systems and sewer systems, improving hydraulic fracturing in reservoir engineering, and enhancing cutting transport for extended-reach well in drilling engineering.

Despite being studied for over 70 years, many problems in this research area are still waiting to be solved. In particular, to accurately predict drag reduction numerically remains challenging, especially in engineering problems where flows with large Reynolds numbers in complex geometries widely exist.

Consequently, in this study, a reliable numerical approach has been proposed in the computationally inexpensive Reynolds-averaged-Navier-Stokes (RANS) framework to estimate polymer induced drag reduction in the cylindrical geometry, with the rheological behavior of polymer solutions represented by the finitely-extensible-nonlinear-elastic model with Peterlin's function (FENE-P model) and the turbulent flow field characterized by the $k-\varepsilon-\overline{v^2}-f$ model, both coded into the commercial software of FLUENT using the User-Defined-Function (UDF).

ANSYS 14.0 is used to complete all the simulations, CFX for the base case Newtonian flow and FLUENT for the drag reduction flow. By using the correlations suggested in this study to determine the essential rheological parameters, simulation results are validated successfully against experimental studies, showing the robust performance of the proposed model to predict accurate drag reduction in the cylindrical geometry for solutions with both rigid and non-rigid flexible polymers.

By comparing behaviors of the non-Newtonian drag reduction and the Newtonian fluids in the concentric annulus, where the geometrical transverse curvature effect plays a vital role in determining the flow field, polymers are found to behave differently close to the inner and outer walls of the annulus, leading to more decay of turbulence at the outer wall than the inner. Such a phenomenon has been explained by relating the elongation of the polymer chains in the solution to the intensity of the flow field they experience, which is also found in this study to be highly dependent on the inherent rheological properties of themselves.

This thesis provides a benchmark study about how the polymer induced turbulent drag reduction in the cylindrical geometry can be numerically estimated using RANS modelling. Substantial progress has also been made in understanding the geometry-dependent behavior of polymers in the turbulent flow, which could inspire research on broader applications of the polymer induced drag reduction in more complex geometries.

Contents

Acknowledgments	i
Abstract	ii
List of Figures.....	viii
List of Tables	x
List of Symbols	xi
Chapter 1 Introduction.....	1
1.1 Background	1
1.2 Research Objectives.....	4
1.3 Organization of the Thesis	5
1.4 References.....	6
Chapter 2 Literature Review	11
2.1 Turbulent Newtonian Flow	11
2.1.1 Experimental Investigation of Newtonian Fluid.....	11
2.1.2 DNS Investigation of Newtonian Fluid	12
2.1.3 RANS Modelling of Newtonian Fluid.....	13
2.2 Turbulent Drag Reduction Flow	19
2.2.1 Experimental Investigations of Drag Reduction Fluid	19
2.2.2 DNS Investigation of Drag Reduction Fluid Using FENE-P Model ...	21
2.2.3 RANS Modelling of Drag Reduction Fluid Using FENE-P Model.....	22
2.3 References.....	24

Chapter 3 RANS Based CFD Simulation of Fully Developed Turbulent

Newtonian Flow in Concentric Annuli.....34

3.1	Introduction.....	35
3.2	Numerical Procedures	38
3.2.1	Governing Equations	38
3.2.2	Problem Setup.....	43
3.3	Results and Discussions.....	45
3.3.1	Average Axial Velocity	45
3.3.2	Reynolds Stress.....	49
3.3.3	Locations of Maximum Axial Velocity and Zero Reynolds Stress	53
3.3.4	Turbulent Kinetic Energy Budget.....	54
3.4	Conclusions.....	62
3.5	References.....	63

Chapter 4 RANS Simulation of Non-Newtonian Drag Reduction Fluid in Horizontal Concentric Annulus Using the Power Law Model67

4.1	Introduction.....	68
4.2	Numerical Procedures	70
4.2.1	Governing Equations	70
4.2.2	Power Law Model.....	72
4.2.3	Problem Setups	73
4.3	Results and Discussions.....	74
4.3.1	Pressure Drop.....	74

4.3.2	Average Axial Velocity	76
4.3.3	Reynolds Stress	77
4.3.4	Correlation between α_1 and Polymer Concentration.....	81
4.4	Conclusions.....	82
4.5	References.....	83
Chapter 5 Estimation of the Drag Reduction for Fully Developed Turbulent Flow in Cylindrical Geometries Using RANS Modelling with the FENE-P Model		86
5.1	Introduction.....	86
5.2	Numerical Models.....	88
5.2.1	Governing Equations	88
5.2.2	Constitutive model: FENE-P model:	89
5.2.3	Turbulence model: modified $k-\varepsilon-\overline{v^2}$ -f model.....	93
5.2.4	Numerical Method	95
5.3	Model Validation and Discussions.....	97
5.4	Conclusions.....	102
5.5	References.....	103
Chapter 6 Reynolds-averaged Simulation of the Fully Developed Turbulent Drag Reduction Flow in Concentric Annuli Using the FENE-P Model		109
6.1	Introduction.....	110
6.2	Numerical Models.....	114
6.3	Results and Discussions.....	116
6.3.1	Mean Velocity profiles	120

6.3.2	Reynolds Stress.....	122
6.3.3	Turbulent Kinetic Energy Budget.....	128
6.4	Conclusions.....	131
6.5	References.....	133
Chapter 7	Summary of Thesis and Future Works.....	136
7.1	Summary.....	136
7.2	Future Works.....	138
7.3	List of Publications.....	140
7.4	References.....	140

List of Figures

Fig. 3-1 Scheme of Test Geometry and Coordinate System	43
Fig. 3-2 Mesh Independence Test.....	44
Fig. 3-3 Axial Velocity at the Wall	47
Fig. 3-4 Axial Velocity for Different θ	47
Fig. 3-5 Axial Velocity for at Different Re.....	48
Fig. 3-6 Reynolds Stress Distribution with Various Reynolds Numbers and Radius Ratios	49
Fig. 3-7 CFD results of Near-wall Reynolds Stresses for Different Reynolds Numbers.....	50
Fig. 3-8 Locations of Maximum Axial Velocity and Zero Reynolds Stress for Different Re	52
Fig. 3-9 Locations of Maximum Axial Velocity and Zero Reynolds Stress for Different θ	53
Fig. 3-10 Shear Production for $\theta = 0.5$ Compared with Pipe Flow	55
Fig. 3- 11 Shear Production Term for Different θ and Re.....	56
Fig. 3-12 Viscous Dissipation Term for Different Re	58
Fig. 3-13 Turbulent Kinetic Energy Budget for $\theta = 0.5$ and $Re = 8900$	60
Fig. 3-14 Average Vorticities for $\theta = 0.4$ and $Re = 38700$	61
Fig. 4-1 Reynolds Stress for Water	73
Fig. 4-2 Pressure Drop for Different Test Cases	76

Fig. 4-3 Axial Velocity for Different Solutions at $m=3.92$ kg/s with Modified Model	
Constants	77
Fig. 4-4 Reynolds Stresses for 0.07% Fluid at $m=3.92$ kg/s.....	78
Fig. 4-5 Reynolds Stress for at $m=3.93$ kg/s for Different Polymer Concentrations	
.....	80
Fig. 4-6 Relation between α_1 and Polymer Concentration	81
Fig. 5-1 Scheme of the Flow Coordinate	96
Fig. 5-2 Mesh in the Wall-normal Direction	96
Fig. 5-3 Comparison of DR between Numerical Prediction and Experimental Study	
	99
Fig. 6-1 Scheme and Mesh of the Flow Domain.....	115
Fig. 6-2 Validation of Current Simulation Results towards DNS at Different DR.....	118
Fig. 6-3 Comparison of TKE and $\overline{v^2}$ with Different DR	119
Fig. 6-4 Comparison of Near-wall Velocity Profiles with and without Polymer	
Additives.....	121
Fig. 6-5 Comparison of Near-wall Velocity Profiles at $L=30$	122
Fig. 6-6 Comparison of Near-wall Velocity Profiles at $L=100$	123
Fig. 6-7 Comparison of Reynolds Stress Profiles at $L=30$	125
Fig. 6-8 Comparison of Reynolds Stress Profiles at $L=100$	126
Fig. 6-9 Comparison of TKE Budgets	130

List of Tables

Table 3-1 Coefficients in the SST model	40
Table 3-2 Mean Flow Parameters.....	46
Table 4-1 Default Model Coefficients.....	72
Table 4-2 Control Factors for Different Test Cases.....	74
Table 4-3 Pressure Drop by Only Power Law Model at Constant Mass Flow Rate	75
Table 4-4 Pressure Drop by Only Power Law with Constant Polymer Concentration	75
Table 5-1 Coefficients of Turbulence model.....	95
Table 5-2 Detail of Polymer Solution used for Validations.....	98
Table 6-1 Mesh Independence Test.....	115
Table 6-2 Summary of Flow Parameters.....	117

List of Symbols

a	flow consistency index the power-law model, $Pa \cdot s^b$
b	flow behavior index in the power-law model, (-)
C_{ij}, c_{ij}	time-averaged and fluctuating components of polymer conformation tensor, respectively, (-)
C_f	skin friction coefficient, (-)
D_{in}, D_{out}, D_h	inner, outer, and hydraulic diameter of the annulus, m
f	turbulence redistribution function, (-)
F_1, F_2	blending functions in the SST model
$F^p, F(C_{nn})$	time-averaged component of the Peterlin's function, (-)
$f^p, f(C_{nn})$	time-fluctuating component of the Peterlin's function, (-)
G, G', G''	elasticity, loss modulus, and storage modulus of the rigid polymers, Pa
k	turbulent kinetic energy, m^2/s^2
k_b	Boltzman constant, $m^2kg/(s^2K)$
K_p	dimensionless pressure gradient, (-)
l_m	turbulent mixing length, m
L	dimensionless maximum elongation length of polymers, (-)
L_t	turbulent length scale, m

n	number of polymers per unit volume in the polymer solution, (-)
\hat{P}, P	Turbulent and time-averaged pressure, respectively, Pa
P_k	production of turbulent kinetic energy, m^2/s^3
\widetilde{P}_k	modified production of turbulent kinetic energy, m^2/s^3
R_1, R_2	inner and outer radius of the annulus, respectively, m
r_{in}, r_{out}, r_0	locations of inner wall, outer wall and zero shear stress in the wall-normal direction in the annulus, m
Re	Reynolds number based on bulk mean velocity, (-)
Re_h	Reynolds number based on hydraulic diameter and bulk flow velocity of the annulus, (-)
Re_τ	Reynolds number based on frictional velocity, (-)
S	average shear strain rate, $1/s$
S_{ij}, s_{ij}	shear strain tensor for time-average and time-fluctuating velocity field, respectively, $1/s$
T_t	Turbulent time scale, s
U, U	vector and magnitude of time-averaged velocity, m/s
\hat{U}	vector of time-dependent turbulent velocity, m/s
U_x, U_y, U_z	time-averaged velocities in x , y , and z directions, respectively, in the Cartesian coordinate m/s
U_z, U_r, U_θ	time-averaged velocity in the streamwise, wall-normal, and spanwise direction, in the cylindrical coordinate, m/s

U_b	bulk mean velocity, m/s
u_x, u_y, u_z	time-fluctuating velocities in x , y , and z directions, respectively, m/s
u_τ, U_τ	frictional velocity, m/s
u^*, u_t, u_t', u_t''	modified velocities in near-wall treatment, m/s
$\overline{v^2}$	wall-normal fluctuating velocity variance, m^2/s^2
We	dimensionless Weissenberg number, (-)
y	distance from the nearest wall in wall-bounded flow, m

Greeks

β	viscosity ratio $\beta = \mu_s/\mu_0$, (-)
δ_{ij}	Kronecker delta function, (-)
ε	viscous dissipation of turbulent kinetic energy, m^2/s^3
λ	polymer relaxation time, s
μ, μ_s	dynamic viscosity of water, $Pa \cdot s$
μ_p	polymetric viscosity, $Pa \cdot s$
$\mu_{t,p}$	viscoelastic eddy viscosity, $Pa \cdot s$
μ_0	dynamic viscosity of solution at zero stress, $Pa \cdot s$
ν, ν_s	kinetic viscosity water, m^2/s
$\nu_t = \frac{\mu_t}{\rho}$	eddy viscosity, m^2/s
ω	turbulent eddy frequency, $1/s$
$\omega^*, \omega', \omega''$	modified turbulent eddy frequency in near-wall treatment, $1/s$

ρ	density, kg/m^3
τ	total shear stress, Pa
$\tau_p, \tau_{ij,p}$	shear stress tensor contributed by polymers, Pa
$\tau_s, \tau_{ij,s}$	shear stress tensor contributed by Newtonian solvent, Pa
τ_w	average wall shear stress, Pa
θ	ratio between inner and outer radius, (-)
$\hat{\phi}_i, \phi_i, \varphi_i$	turbulent, time-averaged and fluctuating variables in the RANS model, respectively
\emptyset	the shape factor of the annulus, (-)
ξ	distance between the inner and outer wall of the annulus,
	m
Ω_{ij}	average vorticity, $1/s$

Chapter 1 Introduction

1.1 Background

Most of the flow phenomena that are important to modern technology involve turbulence. The fundamental difference between the turbulent and laminar flows, first observed experimentally by Reynolds [1], should always be emphasized: when a flow transits from laminar to turbulent with increased flow speed, its velocity trajectories change from a steady linear pattern to a dynamic and sinuous pattern, making it more efficient in mixing. For instance, in the process of mixing different reactants in a combustion device or a chemical reactor, turbulence contributes significantly to ensuring that different flow streams can be mixed as rapidly as possible. Turbulence is also efficient for enhancing the heat and mass transfer at the interfaces of the turbulent multi-phase flows. Therefore, a thorough understanding of turbulent flows is of great importance to a broad range of engineering applications [2]. However, as every coin has two sides, turbulence is not always beneficial. For instance, substantial hydrodynamic losses and energy consumption are encountered when transporting turbulent fluids in pipelines [3,4]. Turbulent flows around the wings of aircraft and the ship hulls also lead to significant increases in wall shear stresses, causing safety issues and decreasing durations of the manufacturing materials [5-8].

To describe the mechanics of turbulence and thus to predict turbulence as it mixes and diffuses, disrupts and dissipates, the Navier-Stokes equations consisting of time-dependent conservation of momentum equations were developed in 1822. Although the Navier–Stokes equations for turbulent flows have been known for a long time, the simulation of turbulent flows by means of computational fluid dynamics is highly challenging due to the three dimensional, time-dependent, and random velocity field

[9]. Depending on the degree of flow details that are being resolved, several modeling levels, from the computationally cheaper Reynolds–Averaged Navier–Stokes (RANS) approach, to the costlier large-eddy simulation (LES) approach, and direct numerical simulation (DNS) can be distinguished [9]. The solution accuracy improves from the RANS approach where only the Reynolds equations are solved to determine the mean velocity field, to the LES approach where the large-scale turbulent motions are successfully represented, to DNS, in which the solutions of all the length and time scales relevant to the turbulent motions become achievable [2]. Due to the available computing power, it has only recently become possible to track the dynamics of eddies in relative simple turbulent flow with low Reynolds numbers and simple geometries. The computing requirements for the DNS of the time-dependent Navier–Stokes equations for practical turbulent flows with high Reynolds number have to await major developments in computer hardware, possibly those based on quantum computing [9].

Over the past few decades, various techniques have been explored to reduce the dissipated energy losses arising from the turbulent friction [10, 11]. Compared with the passive drag reduction efforts that make use of riblets, traveling waves, and microbubbles, the active drag reduction by adding minute amounts of polymers or surfactants to turbulent flows has attracted great interest [11]. To date, drag reduction (DR) techniques have found extensive use in different applications, including but not limited to anti-corrosion in oil and gas conduits [12], irrigation [13], catalyzed bioreactors [14], energy loss prevention in water heating and cooling systems [15], biomedical systems including blood pressure control [16], sewer systems [17], hydraulic fracturing for reservoir engineering [18], ocean and naval engineering [19], floodwater disposals [20], and extended well drilling system [21].

Polymer additives have long been known as highly potent drag-reducing agents, and polymer DR has been extensively studied since it was first reported by Toms [22]. Experimental investigations confirmed that as high as 80% of friction drop is attainable for turbulent pipe flows by adding polymer additives [23, 24]. It was also reported that the presence of polymer solutions considerably reduces the power levels in the transportation of suspensions of sand and slag particles [25], the typical drilling fluids in oil production. Moreover, the practical use of polymer drag reducers has been seen in the Alaska pipeline, where the crude oil transport capacity of the pipeline was increased by about 31200 m³ per day, equating to 1% of the domestic oil consumption for the U.S. at the time [26].

Although the onset of DR, the existence of maximum DR (MRD), and the main factors affecting DR behaviors have been observed and proved experimentally, it was not until recently that progress had been made to elucidate the interactions between polymers and turbulence, which have been reasoned to be responsible for DR [27]. Such progress comes largely from numerical simulations of viscoelastic turbulent flows and detailed turbulence measurements in flows of dilute polymer solutions using laser-based optical techniques [28]. Nonetheless, further theoretical research is still needed to clarify the detailed mechanisms of polymer DR and the quantitative magnitude of MDR.

Intensive research studies have been conducted both experimentally and numerically for Newtonian fluid in various geometries. However, nearly all the numerical studies using the FENE-P (finitely extensible nonlinear elastic with Peterlin's function) model for turbulent DR are limited to the plane channel geometry. The main focus of the reported DNS studies was to determine the key feature of the polymer solution (viscosity or elasticity) that contributes the most to DR and to recast how the structure

of the turbulent flow is modified by each rheological parameter (relaxation time, maximum elongation length and viscosity) of the polymer solution. In contrast, most of the RANS studies were devoted to interpreting the interactions between the turbulence and the polymer additives so that a more reliable prediction of DR can be achieved.

The interactions between DR polymers and the turbulent flow in the cylindrical annulus were experimentally proved to be highly dependent on the geometry of the walls [28-30]. However, such a geometrical impact on polymer DR was scarcely carried out by numerical studies. While recently, RANS modeling of DR for turbulent channel flow has been successfully fulfilled by Iaccarino et al. [31] and Masoudian et al. [32], their simulation results were only compared with DNS data, lacking direct validations against any experimental results. Although Ptasinski et al. validated their FENE-P model-based DNS simulation results against experimental data at a fixed DR magnitude, all the rheological parameters used in their simulations are tuned independently of the experimental study [33,34]. There is no doubt that the direct relation of the experimentally measured fluid properties to the rheological parameters used in the numerical simulation is challenging since the elastic features of the non-Newtonian polymer solutions are difficult to measure and thus barely discussed [35].

1.2 Research Objectives

To address the aforementioned issues in polymer induced drag reduction, an important research topic in the area of fluid transportation, the current research aims to study the turbulent DR in the cylindrical geometry using a numerically inexpensive method and validate the simulation results using reported experimental results. More specifically, this study entailed the following task:

- To apply a theoretical model for analyzing energy conservation of incompressible flows, in a mathematical notation of square-root variables, inner products, and differential operator symmetries.
- To predict turbulent DR using a computationally inexpensive method (RANS model) and validate the simulation results using both DNS simulation results and experimental data.
- To find proper correlations between elastic and viscous properties of different polymer solutions based on extensive experimental data, and apply them to the numerical simulations of turbulent drag reduction.
- To disclose the synergistic effects of polymer additives and the transverse curvature in annular geometries on turbulent DR.

1.3 Organization of the Thesis

This thesis has been organized with a manuscript format such that the main body consists of four manuscripts (Chapters 3-6) that can be read independently. The detailed organization of this thesis is as follows:

A general introduction regarding the problem statement, research objective, and major contributions of the present research is provided in Chapter 1. Following the brief introduction, an overall literature review for the subject matter in this thesis is provided in Chapter 2. Chapter 3 investigates turbulent flows of the Newtonian fluid in the concentric annulus with two different radius ratios at three different Reynolds numbers using RANS simulations, with the primary effort made on finding the dependence of turbulent flow field on the geometrical curvature effect and Reynolds number. Similar flow scenario models developed in chapter 3 are used in Chapter 4 for the simulation of non-Newtonian fluid in the turbulent DR. In chapter 5, a RANS model is proposed for turbulent DR in cylindrical geometries, with the molecular representation of

polymer solution accounted for by the FENE-P model. Performances of the proposed model for predicting drag reduction for different polymer solutions in pipes and concentric annulus are validated by experiment results. Following Chapter 5, a comprehensive analysis of the turbulent DR flow in the concentric annulus is carried out in Chapter 6, which mainly investigates the interactions between polymer additives and the geometrical curvature on the DR behaviors. Finally, the main conclusions drawn from this research and recommendations for future works are summarized in Chapter 7.

1.4 References

1. Reynolds, O.: An experimental investigation of the circumstances which determine whether the motion of water shall be direct or sinuous, and of the law of resistance in parallel channels. *Philosophical Transactions of the Royal Society of London*(174), 935-982 (1883).
2. Pope, S.B.: *Turbulent flows*. IOP Publishing, (2001)
3. McClure, D.D., Kavanagh, J.M., Fletcher, D.F., Barton, G.W.: Development of a CFD model of bubble column bioreactors: part two—comparison of experimental data and CFD predictions. *Chemical Engineering & Technology* **37**(1), 131-140 (2014).
4. Gasljevic, K., Hall, K., Chapman, D., Matthys, E.: Drag-reducing polysaccharides from marine microalgae: species productivity and drag reduction effectiveness. *Journal of applied phycology* **20**(3), 299-310 (2008).
5. Gerz, T., Holzapfel, F.: Wing-tip vortices, turbulence, and the distribution of emissions. *AIAA Journal* **37**(10), 1270-1276 (1999).

6. Bailey, S., Tavoularis, S.: Measurements of the velocity field of a wing-tip vortex, wandering in grid turbulence. *Journal of Fluid Mechanics* **601**, 281-315 (2008).
7. Hirata, N., Hino, T.: An efficient algorithm for simulating free-surface turbulent flows around an advancing ship. *Journal of The Society of Naval Architects of Japan* **1999**(185), 1-8 (1999).
8. Long, Y., Long, X., Ji, B., Huang, H.: Numerical simulations of cavitating turbulent flow around a marine propeller behind the hull with analyses of the vorticity distribution and particle tracks. *Ocean Engineering* **189**, 106310 (2019).
9. Argyropoulos, C.D., Markatos, N.C.: Recent advances on the numerical modelling of turbulent flows. *Applied Mathematical Modelling* **39**, 693-732 (2015).
10. Xi, L.: Turbulent drag reduction by polymer additives: Fundamentals and recent advances. *Physics of Fluids* **31**(12), 121302 (2019).
11. Nesyn, G.V., Sunagatullin, R.Z., Shibaev, V.P., Malkin, A. Ya.: Drag reduction in transportation of hydrocarbon liquids: from fundamentals to engineering applications. *Journal of Petroleum Science and Engineering* **161**, 715-725 (2018).
12. Schmitt, G.: Drag reduction by corrosion inhibitors—A neglected option for mitigation of flow induced localized corrosion. *Materials and Corrosion* **52**(5), 329-343 (2001).
13. Khalil, M., Kassab, S., Elmiligui, A., Naoum, F.: Applications of drag-reducing polymers in sprinkler irrigation systems: Sprinkler head performance. *Journal of irrigation and drainage engineering* **128**(3), 147-152 (2002).

14. Kawase, Y.: Effect of polymer additives on hydrodynamics and oxygen transfer in a bubble column bioreactor. *Journal of Chemical Technology & Biotechnology* **58**(1), 81-87 (1993).
15. Myska, J., Mik, V.: Application of a drag reducing surfactant in the heating circuit. *Energy and Buildings* **35**(8), 813-819 (2003).
16. Kameneva, M.V., Wu, Z.J., Uraysh, A., Repko, B., Litwak, K.N., Billiar, T.R., Fink, M.P., Simmons, R.L., Griffith, B.P., Borovetz, H.S.: Blood soluble drag-reducing polymers prevent lethality from hemorrhagic shock in acute animal experiments. *Biorheology* **41**(1), 53-64 (2004).
17. Sellin, R.: Drag reduction in sewers: First results from a permanent installation. *Journal of Hydraulic Research* **16**(4), 357-371 (1978).
18. Ibrahim, A.F., Nasr-El-Din, H.A., Rabie, A., Lin, G., Zhou, J., Qu, Q.: A New Friction-Reducing Agent for Slickwater-Fracturing Treatments. *SPE Production & Operations* **33**(03), 583-595 (2018).
19. Khomyakov, A., Elyukhina, I.: Complete dynamic similarity for sea trials and towing tank experiments by means of polymer drag reduction. *Ocean Engineering* **178**, 31-37 (2019).
20. Brostow, W.: Drag reduction in flow: Review of applications, mechanism and prediction. *Journal of industrial and Engineering Chemistry* **14**(4), 409-416 (2008).

21. Arnipally, S.K., Kuru, E.: Settling velocity of particles in viscoelastic fluids: a comparison of the shear-viscosity and elasticity effects. *SPE Journal* **23**(5), (2018).
22. Toms, B.A.: Some observations on the flow of linear polymer solutions through straight tubes at large Reynolds numbers. *Proceedings of the 1st International Congress on Rheology*, 135-141. North-Holland Amsterdam (1948).
23. Burger, E.D., Munk, W.R., Wahl, H.A.: Flow increase in the trans Alaska pipeline through use of a polymeric drag-reducing additive. *Journal of Petroleum Technology* **34**(02), 377-386 (1982).
24. Lumley, J.L.: Drag reduction by additives. *Annual Review of Fluid Mechanics* **1**(1), 367-384 (1969).
25. Shenoy, A.: *Rheology of Drag Reducing Fluids*, Springer, Cham, 1-38 (2020).
26. Virk, P.S.: Drag reduction fundamentals. *AIChE Journal* **21**(4), 625-656 (1975).
27. White, C.M., Mungal, M.G.: Mechanics and prediction of turbulent drag reduction with polymer additives. *Annual Review of Fluid Mechanics* **40**, 235-256 (2008).
28. Nouri, J., Umur, H., Whitelaw, J.: Flow of Newtonian and non-Newtonian fluids in concentric and eccentric annuli. *Journal of Fluid Mechanics* **253**, 617-641 (1993).
29. Bizhani, M., Corredor, F.E.R., Kuru, E.: An experimental study of turbulent non-newtonian fluid flow in concentric annuli using particle image velocimetry technique. *Flow, Turbulence, and Combustion* **94**(3), 527-554 (2015).

30. Rodriguez Corredor, F.E., Bizhani, M., Kuru, E.: Experimental investigation of drag-reducing fluid flow in annular geometry using particle image velocimetry technique. *Journal of Fluids Engineering* **137**(8) (2015).
31. Iaccarino, G., Shaqfeh, E.S., Dubief, Y.: Reynolds-averaged modeling of polymer drag reduction in turbulent flows. *Journal of Non-Newtonian Fluid Mechanics* **165**(7), 376-384 (2010).
32. Masoudian, M., Pinho, F., Kim, K., Sureshkumar, R.: A RANS model for heat transfer reduction in viscoelastic turbulent flow. *International Journal of Heat and Mass Transfer* **100**, 332-346 (2016).
33. Ptasinski, P., Boersma, B., Nieuwstadt, F., Hulsen, M., Van den Brule, B., Hunt, J.: Turbulent channel flow near maximum drag reduction: simulations, experiments and mechanisms. *Journal of Fluid Mechanics* **490**, 251-291 (2003).
34. Ptasinski, P., Nieuwstadt, F., Van Den Brule, B., Hulsen, M.: Experiments in turbulent pipe flow with polymer additives at maximum drag reduction. *Flow, Turbulence, and Combustion* **66**(2), 159-182 (2001).
35. Zhang, X., Duan, X., Muzychka, Y.: Analytical upper limit of drag reduction with polymer additives in turbulent pipe flow. *Journal of Fluids Engineering* **140**(5) (2018).

Chapter 2 Literature Review

2.1 Turbulent Newtonian Flow

2.1.1 Experimental Investigation of Newtonian Fluid

Turbulent flow in the cylindrical annular geometry distinguishes itself from turbulent flows in the channel and pipe counterparts by having asymmetry profiles of flow variables in the cross-section of the annulus, such as velocity and shear stress. As a result, early research in this field focused on accurately measuring the distributions of these two variables and determining whether the radial positions of the zero shear stress and the maximum velocity coincide.

The assumption of such coincidence, mainly due to the evidence from laminar flow, was widely adopted in early researches [1,2] and experimentally supported by Walker et al. [3], Brighton et al. [4], and Quarmby [5] with different measuring techniques, until Smith et al. [6] and Lawn et al. [7] showed for the first time that those positions do not necessarily coincide even in smooth annuli, through measurements using the “sliding sleeve” method and the hot-wire technology. Rehme [8] drew the same conclusion in his study and further suggested that the position of the zero shear stress was closer to the inner surface, while the most recent experimental studies of Nouri et al. [9] and Rodriguez et al. [10] also confirmed such findings, using more advanced laser doppler velocimetry (LDV) and particle image velocimetry (PIV) technologies, respectively. However, despite being investigated extensively by experiments in the past, whether or not the zero shear stress coincides with the maximum velocity in the annular geometry remains disputable.

2.1.2 DNS Investigation of Newtonian Fluid

In the past three decades, with the rapid enhancement of computational power, numerical simulations have become an essential tool for turbulence analysis in the cylindrical annular geometry. In addition to being another source for predicting the locations of the zero shear stress and the maximum velocity, the numerical approach serves as an ideal tool for investigating the influence of the transverse curvature in the annular geometry.

Among different numerical approaches, direct numerical simulation (DNS) is the most reliable and accurate one. In a DNS simulation, the Navier-Stokes equations are solved directly for the instantaneous turbulent velocity $\hat{\mathbf{U}}$, *m/s*, as shown in the following governing equations for incompressible Newtonian flows:

Continuity:

$$\nabla \cdot \hat{\mathbf{U}} = 0 \quad (2-1)$$

Momentum:

$$\rho \frac{\partial \hat{\mathbf{U}}}{\partial t} + \rho \nabla \cdot (\hat{\mathbf{U}} \hat{\mathbf{U}}) = \mu_s \nabla \cdot [\nabla \hat{\mathbf{U}} + (\nabla \hat{\mathbf{U}})^T] - \nabla P \quad (2-2)$$

Conceptually, DNS is the simplest approach since no pre-treatment, for instance, the filtering in the LES approach or the Reynolds decomposition in the RANS approach, is needed for the time-dependent turbulent velocity $\hat{\mathbf{U}}$. However, the drawback of such an approach is obvious that the computational cost is extremely high, and thus its application is restricted to flows with relatively low Reynolds numbers and simple geometries.

Neves et al. [11] were the pioneers to investigate the transverse curvature affected turbulent flow field using DNS. Their results suggested that the slope of the mean velocity profile in the logarithmic region, the turbulence intensities, and the Reynolds stress decrease with the increase in curvature, which was also confirmed later by the DNS work of Shin et al. [12]. However, those studies were conducted in a truncated domain where only the inner boundary layer in an annular geometry was accurately solved, which is sufficient to support their investigation for the curvature effect but missing the essential outer boundary layer.

Chung et al. [13] were the first to conduct DNS simulation in the full domain of a concentric annulus, with two radius ratios representing both high (small radius ratio) and low (large radius ratio) curvature effects at fixed Reynolds number, the same geometries investigated experimentally by Nouri et al. [9]. They reported that the distributions of the flow statistics in the wall-normal direction are highly dependent on the radius ratio of the annulus, with more asymmetric flow obtained with a smaller radius ratio. They also stated that the smaller surface area of the inner wall supplies relatively less turbulent kinetic energy than the outer wall, leading to weaker turbulent intensities and less Reynolds shear stress. Besides, their work numerically confirmed the finding from experimental studies that the positions of the zero shear stress are closer to the inner wall than that of the maximum velocity.

2.1.3 RANS Modelling of Newtonian Fluid

A meticulous literature review indicates that the simulation of turbulent flows using the Reynolds-averaged Navier-Stokes (RANS) simulation is more attractive in terms of

its balance between accuracy and computational efficiency [14,15]. Compared to DNS, this approach reduces the computational expense of turbulence modelling significantly by only solving the average flow field, enabling itself to be applied more broadly to increasingly complex configurations [16].

In a RANS simulation, the time-dependent velocity of the turbulent flow is decomposed into the time-averaging and time-fluctuating components as:

$$\hat{\mathbf{U}} = \mathbf{U} + \mathbf{u} \quad (2-3)$$

Accordingly, wherever applicable in this thesis, an upper-case letter or a letter with an overbar represents a time-averaged variable, and its lower-case counterpart denotes the time-fluctuating part of the variable. Taking the mean of the governing equations Eq. (2-2) and replacing $\hat{\mathbf{U}}$ by Eq. (2-3), the continuity and momentum equations read:

$$\nabla \cdot \mathbf{U} = 0 \quad (2-4)$$

$$\rho \frac{\partial \mathbf{U}}{\partial t} + \rho \nabla \cdot \overline{(\mathbf{U} + \mathbf{u})(\mathbf{U} + \mathbf{u})} = \mu_s \nabla \cdot [\nabla \mathbf{U} + (\nabla \mathbf{U})^T] - \nabla P \quad (2-5)$$

The second term on the left side of Eq. (2-5) is the nonlinear convective term and needs further simplification as:

$$\overline{(\mathbf{U} + \mathbf{u})(\mathbf{U} + \mathbf{u})} = \overline{\mathbf{U}\mathbf{U}} + \overline{\mathbf{U}\mathbf{u}} + \overline{\mathbf{u}\mathbf{U}} + \overline{\mathbf{u}\mathbf{u}} = \mathbf{U}\mathbf{U} + \overline{\mathbf{u}\mathbf{u}} \quad (2-6)$$

Therefore, the ultimate form of the momentum equations in the RANS simulation for turbulent Newtonian flows can be expressed as:

$$\rho \frac{\partial \mathbf{U}}{\partial t} + \rho \nabla \cdot \mathbf{U}\mathbf{U} = \mu_s \nabla \cdot [\nabla \mathbf{U} + (\nabla \mathbf{U})^T] - \rho \nabla \cdot \overline{\mathbf{u}\mathbf{u}} - \nabla P \quad (2-7)$$

where $\overline{\mathbf{u}\mathbf{u}}$ have been defined as the Reynolds stresses, Pa . Since only the time-averaging velocity is directly solved in the RANS approach, this term needs to be accurately estimated by the turbulence models in order to solve Eq. (2-7). Specifically,

for the first order turbulent-viscosity method used in the current study, the Reynolds stresses are modelled via the turbulent viscosity hypothesis, which relates the Reynolds stress to the turbulent viscosity ν_t (also called the eddy viscosity), m^2/s , and the average strain rate tensor:

$$\overline{uu} = \nu_t[\nabla U + (\nabla U)^T] \quad (2-8)$$

Consequently, to have an appropriate estimation of the turbulent viscosity is fundamental to a RANS simulation, which determines how accurate this method is and has attracted significant research interest.

Counting how many additional transport equations of turbulent variables to involve, this topic can be started by introducing the zero-equation model, or the mixing-length model developed by Prandtl [17], in which the position-dependent mixing length is used with the mean shear rate to estimate the turbulent viscosity explicitly, with no additional transport equation needed:

$$\nu_t = l_m^2[\nabla U + (\nabla U)^T] \quad (2-9)$$

Despite being arguably the simplest turbulence model that is applicable to all turbulent flows [18-20], its drawback is apparent that the model is not complete since the mixing length l_m , m , has to be specified, which is highly dependent on the geometry of the flow. It also fails to predict the circumstances where the average velocity gradient is zero but the turbulent velocity scale is non-zero, such as in the decaying grid turbulence and at the centreline of the round jet, which motivates the development of the one-equation model.

The one-equation model proposed by Kolmogorov [21] and Prandtl [22], alternatively, suggested relating the turbulent viscosity to the turbulent kinetic energy (TKE) and closing the correlation between them by solving a model transport equation, which can be derived directly from the momentum equation of the turbulent velocity:

$$\nu_t = ck^{1/2}l_m \quad (2-10)$$

$$\frac{\partial k}{\partial t} + \nabla \cdot \mathbf{U}k = \left(\nu_s + \frac{\nu_t}{\sigma_k}\right) \nabla^2 \cdot k + P_k - \varepsilon \quad (2-11)$$

where c and σ_k are the dimensionless model constants, $(-)$, $k = \frac{1}{2}(\bar{u}_i^2 + \bar{u}_j^2 + \bar{u}_k^2)$ is TKE, m^2/s^2 , and $P_k = \frac{\nu_t}{2}[\nabla \mathbf{U} + (\nabla \mathbf{U})^T]^2$ is the production of TKE, m^2/s^3 . However, in spite of the modest improvement of accuracy compared to the mixing length model [23], the specification of the turbulent length scale remains a priori in this method. One way to overcome this drawback, wherever applicable, is to use another one-equation model developed by Spalart and Allmaras [24], which solves a transport equation of the turbulent viscosity directly instead of using the correlation of the turbulent kinetic energy and the mixing length. However, this model is specially designed for aerodynamic flows, for instance, the transonic flow over airfoils, and thus, as an effort to provide a complete turbulence model without specifying a flow-dependent length scale for broader engineering applications, the two-equation turbulence models emerged.

While many two-equation turbulence models have been proposed [21, 25-27], the $k - \varepsilon$ model is the most widely used one, which has been incorporated in most commercial computational fluid dynamics (CFD) codes. Compared to the one-equation model, this model is made complete by defining the turbulent length scale by the

turbulent kinetic energy k and the dissipation rate of the turbulent kinetic energy ε , m^2/s^3 :

$$\nu_t = C_\mu k^2 / \varepsilon \quad (2-12)$$

which are solved by two individual transport equations. Therefore, no flow-dependent specification of the turbulent length scale is needed. This model was first developed by Johns and Launder [28] and later optimized by Launder and Sharma [29]. Different from Eq. (2-11) for k , the transport equation of ε in the standard $k - \varepsilon$ is not derived directly but formed empirically as:

$$\frac{\partial \varepsilon}{\partial t} + \nabla \cdot \mathbf{U} \varepsilon = \left(\nu_s + \frac{\nu_t}{\sigma_\varepsilon} \right) \nabla^2 \cdot \varepsilon + C_{\varepsilon 1} \frac{\varepsilon \cdot P_k}{k} - C_{\varepsilon 2} \frac{\varepsilon^2}{k} \quad (2-13)$$

where $C_{\varepsilon 1}$, $C_{\varepsilon 2}$, and σ_ε are dimensionless model constants.

The second most widely used two-equation model is the $k - \omega$ model developed by Wilcox and other contributors (mentioned in his paper Wilcox [23]), with the transport equation of ε replaced by that of ω , $1/s$, named the turbulence frequency (see model detail in Chapters 3 and 4). Compared with the $k - \varepsilon$ model, Wilcox's $k - \omega$ model is specialized in treating the viscous near-wall region and accounting for the effects of streamwise pressure gradients for boundary-layer flows. However, the solution of this model is too sensitive to the non-physical, non-zero free-stream boundary condition required for ω [30].

To address this issue, another two-equation model that worthies a note is the one developed by Menter [31], which takes the advantages of both the $k - \varepsilon$ and $k - \omega$ models and is often referred to as the shear stress transport (SST) model (see model detail in Chapters 3 and 4). With a specially defined blending function, this model

transferred from the $k - \omega$ formulation at the near-wall region to the $k - \varepsilon$ model away from the wall in the wall bounded flow, eliminating the demand of a free-stream boundary condition for the ω equation and improving accuracy.

All the above turbulent-viscosity models suffer from the inherent isotropic turbulence assumption, and thus, are insensitive to the anisotropic turbulence in the wall-normal direction, leading to over predicted turbulent kinetic energy in the wall-bounded flow. To improve performance, Durbin [32] proposed a four-equation model based on the $k - \varepsilon$ model, solving two additional equations, one for the velocity variance $\overline{v^2}$, m^2/s^2 and the other for the turbulence redistribution function, $f(-)$ (see model detail in Chapter 5). By involving $\overline{v^2}$ in the formulation of the turbulent viscosity, this model successfully characterizes the turbulence anisotropy and the non-local pressure-strain effects. The complicated damping functions required in the standard low Reynolds number (LRN) turbulence models are also avoided by using this model, significantly improving model efficiency.

With advances in turbulence modelling, many RANS studies have been carried out in the past decade for turbulent flow in the cylindrical annular geometry [33-38]. Xiong et al. [39] conducted RANS simulations in annular geometries with two different radius ratios and three different Reynolds numbers, as an effort to investigate the dependence of the turbulent flow field on both the curvature and Reynolds number, and obtained satisfactory agreements between their results and results from both DNS [13] and experimental studies[9] regarding locations of the zero shear stress and the maximum velocity. They also showed that the RANS model could successfully capture the

transverse curvature effect, and such an effect on the flow field in a concentric annulus is more pronounced compared to that of the Reynolds number.

In the RANS simulation, only the averaged Navier-Stokes equations are directly solved, with turbulence variables, such as Reynolds stress, evaluated by the turbulence model, which relies heavily on empiricism [15]. Thus, the success of the RANS modelling is highly dependent on the advances in experimental and DNS databases from which more reliable turbulence models can be developed. For instance, the all the model constants discussed previously in the transport equations of the standard turbulent-viscosity model are obtained empirically from the turbulent flow of Newtonian fluids, making the model unable to treat turbulence of non-Newtonian fluid accurately. Therefore, when modelling non-Newtonian turbulence, new closures are needed, by analyzing data from experimental or DNS studies, to capture the essential features of the non-Newtonian fluid, such as the drag reduction (DR) phenomenon, which has drawn great attention from researchers.

2.2 Turbulent Drag Reduction Flow

2.2.1 Experimental Investigations of Drag Reduction Fluid

Polymer induced DR stands for the phenomenon first reported by Toms [40] that by adding a proper amount of high molecular weight, long-chain polymers, the frictional drag of the solution can be substantially reduced at high Reynolds number, compared to that of the pure water solvent. The two most important findings for this behavior from a vast amount of experimental studies are those of Virk et al. [41,42], showing the existences of the onset and upper limit of DR, suggesting that DR is not solely caused

by viscous effect [43]. These studies contributed significantly to the establishments of the two principle concepts that have been widely cited to explain polymer-induced DR theoretically.

The first, proposed by Lumley [44,45] and widely referred to as the extensional viscosity hypothesis, is based on the polymer extension mechanism. It suggests that the polymer induced DR is mainly caused by the stretching of the randomly coiled polymers, which primarily occurs in the highly deformed buffer layer in a wall-bounded flow. Such stretching increases the effective viscosity of polymer solutions, leading to the thickening of the viscous sublayer. This thickened viscous sublayer suppresses the turbulent eddies near the wall and leads to DR.

Contrarily, Gennes [43] proposed an elastic theory, claiming that the elastic features of the polymers, which create shear waves that prevent the production of turbulent velocity fluctuations at small scales, are instead the primary cause of DR. He argued that the extensional-viscosity theory can explain neither the onset nor the upper limit of DR, and that DR can occur even before the polymer molecules have reached the solid wall after they are injected far away from the wall in the wall-bounded turbulent flow.

The debate implies that numerical models that focus on adequately characterizing only the viscous features of the polymer solutions are insufficient to recast the entire mechanism relevant to DR dynamics, even if the DR can be numerically achieved [46,47]. Such models fail to produce the stress deficit in turbulent DR flow that has been widely reported by experimental studies [47-49]. Nowadays, it becomes generally accepted that both the viscous and elastic features of the polymer solution contribute

cooperatively to the polymer induced DR, and numerical models that take into account both features are named the viscoelastic model. Subsequently, the non-Newtonian fluid whose DR feature can be accurately captured by such models can also be called the viscoelastic fluid.

2.2.2 DNS Investigation of Drag Reduction Fluid Using FENE-P Model

With the development of reliable viscoelastic models and again the rapid improvement of computational powers, DNS has become a powerful tool to investigate turbulent DR both qualitatively and quantitatively, which helps expose more details of the mechanisms underlying the behavior of the polymer-induced DR [50-54]. Interactions between the turbulent flow field and the polymer additives have been investigated extensively by DNS lately, by which the finitely extensible nonlinear elastic-Peterlin (FENE-P) model gains its popularity among other viscoelastic models, characterizing both the viscous and elastic features of the polymers using the elastic dumbbell model (see Chapter 5 for model details). This constitutive model relates the drag reduction feature of polymers to the stretching-releasing mechanism of its elastic chains, which can be appropriately characterized by the rheological parameters of polymers, such as the relaxation time, the elasticity, and the polymeric viscosity, allowing each of them to be investigated independently and making it possible to reveal their sole contributions to the DR behaviors of the polymer solution [55].

Sureshkumar et al. [56] were the first to utilize a proper viscoelastic model for DNS simulations, showing the robust performance of the FENE-P model in characterizing polymer induced drag reduction dynamics. Since detailed measurements of turbulence

variables in the laboratory are challenging and highly restricted by measuring techniques, especially for polymer solutions, in which the rheological properties are incredibly complicated, their DNS study encouraged many newcomers to use DNS for analyzing turbulent DR [57-62]. Despite advancing the fundamental understandings of this phenomenon, the recent booming of DNS studies supplies an abundance of databases for researchers to develop more cost-effective numerical approaches in this research field, for instance, the Reynolds-averaged-Navier-Stokes (RANS) approach.

2.2.3 RANS Modelling of Drag Reduction Fluid Using FENE-P Model

As discussed previously, DNS is computationally much more expensive than RANS. In particular, for simulations of the turbulent drag reduction flow, uses of the FENE-P model bring in nine additional evolution equations of the polymer conformation tensor. Each component of the conformation tensor needs to be solved for the entire turbulent time and length scales, which is extremely time-consuming, even with the supercomputing [63]. Thus, the development of a RANS method that is capable of modelling the polymer induced turbulent DR is highly beneficial and has been one of the most attractive topics in the past decade.

Poreh et al. [64] and Durst et al. [65] tried to meet that target by tuning one of the constants in the standard $k - \varepsilon$ model according to an empirical correlation. Similar approach was also applied by Xiong et al. [66] to the SST model to simulate the drag reduction behavior of the shear-thinning fluid. Despite successfully adjusting the mean velocity profile and achieving DR, such approaches lack a rational molecular

representation of the polymer solution relevant to its drag reduction feature and are thus less applicable.

The initial effort to include the molecular representation of the polymers by involving the FENE-P model in the RANS method was made by using the low Reynolds number (LRN) k - ε model [67-69], until Resende et al. [69] concluded that such methods proposed based on the traditional k - ε model cannot properly predict the flow field of polymer solutions at high DR. They explained that in DR solutions, the magnitude of turbulence anisotropy increases dramatically with the increase in DR, while the k - ε model is limited by its inherent isotropic turbulence assumption, leading to unrealistic predictions of turbulence at high DR, which was later found also true for the k - ω based model [70].

To this end, Iaccarino et al. [71] developed a RANS approach for polymer-induced turbulent DR flow based on the k - ε - $\overline{v^2}$ - f model, where the wall-normal anisotropic turbulence accounted for by the velocity variance $\overline{v^2}$ is solved directly. This approach successfully captured the behavior of turbulent channel flow up to the maximum DR, and further, they demonstrated the postulation of the standard k - ε - $\overline{v^2}$ - f model [72] for Newtonian fluids also suitable for polymer solutions, emphasizing the dominant role played by the wall-normal turbulent fluctuations on the eddy viscosity in the near-wall region. Hence, no damping function is needed neither in the DR modelling to reduce turbulence activity at the wall using this model (see Chapter 5 for model details).

Their model was later assessed and improved by Masoudian et al. [55] with new closures. However, this model only considers the extension of the polymer chains,

neglecting the effects made by the spins of their orientation. Most recently, Masoudian et al. [73] addressed this issue by further improving their closures, providing the most reliable RANS model to date for modelling turbulent DR induced by polymer additives.

2.3 References

1. Knudsen, J.: Velocity profiles in annuli. Proceeding of 1st Midwestern Conference on Fluid Dynamics, 175-203. (1951)
2. Rothfus, R., Sartory, W., Kermode, R.: Flow in concentric annuli at high Reynolds numbers. *AIChE Journal* **12**(6), 1086-1091 (1966).
3. Walker, J., Rothfus, R.: Transitional velocity patterns in a smooth concentric annulus. *AIChE Journal* **5**(1), 51-54 (1959).
4. Brighton, J. A. and Jones, J. B.: Fully Developed Turbulent Flow in Annuli. *Journal of Basic Engineering D*, **86**, 835-844 (1964).
5. Quarmby, A.: On the use of the Preston tube in concentric annuli. *The Aeronautical Journal* **71**(673), 47-49 (1967).
6. Smith, S., Hamlin, M., Lawn, C.: The direct measurement of wall shear stress in an annulus. Berkeley Nuclear Laboratories, Research Department, Central Electricity (1968)
7. Lawn, C., Elliott, C.: Fully developed turbulent flow through concentric annuli. *Journal of Mechanical Engineering Science* **14**(3), 195-204 (1972).
8. Rehme, K.: Turbulent flow in smooth concentric annuli with small radius ratios. *Journal of Fluid Mechanics* **64**(2), 263-288 (1974).

9. Nouri, J., Umur, H., Whitelaw, J.: Flow of Newtonian and non-Newtonian fluids in concentric and eccentric annuli. *Journal of Fluid Mechanics* **253**, 617-641 (1993).
10. Rodriguez-Corredor, F., Bizhani, M., Ashrafuzzaman, M., Kuru, E.: An experimental investigation of turbulent water flow in concentric annulus using particle image velocimetry technique. *Journal of Fluids Engineering* **136**(5), 051203 (2014).
11. Neves, J.C., Moin, P., Moser, R.D.: Effects of convex transverse curvature on wall-bounded turbulence. Part 1. The velocity and vorticity. *Journal of Fluid Mechanics* **272**, 349-382 (1994).
12. Shin, D., Lee, S., Na, Y.: Space-time characteristics of the wall shear-stress fluctuations in an axial turbulent boundary layer with transverse curvature. *Journal of mechanical science and technology* **19**(8), 1682-1691 (2005).
13. Chung, S.Y., Rhee, G.H., Sung, H.J.: Direct numerical simulation of turbulent concentric annular pipe flow: Part 1: Flow field. *International Journal of Heat and Fluid Flow* **23**(4), 426-440 (2002).
14. Kalitzin, G., Medic, G., Iaccarino, G., Durbin, P.: Near-wall behavior of RANS turbulence models and implications for wall functions. *Journal of Computational Physics* **204**(1), 265-291 (2005).
15. Durbin, P.A.: Some recent developments in turbulence closure modeling. *Annual Review of Fluid Mechanics* **50**, 77-103 (2018).

16. Launder, B.E., Sandham, N.D.: Closure strategies for turbulent and transitional flows. Cambridge University Press, (2002)
17. Prandtl, L.: 7. Bericht über Untersuchungen zur ausgebildeten Turbulenz. ZAMM- Journal of Applied Mathematics and Mechanics/Zeitschrift für Angewandte Mathematik und Mechanik **5**(2), 136-139 (1925).
18. Pope, S.B.: Turbulent flows. IOP Publishing, (2001)
19. Smagorinsky, J.: General circulation experiments with the primitive equations: I. The basic experiment. Monthly weather review **91**(3), 99-164 (1963).
20. Baldwin, B., Lomax, H.: Thin-layer approximation and algebraic model for separated turbulent flows. Proceedings of the 16th Aerospace Sciences Meeting, (1978).
21. Kolmogorov, A.: The equations of turbulent motion of inviscid liquid. Izv. USSR Acad. Sci. Phys. Ser. **6**(1/2), 56-58 (1942).
22. Prandtl, L.: Über Reibungsschichten bei dreidimensionalen Strömungen. Festschrift zum **60**, 134-141 (1945).
23. Wilcox, D.C.: Turbulence modeling for CFD, vol. 2. DCW industries La Canada, CA, (1998)
24. Spalart, P., Allmaras, S.: A one-equation turbulence model for Aerodynamic Flows. La Recherche Aérospatiale, No. 1. (1994).
25. Rotta, J.: Statistische theorie nichthomogener turbulenz. Zeitschrift für Physik **129**(6), 547-572 (1951).

26. Saffman, P.G.: A model for inhomogeneous turbulent flow. Proceedings of the Royal Society of London. A. Mathematical and Physical Sciences **317**, 417-433 (1970).
27. Speziale, C.G., Abid, R., Anderson, E.C.: Critical evaluation of two-equation models for near-wall turbulence. AIAA Journal **30**(2), 324-331 (1992).
28. Jones W., Launder B.E.: The prediction of laminarization with a two-equation model of turbulence, International Journal of Heat and Mass Transfer, **15**, 301-314(1972).
29. Launder, B.E., Sharma, B.: Application of the energy-dissipation model of turbulence to the calculation of flow near a spinning disc. Letters in Heat and Mass Transfer **1**(2), 131-137 (1974).
30. Menter, F.: Zonal two equation $k-\omega$ turbulence models for aerodynamic flows. Proceedings of 23rd Fluid Dynamics, Plasma Dynamics, and Lasers Conference, (1993).
31. Menter, F.R.: Two-equation eddy-viscosity turbulence models for engineering applications. AIAA Journal **32**(8), 1598-1605 (1994).
32. Durbin, P.A.: Near-wall turbulence closure modeling without “damping functions”. Theoretical and Computational Fluid Dynamics **3**(1), 1-13 (1991).
33. Francis Jr, N.D., Itamura, M.T., Webb, S.W., James, D.L.: CFD calculation of internal natural convection in the annulus between horizontal concentric cylinders. Yucca Mountain Project, Las Vegas, Nevada (US), (2002).

34. Addad, Y., Laurence, D.R., Rabbitt, M.: Turbulent natural convection in horizontal coaxial cylindrical enclosures: LES and RANS models. ICHMT Digital Library Online. Begel House Inc. (2006)
35. Neto, J.V., Martins, A., Neto, A.S., Ataíde, C., Barrozo, M.: CFD applied to turbulent flows in concentric and eccentric annuli with inner shaft rotation. The Canadian Journal of Chemical Engineering **89**(4), 636-646 (2011).
36. Mme, U., Skalle, P.: CFD calculations of cuttings transport through drilling annuli at various angles. International Journal of Petroleum Science and Technology **6**(2), 129-141 (2012).
37. Marocco, L., di Valmontana, A.A., Wetzel, T.: Numerical investigation of turbulent aided mixed convection of liquid metal flow through a concentric annulus. International Journal of Heat and Mass Transfer **105**, 479-494 (2017).
38. Azouz, I., Shirazi, S.: Evaluation of several turbulence models for turbulent flow in concentric and eccentric annuli, (1998).
39. Xiong, X., Rahman, M.A., Zhang, Y.: RANS Based Computational Fluid Dynamics Simulation of Fully Developed Turbulent Newtonian Flow in Concentric Annuli. Journal of Fluids Engineering **138**(9), 091202 (2016).
40. Toms, B.A.: Some observations on the flow of linear polymer solutions through straight tubes at large Reynolds numbers. Proceedings of the 1st International Congress on Rheology, 135-141. North-Holland Amsterdam (1948).

41. Virk, P.S., Merrill, E., Mickley, H., Smith, K., Mollo-Christensen, E.: The Toms phenomenon: turbulent pipe flow of dilute polymer solutions. *Journal of Fluid Mechanics* **30**(2), 305-328 (1967).
42. Virk, P.: An elastic sublayer model for drag reduction by dilute solutions of linear macromolecules. *Journal of Fluid Mechanics* **45**(3), 417-440 (1971).
43. Gennes, P.G.D.: *Introduction to polymer dynamics*. Cambridge University Press, (1990)
44. Lumley, J.L.: Drag reduction by additives. *Annual Review of Fluid Mechanics* **1**(1), 367-384 (1969).
45. Lumley, J.L.: Drag reduction in turbulent flow by polymer additives. *Journal of Polymer Science: Macromolecular Reviews* **7**, 263-290 (1973).
46. Orlandi, P.: A tentative approach to the direct simulation of drag reduction by polymers. *Journal of Non-Newtonian Fluid Mechanics* **60**(2-3), 277-301 (1995).
47. Den Toonder, J., Hulsen, M., Kuiken, G., Nieuwstadt, F.: Drag reduction by polymer additives in a turbulent pipe flow: numerical and laboratory experiments. *Journal of Fluid Mechanics* **337**, 193-231 (1997).
48. Gyr, A., Tsinober, A.: On the rheological nature of drag reduction phenomena. *Journal of Non-Newtonian Fluid Mechanics* **73**(1-2), 153-162 (1997).
49. Warholic, M., Massah, H., Hanratty, T.: Influence of drag-reducing polymers on turbulence: effects of Reynolds number, concentration and mixing. *Experiments in fluids* **27**(5), 461-472 (1999).

50. Massah, H., Hanratty, T.J.: Added stresses because of the presence of FENE-P bead-spring chains in a random velocity field. *Journal of Fluid Mechanics* **337**, 67-101 (1997).
51. Kim, K., Li, C.-F., Sureshkumar, R., Balachandar, S., Adrian, R.J.: Effects of polymer stresses on eddy structures in drag-reduced turbulent channel flow. *Journal of Fluid Mechanics* **584**, 281-299 (2007).
52. Kim, K., Adrian, R.J., Balachandar, S., Sureshkumar, R.: Dynamics of hairpin vortices and polymer-induced turbulent drag reduction. *Physical review letters* **100**(13), 134504 (2008).
53. Stone, P.A., Roy, A., Larson, R.G., Waleffe, F., Graham, M.D.: Polymer drag reduction in exact coherent structures of plane shear flow. *Physics of Fluids* **16**(9), 3470-3482 (2004).
54. Li, W., Xi, L., Graham, M.D.: Nonlinear travelling waves as a framework for understanding turbulent drag reduction. *Journal of Fluid Mechanics* **565**, 353-362 (2006).
55. Masoudian, M., Kim, K., Pinho, F., Sureshkumar, R.: A viscoelastic turbulent flow model valid up to the maximum drag reduction limit. *Journal of Non-Newtonian Fluid Mechanics* **202**, 99-111 (2013).
56. Sureshkumar, R., Beris, A.N., Handler, R.A.: Direct numerical simulation of the turbulent channel flow of a polymer solution. *Physics of Fluids* **9**(3), 743-755 (1997).

57. Dimitropoulos, C.D., Sureshkumar, R., Beris, A.N.: Direct numerical simulation of viscoelastic turbulent channel flow exhibiting drag reduction: effect of the variation of rheological parameters. *Journal of Non-Newtonian Fluid Mechanics* **79**(2-3), 433-468 (1998).
58. Dimitropoulos, C.D., Sureshkumar, R., Beris, A.N., Handler, R.A.: Budgets of Reynolds stress, kinetic energy and streamwise enstrophy in viscoelastic turbulent channel flow. *Physics of Fluids* **13**(4), 1016-1027 (2001).
59. Sibilla, S., Baron, A.: Polymer stress statistics in the near-wall turbulent flow of a drag-reducing solution. *Physics of Fluids* **14**(3), 1123-1136 (2002).
60. De Angelis, E., Casciola, C., Piva, R.: DNS of wall turbulence: dilute polymers and self-sustaining mechanisms. *Computers & fluids* **31**(4-7), 495-507 (2002).
61. Min, T., Yoo, J.Y., Choi, H., Joseph, D.D.: Drag reduction by polymer additives in a turbulent channel flow. *Journal of Fluid Mechanics* **486**, 213-238 (2003).
62. Ptasinski, P., Boersma, B., Nieuwstadt, F., Hulsen, M., Van den Brule, B., Hunt, J.: Turbulent channel flow near maximum drag reduction: simulations, experiments and mechanisms. *Journal of Fluid Mechanics* **490**, 251-291 (2003).
63. Xi, L.: Turbulent drag reduction by polymer additives: Fundamentals and recent advances. *Physics of Fluids* **31**(12), 121302 (2019).
64. Poreh, M., Hassid, S.: Mean velocity and turbulent energy closures for flows with drag reduction. *Physics of Fluids* **20**(10), S193-S196 (1977).
65. Durst, F., Rastogi, A.: Calculations of turbulent boundary layer flows with drag reducing polymer additives. *Physics of Fluids* **20**(12), 1975-1985 (1977).

66. Xiong, X., Rahman, M.A., Zhang, Y.: Characterization of Time-Averaged Turbulence Statistics for Shear Thinning Fluid in Horizontal Concentric Annulus Using RANS Based CFD Simulation. Proceedings of ASME 35th International Conference on Ocean, Offshore and Arctic Engineering. American Society of Mechanical Engineers Digital Collection (2016).
67. Li, C.-F., Sureshkumar, R., Khomami, B.: Influence of rheological parameters on polymer induced turbulent drag reduction. *Journal of Non-Newtonian Fluid Mechanics* **140**(1-3), 23-40 (2006).
68. Pinho, F., Li, C., Younis, B., Sureshkumar, R.: A low Reynolds number turbulence closure for viscoelastic fluids. *Journal of Non-Newtonian Fluid Mechanics* **154**(2), 89-108 (2008).
69. Resende, P., Kim, K., Younis, B., Sureshkumar, R., Pinho, F.: A FENE-P $k-\varepsilon$ turbulence model for low and intermediate regimes of polymer-induced drag reduction. *Journal of Non-Newtonian Fluid Mechanics* **166**(12), 639-660 (2011).
70. Resende, P., Pinho, F., Younis, B., Kim, K., Sureshkumar, R.: Development of a Low-Reynolds-number $k-\omega$ model for FENE-P fluids. *Flow, turbulence, and combustion* **90**(1), 69-94 (2013).
71. Iaccarino, G., Shaqfeh, E.S., Dubief, Y.: Reynolds-averaged modeling of polymer drag reduction in turbulent flows. *Journal of Non-Newtonian Fluid Mechanics* **165**(7), 376-384 (2010).

72. Durbin, P.A.: Separated flow computations with the k-epsilon-v-squared model. AIAA Journal **33**(4), 659-664 (1995).
73. Masoudian, M., Pinho, F., Kim, K., Sureshkumar, R.: A RANS model for heat transfer reduction in viscoelastic turbulent flow. International Journal of Heat and Mass Transfer **100**, 332-346 (2016).

Chapter 3 RANS Based CFD Simulation of Fully Developed Turbulent Newtonian Flow in Concentric Annuli

This chapter was prepared based on a published journal article: Xiong X., Rahman A., Zhang Y.: RANS based CFD simulation of fully developed turbulent Newtonian flow in concentric annuli, ASME Journal of Fluids Engineering, **138**(9), 091202 (2016). I conducted all the simulations, prepared the manuscript, and made the revisions during the publication process. Dr. Yan Zhang helped revise the manuscript. Both Dr. Aziz Rahman and Dr. Yan Zhang provide essential supports and suggestions while running the simulations and writing the paper.

3.1 Introduction

The ability of turbulence to mix scalars within a flow field is of great importance to engineering applications [1]. For example, in a bioreactor, sufficient mixing of reactants and enzymes greatly increases the reaction conversion and yield. In subsea oil and gas pipeline transportation, where local flow conditions are critical, turbulence plays an essential role in determining the pressure loss and heat transfer, which are highly related to energy consumption. Turbulent flow in concentric annuli is essential to drilling engineering, as the flow path of the drilling fluid formed by the drill string and the well casing is exactly the same as that of an annular pipe. Many studies have been carried out in the past regarding this flow scenario.

Early research was focused on predicting the velocity and shear stress profiles. Most experimental investigations reported that in turbulent flow, the position of the maximum velocity was closer to the inner wall than in the laminar flow. However, the coincidence of the positions of zero shear stress and maximum velocity remains disputable. Brighton and Jones [2] employed a double Pitot tube to determine the velocity profiles and firstly measured the shear stress distributions by means of hot wires. Their results indicated that the position of zero shear stress was identical to the maximum velocity point. Quarmby [3] also believed the coincidence of positions of zero stress and maximum velocity. He employed a more accurate experimental method, i.e., the Preston-tube method, to identify the position of maximum velocity. Nevertheless, contrarily, Kjellström and Hedberg [4] reported that the zero shear stress is not coincident with the position of maximum velocity in the annulus with rough inner

walls. Subsequently, Lawn and Elliott [5] employed hot-wire technology to measure the shear stress and experimentally showed for the first time that there was a shift between the positions of maximum velocity and zero shear stress. Rehme [6] drew the same conclusion in his study and explained that the position of zero shear stress was closer to the inner wall than that of the maximum velocity. Nouri et al. [7] also experimentally demonstrated that these two positions did not overlap.

Recently, with the rapid enhancement of computational power, numerical simulations have become an important tool for turbulence analysis in concentric annuli. Many simulation studies have been focused on the effects of curvature on the turbulent structure in concentric annuli. Satake and Kawamura [8] conducted a Large Eddy Simulation (LES) for flow in a concentric annulus with three different radius ratios, aiming at characterizing the vortical structure near the inner wall. Their results demonstrated that for a small radius ratio ($\theta = R_1/R_2$), the turbulent structure near the inner wall was similar to that of turbulent flow around a cylinder. Direct Numerical Simulation (DNS) of similar flow scenario by Neves et al. [9] suggested that the turbulent structure near the outer wall for a small radius ratio was comparable with that of a turbulent pipe flow. Moreover, Neves et al. concluded that the slope of the mean velocity profile in the logarithmic region, turbulence intensities and the Reynolds stress decrease with an increase of curvature. Chung et al. [10] performed a DNS of turbulent flow in annuli with two different radius ratios at $Re = 8900$ and compared their results with experimental results of Nouri et al. Apart from the velocity profile and shear stress, they carefully analyzed the effect of curvature on the kinetic energy budget of turbulent

flow. Liu and Lu [11] performed an LES with a fixed radius ratio and various Reynolds numbers in an effort to investigate the influence of Reynolds numbers on high order turbulent statistics, including the viscous dissipation.

A meticulous literature review indicates that the simulation of complex turbulent flows using Reynolds-averaged Navier-Stokes (RANS) model is more attractive in terms of its balance between accuracy and computational efficiency [12]. To better identify the near-wall turbulence structures and clarify the effects of curvature and the Reynolds number on the development of the turbulent structures, a systematic study of turbulence in concentric annuli was undertaken in this work using ANSYS-CFX with a built-in RANS model. Computational Fluid Dynamics (CFD) simulations were carried out for fully turbulent flow in the horizontal annulus. Simulation results were compared with experimental results reported by Nouri. et al. [7] and Corredor et al. [13] as well as DNS results of Chung et al. in annulus channels [10]. This study also elaborately discussed the mean velocity profiles, Reynolds stresses, average vorticity, and the turbulent kinetic budget of fully developed turbulent Newtonian flow in concentric annuli. Good agreements between present results and those from literature demonstrate the reliability of the RANS model for predicting near-wall turbulence for wall-bounded flow.

3.2 Numerical Procedures

3.2.1 Governing Equations

3.2.1.1 Reynolds-averaged Navier-Stokes Equations (RANS)

In the RANS formulation, turbulent variables are decomposed into a time-averaged component and a time-fluctuating component:

$$\hat{\phi}_i = \phi_i + \varphi_i \quad \text{with} \quad \phi_i = \frac{1}{\Delta t} \int_t^{t+\Delta t} \phi_i dt \quad (3-1)$$

By applying the decomposition and averaging operations of the velocity to the original Navier-Stokes equations, the continuity and the momentum conservation equations for steady-state problems can be converted into the following expressions:

$$\nabla \cdot \mathbf{U} = 0 \quad (3-2)$$

$$\frac{\partial}{\partial x_j} (\rho U_i U_j) = -\frac{\partial P}{\partial x_i} + \frac{\partial}{\partial x_j} \left[\mu \left(\frac{\partial U_i}{\partial x_j} + \frac{\partial U_j}{\partial x_i} \right) - \rho \overline{u_i u_j} \right] \quad (3-3)$$

The term $\rho \overline{u_i u_j}$ in Eq. (3-3) is the turbulent flux term called Reynolds stress. It is apparent that only the mean velocity field is solved in the RANS model, while the effects of the fluctuating turbulent velocity on the entire flow field are represented by Reynolds stress, a covariance velocity obtained from the averaging operation over the Navier-Stokes equations. To accurately characterize the turbulent structures using the RANS model, a proper turbulence model needs to be used. A most used turbulence model in CFD is the eddy viscosity model based on Boussinesq's hypothesis [14], in which the Reynolds stress is related to the mean velocity gradient and eddy viscosity by the gradient diffusion hypothesis.

3.2.1.2 Shear Stress Transportation (SST) Model

Selections of turbulence models significantly influence the turbulent structure of the flow field predicted by the CFD code. The standard SST model of Menter [15], based on Boussinesq's hypothesis, is adopted in the present study for the estimation of Reynolds stress since it combines the advantages of both k - ε and k - ω models. With specially defined blending functions, the SST model transfers successfully from a Low Reynolds Number (LRN) formulation (available in the standard k - ω model) in the near-wall boundary layer to the k - ε formulation in the free shear layer. The development of this model is encouraged based on the fact that the near-wall treatment of LRN in the k - ω model requires less resolution effort and avoids the use of non-linear damping functions specified in the k - ε model, but is much more sensitive to free-stream boundary conditions [16].

The SST model employs two transportation equations [17], one for turbulent kinetic energy k , m^2/s^2 (the variance of the fluctuations in velocity), and the other for turbulent frequency ω , $1/s$. The relationship between k , ε and ω can be found in Eq. (3-4):

$$\varepsilon = C_\mu k \omega \quad (3-4)$$

where ε , m^2/s^3 , is the rate at which the velocity fluctuations dissipate and C_μ is a dimensionless model constant, (-).

k -equation:

$$\frac{\partial}{\partial x_j} (\rho U_j k) = \frac{\partial}{\partial x_j} \left[\left(\mu + \frac{\mu_t}{\sigma_k} \right) \frac{\partial k}{\partial x_j} \right] + \widetilde{P}_k - \beta' \rho k \omega \quad (3-5)$$

where

$$\widetilde{P}_k = \min (P_k, C_{lim} \rho \varepsilon) \quad (3-6)$$

ω -equation [18]:

$$\frac{\partial}{\partial x_j}(\rho U_j \omega) = \alpha \rho \left(\frac{\partial U_i}{\partial x_j} + \frac{\partial U_j}{\partial x_i} \right)^2 + \frac{\partial}{\partial x_j} \left[\left(\mu + \frac{\mu_t}{\sigma_\omega} \right) \frac{\partial \omega}{\partial x_j} \right] - \rho \beta \omega^2 + \frac{2\rho(1-F_1)}{\omega \sigma_{\omega 2}} \frac{\partial k}{\partial x_j} \frac{\partial \omega}{\partial x_j} \quad (3-7)$$

The modified shear production term \widetilde{P}_k introduced by Menter [15] is employed here to avoid the excessive generation P_k of turbulent energy, m^2/s^2 , in the vicinity of stagnation points, generated by the k - ω model. The dimensionless production limiter C_{lim} has a value of 10 for the standard ω based model and does not influence the shear layer performance of the model.

Table 3- 1 Coefficients in the SST model

α_1	β_1	$\sigma_{\omega 1}$	σ_{k1}	c_1	λ	a_1
$\beta_1/\beta - \lambda^2/(\sigma_{\omega 1}\sqrt{\beta'})$	0.075	2.0	1.176	0.31	0.41	0.31
α_2	β_2	$\sigma_{\omega 2}$	σ_{k2}	β'	C_μ	
$\beta_2/\beta' - \lambda^2/(\sigma_{\omega 2}\sqrt{\beta'})$	0.8282	1.168	1.0	0.09	0.09	

As discussed above, the SST model is a combination of k - ε and k - ω models; thus, any index α used in this model is calculated directly from corresponding coefficients of those two models and the specially defined blending functions as shown in Eq. (3-8), which ensures a smooth transition from the k - ω model near the wall to the k - ε model away from it. The definitions and default values of the model coefficients are summarized in Table 3-1.

$$\alpha = F_1 \alpha_1 + (1 - F_1) \alpha_2 \quad (3-8)$$

$$F_1 = \tanh(\text{arg}_1^4) \quad (3-9)$$

$$\text{arg}_1 = \min \left[\max \left(\frac{\sqrt{k}}{\beta' \omega y}, \frac{500\nu}{y^2 \omega} \right), \frac{4\rho k}{\sigma_{w2} CD_{k\omega} y^2} \right] \quad (3-10)$$

$$CD_{k\omega} = \max \left(\frac{2\rho}{\sigma_{w2} \omega} \frac{\partial k}{\partial x_j} \frac{\partial \omega}{\partial x_j}, 10^{-10} \right) \quad (3-11)$$

$$F_2 = \tanh(\text{arg}_2^2) \quad (3-12)$$

$$\text{arg}_2 = \max \left(\frac{2\sqrt{k}}{\beta' \omega y}, \frac{500\nu}{y^2 \omega} \right) \quad (3-13)$$

$$S = \sqrt{2S_{ij}S_{ij}} \quad (3-14)$$

where S_{ij} is the shear strain tensor and can be expressed as:

$$S_{ij} = \frac{1}{2} \left(\frac{\partial U_i}{\partial x_j} + \frac{\partial U_j}{\partial x_i} \right) \quad (3-15)$$

The eddy viscosity can be expressed as:

$$\nu_t = \frac{a_1 k}{\max(a_1 \omega, SF_2)} \quad (3-16)$$

Finally, the Reynolds stress can be estimated by:

$$-\rho \overline{u_i u_j} = 2\mu_t S_{ij} \quad (3-17)$$

3.2.1.3 Near-Wall Treatment

The main challenge for modelling a wall-bounded flow using RANS lies in the characterization of the near-wall flow field in which the viscous effect is significant. The idea of the “wall-function” approach was first introduced by Launder and Spalding [19] with an aim to reduce the complexity of the near-wall treatment; for instance, the non-linear damping functions for the k - ε model. In this approach, a boundary condition was built up in the log-law region based on empirical relations. With the presence of this boundary, one has the ability to model the flow field between the wall and the location where the boundary condition is applied by using an empirical wall-function.

This approach is always utilized in statistical turbulence simulations. However, due to the mass and momentum balances in the viscous sub-layer being unknown, such an approach causes significant accuracy problems in flows where the entire flow field is very influenced by the near-wall turbulence structure [20]. As a result, since this structure plays a key role in the present study, an advanced near-wall treatment available in ANSYS-CFX has been applied. This treatment takes advantage of $k-\omega$ and transfers automatically from the near-wall function to the LRN formulation once the mesh is refined [16]. By doing so, depending on the demand, one has the ability to choose whether to refine the mesh, in order to get more precise information of the near-wall turbulence structures or to apply coarse mesh only for obtaining the bulk flow characteristics, without addressing the mesh consistency issue. Note that in order to benefit from the LRN formulations, the near-wall mesh should be strictly refined, with the first mesh point located exactly in the viscous sub-layer. The details of this treatment can be expressed as follows:

Flux of momentum equation:

$$F_U = -\rho u_t u^* \quad (3-18)$$

where

$$u^* = \sqrt[4]{\left(\frac{\mu}{\rho} \left| \frac{\Delta U}{\Delta y} \right| \right)^4 + (a_1 k)^4} \quad u_t = \sqrt[4]{(u_t')^4 + (u_t'')^4} \quad \text{and}$$

$$u_t' = \sqrt{\frac{\mu}{\rho} \left| \frac{\Delta U}{\Delta y} \right|} \quad u_t'' = \frac{U}{1/\lambda \log(y^+) + 5.2}$$

Flux of the k -equation:

$$F_k = 0 \quad (3-19)$$

An algebraic expression for ω is specified from the viscous sub-layer to the logarithmic region as follows:

$$\omega' = \frac{6\nu}{\beta_1(\Delta y)^2} \quad (3-20)$$

$$\omega'' = \frac{u^{*2}}{a_1\lambda\nu y^+} \quad (3-21)$$

$$\omega^* = \omega'' \sqrt{1 + \left(\frac{\omega'}{\omega''}\right)^2} \quad (3-22)$$

3.2.2 Problem Setup

Steady-state simulations were performed in a 3D geometry. Momentum equations for each velocity component, the Poisson equation for pressure, and transportation equations for turbulence variables are solved with a high-resolution scheme for turbulence and advection terms. The mass flow rate of water with turbulent intensity of 5% was specified at the inlet, while the outlet boundary condition was set to be static pressure of the atmosphere. The no-slip condition was assumed for both walls of the annulus (inner and outer). Simulations were considered to be converged when scaled residuals (continuity, velocities in x , y , z dimensions, k , and ω) fell below 10^{-6} .

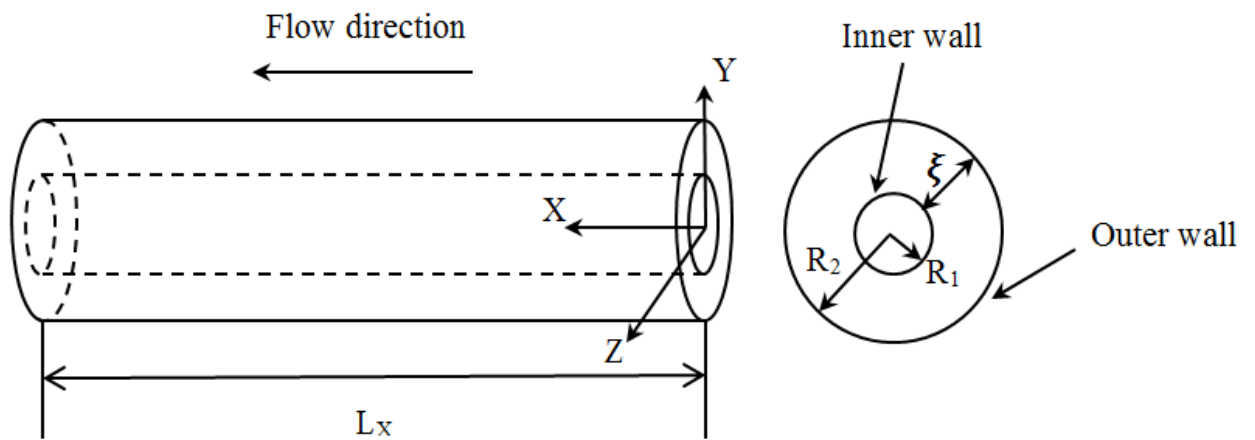


Fig. 3- 1 Scheme of Test Geometry and Coordinate System

The computational grid was defined by 12,192,342 unstructured Hexa cells generated by the multi-zone method, supplemented by the inflation method for the wall boundary and the sizing method for the inlet and outlet boundaries, in order to ensure a smooth transition from the near-wall region to the outer-wall free shear region. Note that the vicinity of the annuli centre was occupied by a refined mesh instead of a coarse one, in order to analyze the locations of the maximum axial velocity and the zero shear stress. The first point of the inflation method was located at $y^+=0.7$, and eight layers were placed within the viscous sub-layer, where $y^+<10$.

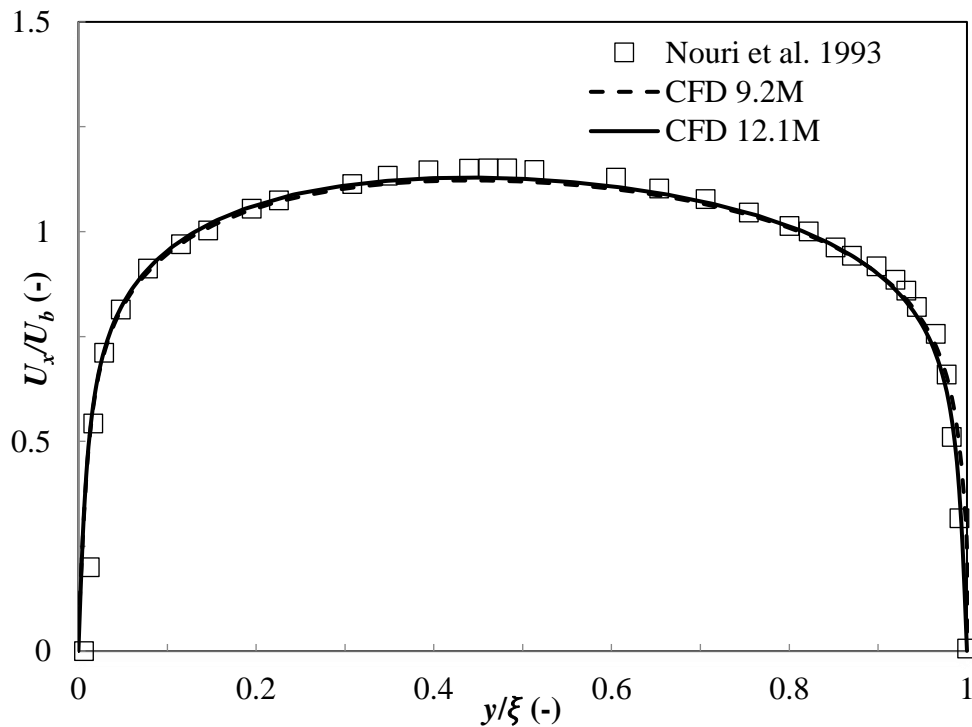


Fig. 3- 2Mesh Independence Test

Before proceeding further, a mesh independency test was given to estimate the accuracy of the meshing method discussed above. Results were compared with experimental results reported by Nouri and Whitelaw [7]. Average velocity, normalized by average bulk velocity U_b , was calculated at $Re=26600$ based on the bulk velocity and the hydraulic diameter for fully turbulent flow in an annulus with $\theta = 0.5$.

Simulation results are shown in Fig. 3-2. According to this figure, our results are in good agreement with the experimental data, which indicates that the present model is sufficiently accurate to support the analysis.

3.3 Results and Discussions

The simulation was carried out with two radius ratios ($\theta = 0.4$ and 0.5) while flow with three different Reynolds numbers ($Re = 8900, 26600$ and 38700) were investigated in order to reflect the influence of the Reynolds number.

3.3.1 Average Axial Velocity

The near-wall axial velocity, normalized by friction velocity $u_\tau = \sqrt{\tau_w/\rho}$, is plotted against the wall unit $y^+ = \rho y u_\tau / \mu$ suggested by [21], in Fig. 3-3, where y is the radial distance from the nearest wall. τ_w was the wall shear stress, which was calculated by equations suggested by [7]:

$$\tau_w \text{ inner wall} = -\frac{\Delta P}{L_x} \left(\frac{r_0^2 - r_{in}^2}{2r_{in}} \right) \quad (3-23)$$

$$\tau_w \text{ outer wall} = -\frac{\Delta P}{L_x} \left(\frac{r_{out}^2 - r_0^2}{2r_{out}} \right) \quad (3-24)$$

Several mean flow parameters obtained in the present study are shown in Table 3-2. CFD results show good agreement with experimental data from [7] and [13]. Both results have been found to concur with the law of the wall [22], except data from [7], which shows a slight over-estimate of axial velocity in the logarithmic zone, where $y^+ > 30$. As seen in Fig. 3-2, for flow in the annuli, the location of the maximum axial velocity r_0 is no longer in the pipe centre. Therefore, the wall shear stresses calculated by Eq. (3-23) and (24) for the inner and outer wall are different, leading to different axial velocities for the law of the wall U^+ . Fig. 3-3 suggests that U^+ near the outer wall

is slightly larger than that at the inner wall due to the curvature effect, which is consistent with the results reported by [10] and [23].

Table 3- 2 Mean Flow Parameters

θ	0.5		0.4
Re	8900	26600	38700
$Re_{\tau}(inner)$	608	1503	2188
$Re_{\tau}(outer)$	580	1479	2028
$C_f(inner)$	0.00934	0.00639	0.00651
$C_f(outer)$	0.00852	0.00619	0.00560
$-K_P(inner)$	0.00673	0.00272	0.00164
$-K_P(outer)$	0.00729	0.00286	0.00206

In order to further investigate the curvature effect, mean axial velocity profiles along the whole cross-section of annuli at different inner and outer radius ratios are compared in Fig. 3-4. As seen in Fig. 3-4, velocity profiles are asymmetric, tilting towards the inner wall for both cases. Due to the presence of skewness, maximum axial velocities appear in locations close to the inner wall. Additionally, these locations move closer to the inner wall with a decrease of the radius ratio from 0.5 to 0.4. Specifically, the maximum velocity is located at $y = 0.427\xi$ from the inner wall for $\theta = 0.4$ whereas it is located at $y = 0.434\xi$ for $\theta = 0.5$. A similar conclusion was drawn by Chung [10], who conducted a direct numerical simulation for the fully turbulent flow in concentric annular pipes with radius ratios of 0.1 and 0.5.

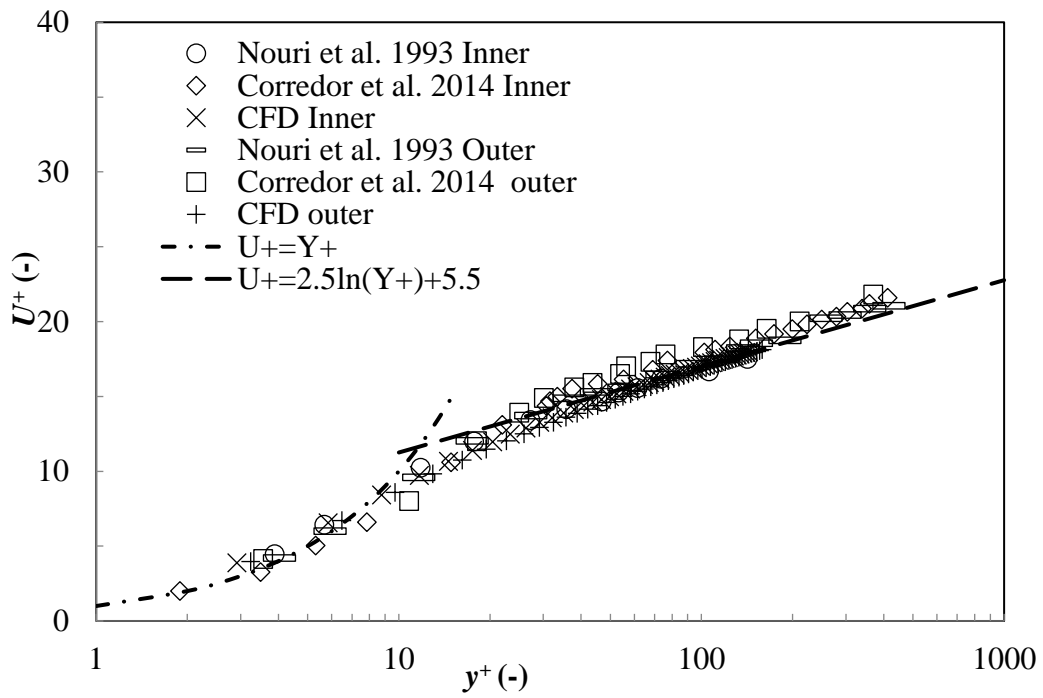


Fig. 3- 3 Axial Velocity at the Wall

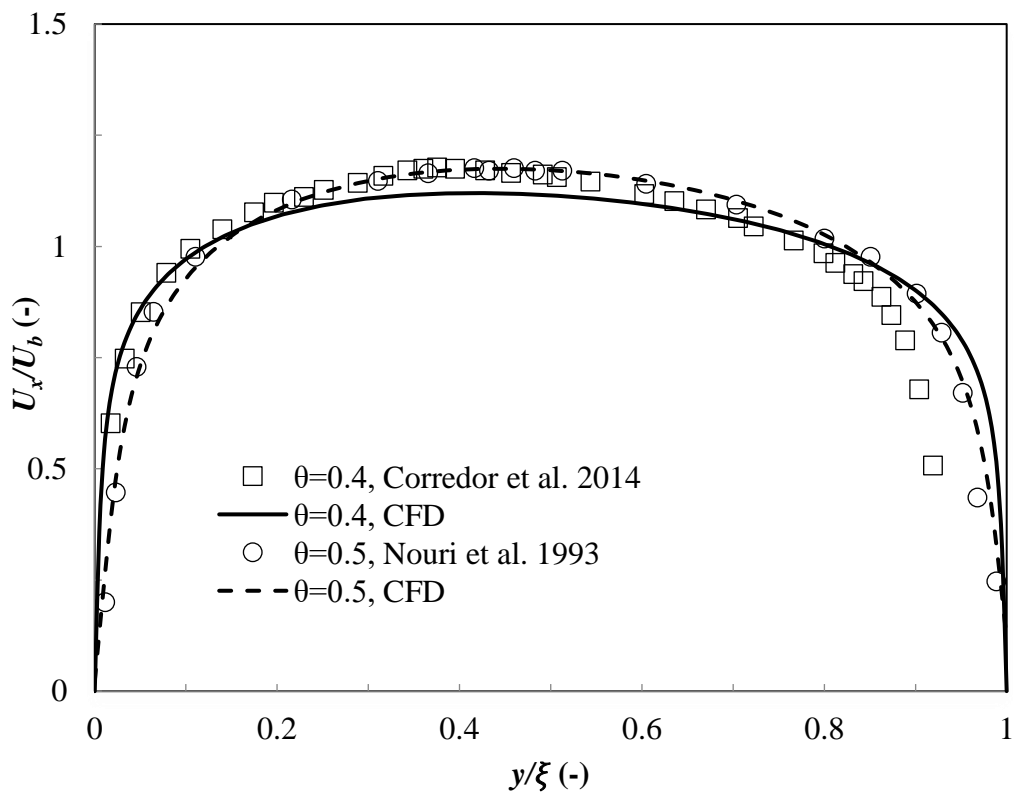


Fig. 3- 4 Axial Velocity for Different θ

The effect of Reynolds number on the axial velocity profile is demonstrated in Fig. 3-5. The thickness of the viscous sub-layer is decreased due to the increase in the Reynolds number, reflected by the increase in axial velocity in this layer, as seen in Fig. 3-5. Consequently, this change leads to a redistribution of axial velocity profiles, resulting in a movement of maximum axial velocity, which is consistent with Rehme's results [24]. Our simulation results indicate that the location of the maximum axial velocity moves closer to the inner wall, from 0.459ξ to 0.434ξ as the Reynolds number increases from 8900 to 26600 for $\theta = 0.5$. At the same time, the velocity distribution in the core region of the annulus becomes flatter as a result of this redistribution. This finding has also been noted by Liu et al. [11].

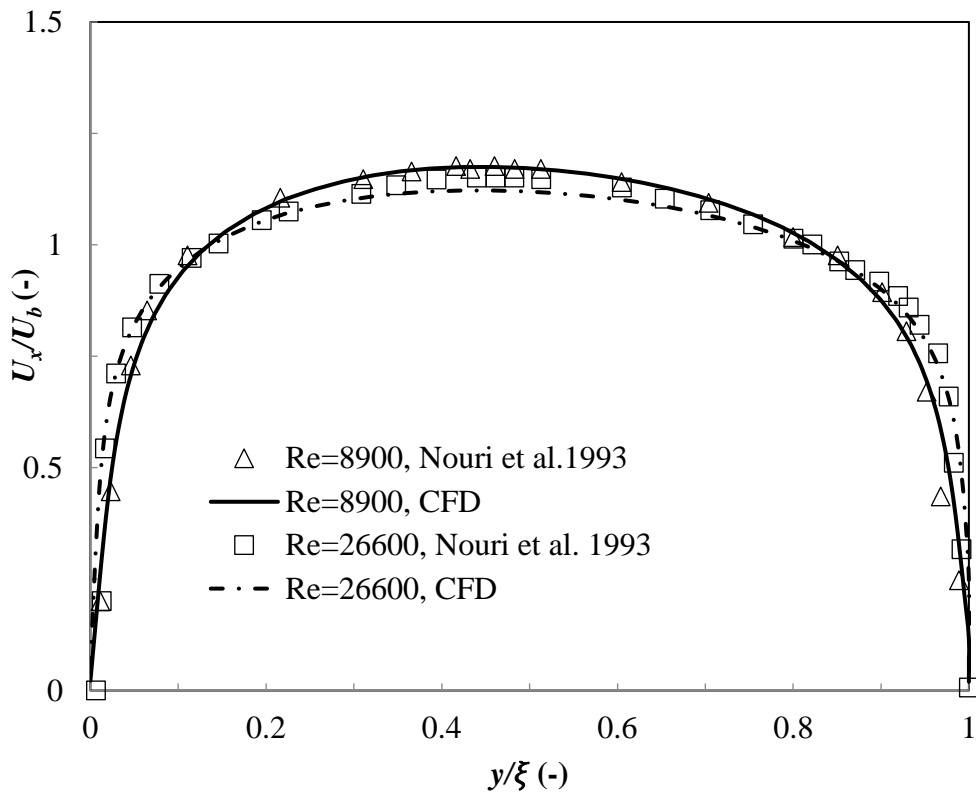


Fig. 3- 5 Axial Velocity for at Different Re

3.3.2 Reynolds Stress

Results of Reynolds stress, normalized by the local friction velocity are plotted in Fig. 3-6. The current simulation results show good agreement with data from the literature. Compared to the inner wall, the outer wall of the annulus has higher Reynolds stress, being more apparent when the radius ratio between the inner and outer θ becomes smaller.

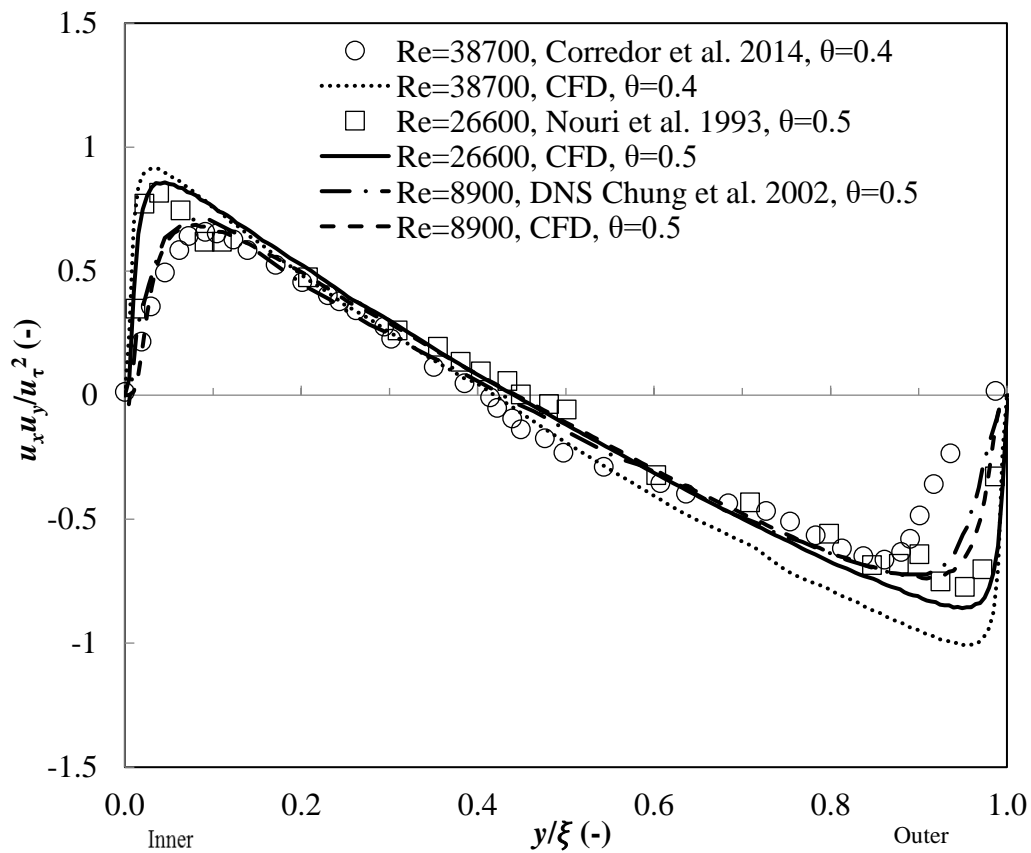


Fig. 3- 6 Reynolds Stress Distribution with Various Reynolds Numbers and Radius Ratios

This can be explained by the fact that the outer wall has a larger surface area to support higher turbulent energy [7, 10, 11]. For $\theta = 0.4$, the discrepancy in surface area between inner and outer walls becomes greater so that in Fig. 3-6 the annulus with

this ratio provides more distinguishable Reynolds stresses between the inner and outer walls. In addition, with an increase of the Reynolds number, a decay of the viscous sub-layer is also observed in Fig. 3-6, reflected as the boundary layer of the Reynolds stress becomes thinner, and the peak value the Reynolds stress moves closer to the wall, which is consistent with the findings from the axial velocity profiles.

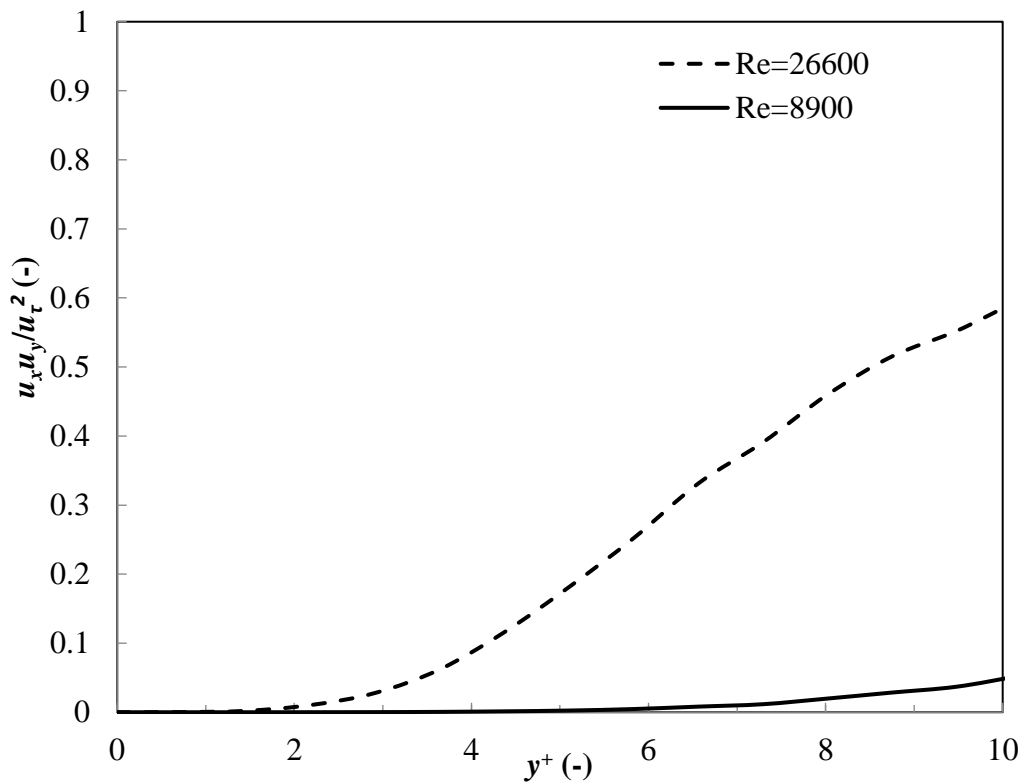


Fig. 3- 7 CFD results of Near-wall Reynolds Stresses for Different Reynolds Numbers

It is clear from the momentum equation that the frictional pressure gradient is related to both shear/viscous stress and turbulence/Reynolds stress. According to Moody's diagram, an increase in the Reynolds number will cause a decrease in the friction factor, leading to a decrease in pressure drop. Based on the present study, this decrease in pressure drop can be explained by the decrease in viscous stress due to the thinning of the viscous sub-layer near the wall. As discussed earlier, increasing the Reynolds number can cause this change; however, as shown clearly in Fig. 3-7, in a turbulent

flow, an increase in the Reynolds number contributes to a great rise in the Reynolds stress, which inversely leads to an increase in pressure drop. Based on this study, it is necessary to mention that for a fully turbulent flow with a relatively high Reynolds number, turbulence plays a dominant role in determining the pressure drop. As a result, in such a condition, an increase of Reynolds number has a positive influence on increasing the pressure gradient.

As noted in [11] and shown in Fig. 3-6, Reynolds stresses in the core region of the annuli appear to be linear, and the slope of Reynolds stresses increases with the increase in the Reynolds number. Change of the slope can be interpreted by Kolmogorov's hypothesis [25], in which the turbulent energy cascade has been elucidated both qualitatively and quantitatively in detail. According to this hypothesis, turbulent eddies break down from large pieces to small pieces while energy transfers from larger eddies to smaller eddies, until they reach a scale small enough to be dissipated, called viscous dissipation. Turbulent energy cannot be dissipated unless it is on this scale. The viscous sub-layer existing in the wall-bounded flow is an ideal place for such dissipation since in this layer, not only is the viscous effect strong enough but also the turbulence scale meets the requirement for viscous dissipation. In this regard, the Reynolds number plays an important role in the dissipation process as it determines the thickness of the viscous sub-layer near the wall. As illustrated in Fig. 3-7, Reynolds stress starts to increase at $y^+ = 2$ for $Re = 26600$, whereas it remains invariably tiny until $y^+ = 9$ for $Re = 8900$, which indicates a thinner viscous sub-layer is being generated by the flow with a larger Reynolds number. Consequently, more turbulence accumulates in the buffer

layer as the Reynolds number increases, reflected by a higher peak of Reynolds stress in the near-wall region as shown in Fig. 3-6. Finally, a higher slope is generated at the linear region in the profile of Reynolds stress to balance its accumulation within the near-wall region.

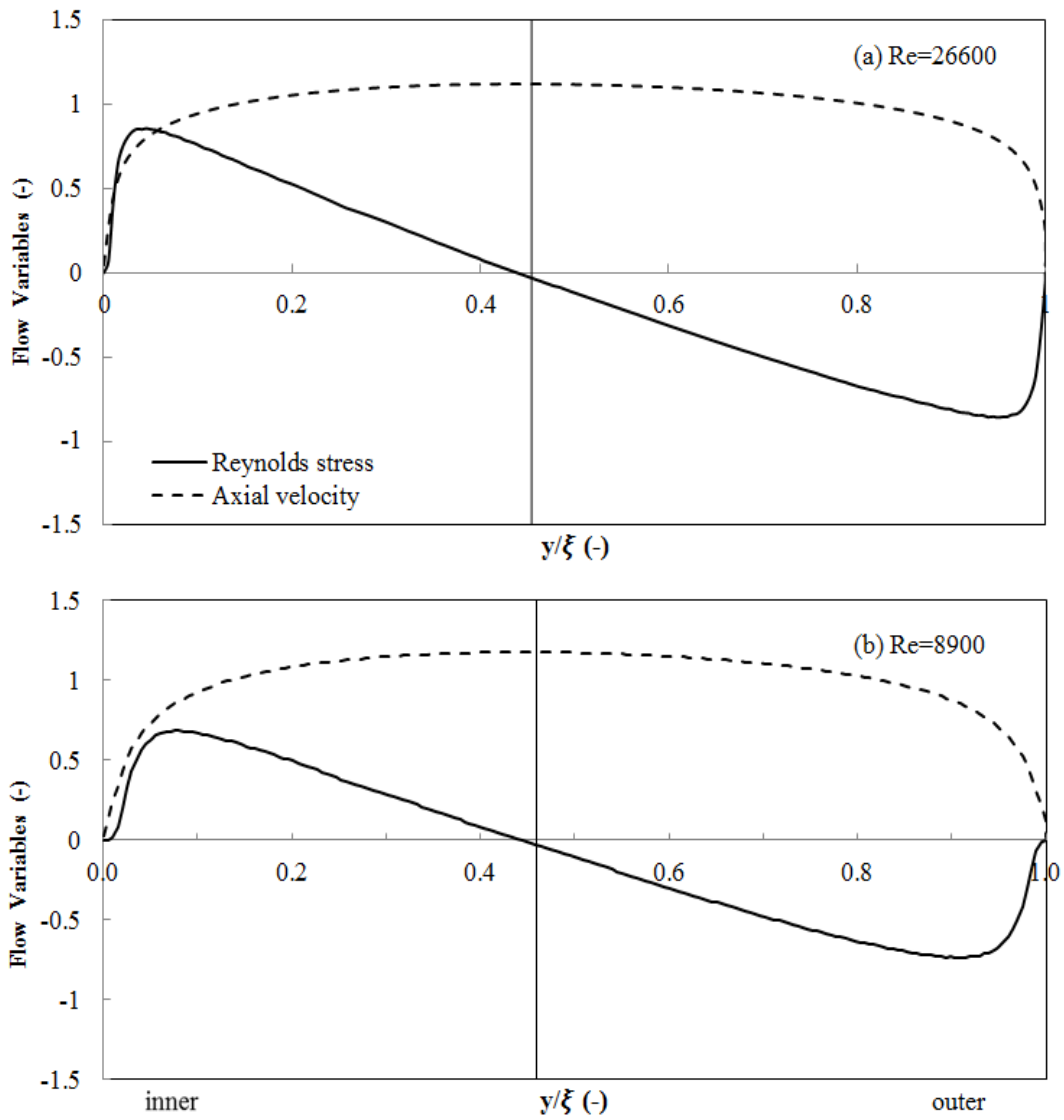


Fig. 3- 8 Locations of Maximum Axial Velocity and Zero Reynolds Stress for Different Re

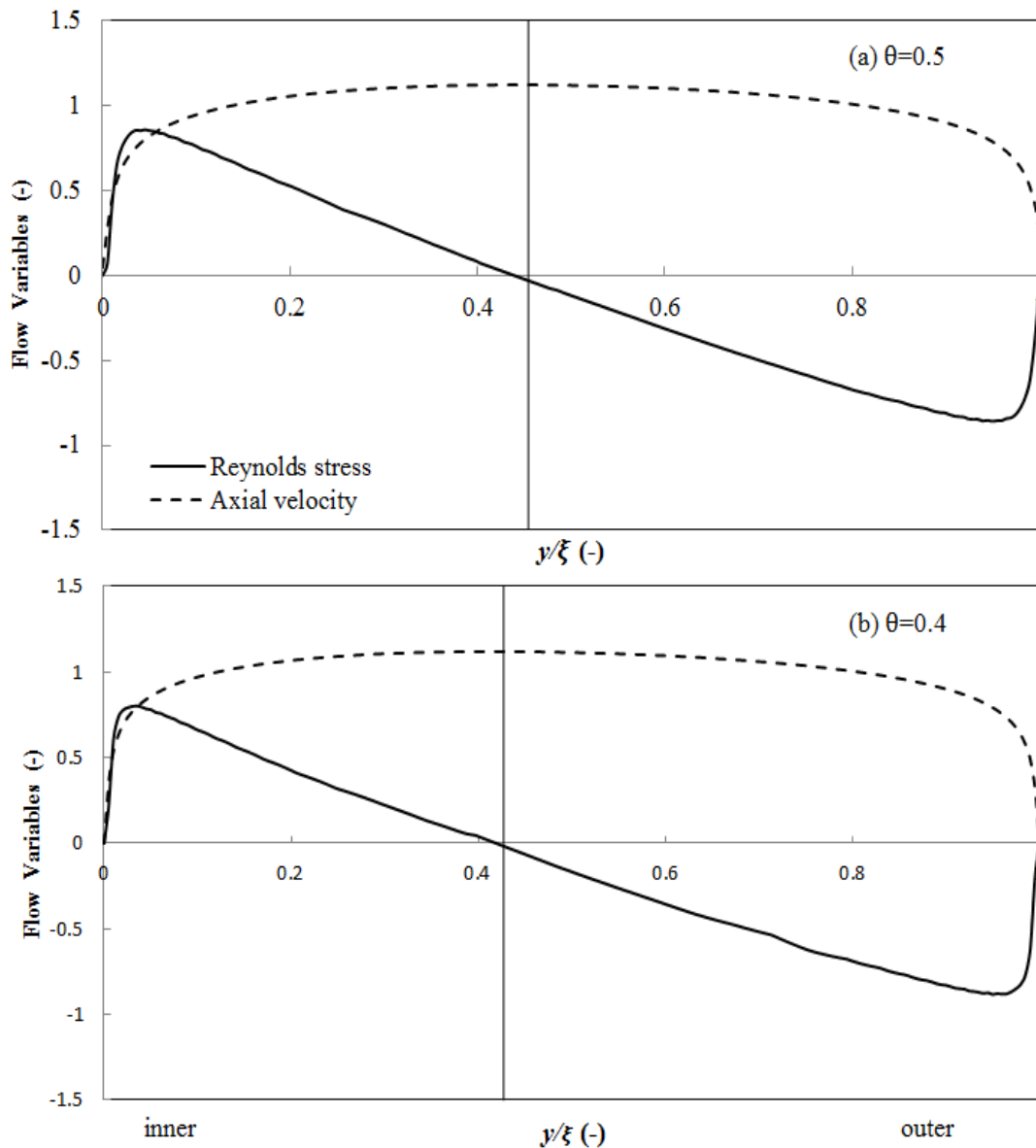


Fig. 3- 9 Locations of Maximum Axial Velocity and Zero Reynolds Stress for Different θ

3.3.3 Locations of Maximum Axial Velocity and Zero Reynolds Stress

As discussed earlier, there is a controversy with respect to the coincidence of the positions of zero shear stress and maximum velocity for turbulent flow in concentric annuli. According to Rheme [6], the effect of geometry on the velocity profile is the main cause of the non-coincidence between zero shear stress and maximum velocity.

Our results, as shown in Fig 3-8, illustrate that with an increase in the Reynolds number, both the velocity and Reynolds stress profiles move only slightly towards the inner wall while apparent movement is noted in Fig. 3-9 for both profiles as the radius ratio θ decreases from 0.5 to 0.4. This observation indicates that the Reynolds stress and axial velocity are quite sensitive to the curvature effect. Further, according to the simulation results, both the maximum axial velocity and zero Reynolds stress move closer to the inner wall with a decrease in the radius ratio, and a minor shift was observed from Figs 3-8 and 3-9 between these two positions.

3.3.4 Turbulent Kinetic Energy Budget

Equations for the turbulent kinetic energy have been suggested by Pope [26] as follows:

$$\frac{D(k)}{Dt} = -\frac{\partial}{\partial x_j} \left(\frac{1}{2} \overline{u_i u_j u_j} + \frac{\overline{u_i (\hat{P}-P)}}{\rho} - 2\nu \overline{u_j s_{ij}} \right) + \overline{u_i u_j} \frac{\partial U_i}{\partial x_j} - 2\nu \overline{s_{ij} s_{ij}} \quad (3-25)$$

where

$$s_{ij} = \frac{1}{2} \left(\frac{\partial u_i}{\partial x_j} + \frac{\partial u_j}{\partial x_i} \right) \quad (3-26)$$

The first three terms on the right-hand side represent the spatial transport of the turbulent kinetic energy. The first two terms represent the transport of turbulent kinetic energy by turbulence while the third term represents the viscous transport. The fourth term represents kinetic energy transferred from the mean flow field to the turbulent fluctuating field and is called shear production P_k . As shown in Eq. (3-25), this term is produced by an interaction between the mean shear strain and Reynolds stress. The last term in Eq. (3-25) represents viscous dissipation term ε of turbulent kinetic energy. As discussed earlier, viscous dissipation is the only way that kinetic energy can be

dissipated. Since the last two terms are of great importance, they will be discussed in detail.

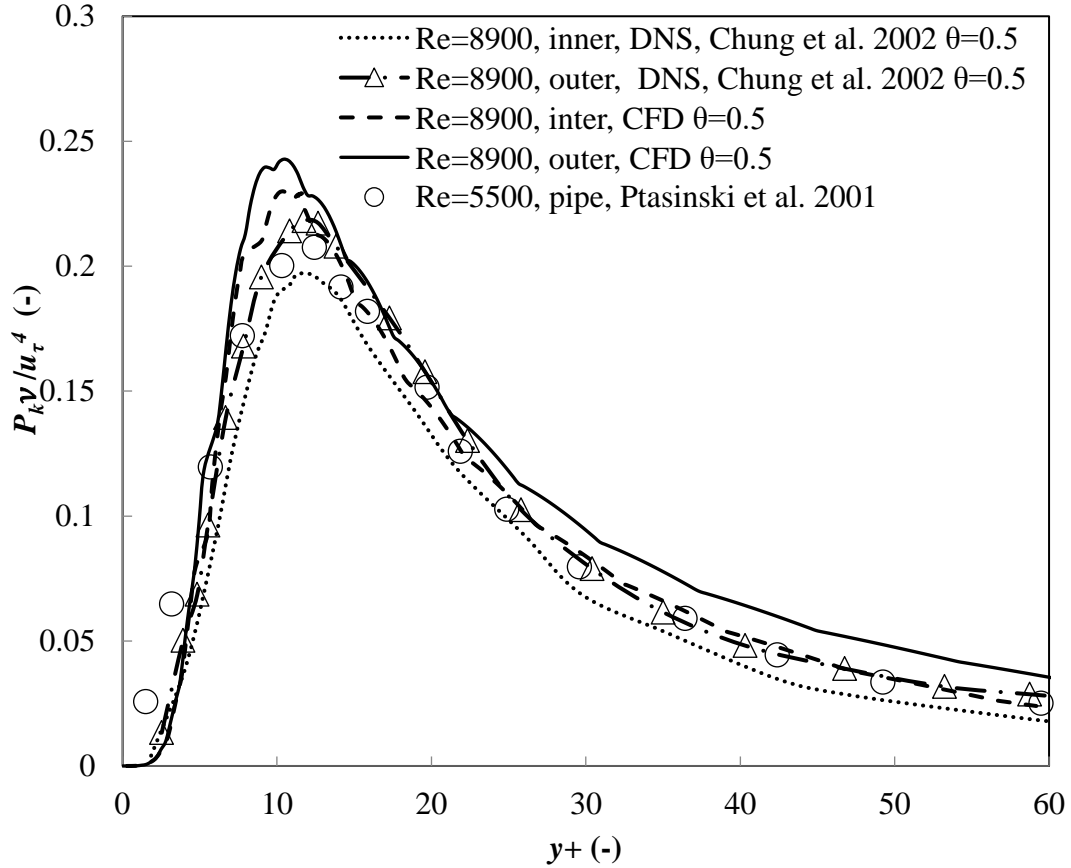


Fig. 3- 10 Shear Production for $\theta = 0.5$ Compared with Pipe Flow

3.3.4.1 Shear Production

Based on the turbulent-viscosity hypothesis, the shear production term P_k is computed by:

$$P_k = 2\nu_t \bar{S}_{ij} \bar{S}_{ij} \quad (3-27)$$

where ν_t is the eddy viscosity, m^2/s , and can be calculated directly by Eq. (3-16). Fig. 3-10 and 3-11 show the production terms predicted by the present CFD code and results from literature e. For both cases, shear production increases from the wall, reaches the maximum value in the buffer zone between $y^+ = 10$ and $y^+ = 13$ and then decreases

when approaching the outer wall region. A high production level appears at the outer wall due to larger surface areas, as discussed previously.

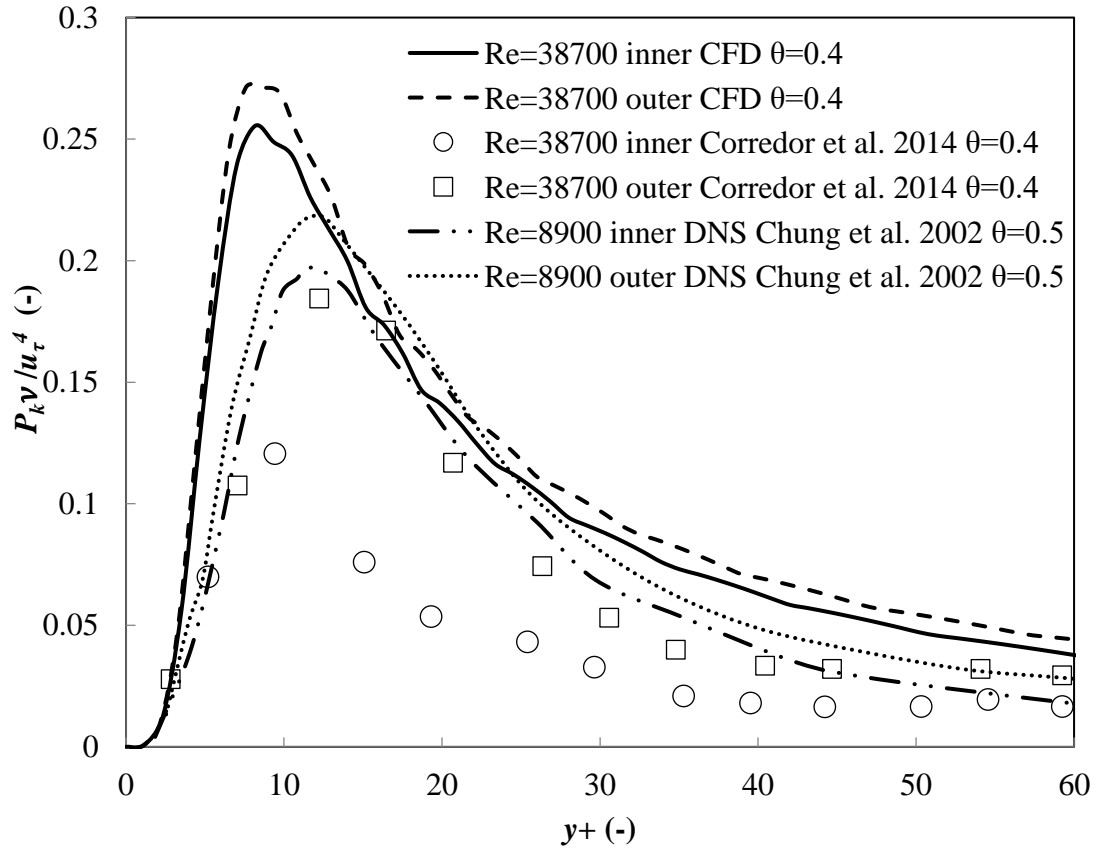


Fig. 3- 11 Shear Production Term for Different θ and Re

CFD results indicate that the Reynolds number has an insignificant influence on the location of maximum production. Both results from this study and literature show that this location remains the same for shear production profiles at the inner and outer walls of the annuli, except the results from Corredor's report, which states that the peak shear production appears slightly closer to the inner wall. Additionally, no apparent change has been observed for the location of the maximum shear production when the radius ratio is reduced from 0.5 to 0.4, which has also been mentioned in [10].

3.3.4.2 Viscous Dissipation

The combination of Eq. (3-4), (3-5), and (3-7) in the SST model serves as a way to calculate the viscous dissipation term ε in the turbulence kinetic budget. It is important to note that the transportation equation of the turbulence frequency ω , Eq. (3-7), is not a direct derivation of viscous dissipation from the exact equation but contrarily an empirical correlation [26]. Since viscous dissipation is best viewed as an energy transfer rate in the energy cascade concept, it is determined by large-scale motions and is independent of the viscosity in large Reynolds numbers. However, the exact equation of viscous dissipation requires scales to be in the dissipative range, which is hard to model. Viscous dissipation calculated by CFD is shown in Fig. 3-12 and compared with available data from the literature.

CFD results show the same trend as the DNS data for the viscous dissipation term in the log-law region ($y^+ > 30$). However, different shapes of viscous dissipation profiles appear in the viscous sub-layer ($y^+ < 10$), where DNS data show a continuous increase in viscous dissipation while CFD results show a slight decrease. This difference can be related to the report of Härtel et al. [27], in which they claimed that there was an inverse cascade of turbulent kinetic energy occurring in the buffer layer for the wall-bounded flow. Invoking Kolmogorov's hypothesis, it is reasonable to believe that this inverse cascade of kinetic energy in the buffer layer is caused by a significant inverse transfer of turbulent eddies from small pieces to large pieces. According to this hypothesis, kinetic energy contained in large turbulent eddies cannot be dissipated but is transferable. Due to the inverse transfer of turbulent eddies, less turbulent energy exists

in the proper scale for viscous dissipation within the buffer layer. Consequently, less kinetic energy is expected to be dissipated in this layer.

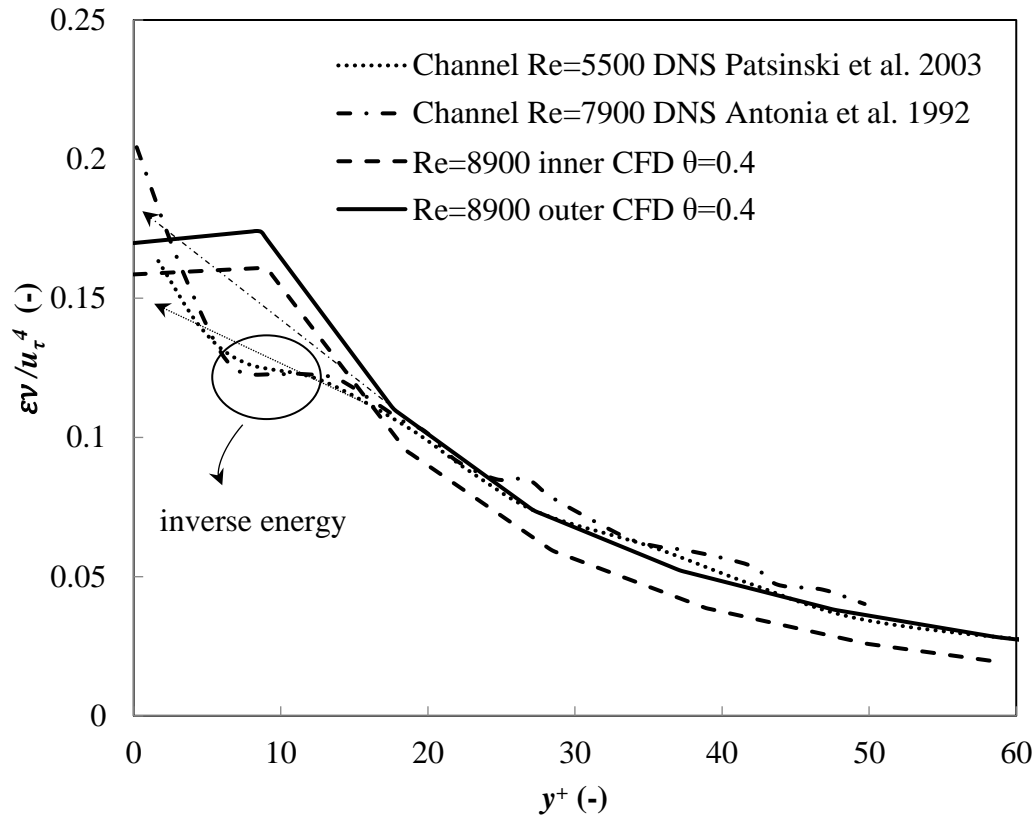


Fig. 3- 12 Viscous Dissipation Term for Different Re

Reflected in Fig. 3-12, the inverse transfer of energy results in a flat curve region in the viscous dissipation profile predicted by DNS, approximately from $y^+ = 10$ to $y^+ = 14$, between a sharply increasing trend in the viscous sub-layer and a gradually increasing trend in the outer layer. In spite of the fact that the strongest viscous effect exists in the viscous sub-layer, which leads to the largest viscous dissipation in this layer, the inverse energy cascade occurring in the buffer layer is believed to be another factor that dramatically enhances viscous dissipation in the viscous sub-layer.

Without the inverse energy cascade, the viscous dissipation profiles might obey the continuously increasing trends and follow the arrow lines drawn in Fig. 3-12. However,

with the presence of this energy cascade, less kinetic energy is dissipated in the buffer layer, whereas more kinetic energy is accumulated in the viscous sub-layer. Most important of all, the aggregated kinetic energy in the viscous sub-layer can be broken down due to the stronger viscous effect in this region. Conclusively, with more turbulent kinetic energy in proper scales for dissipation and the strongest viscous effect in the viscous sub-layer, the real profiles for the viscous dissipation term in this layer show distinctive slopes in Fig. 3-12.

The CFD code utilized in this study is unable to capture the inverse energy cascade in the buffer layer. A possible reason for this demerit is the employment of the empirical transportation equation for ω , which has been discussed in detail by Pope [26]. Besides, the viscous dissipation term in our simulation results is insignificantly dependent on Reynolds number as very tiny changes of this term are detected in Fig. 3-12 with relatively big changes in the Reynolds number.

Turbulent kinetic energy budgets consisting of shear production and viscous dissipation for flow in concentric annuli are plotted in Fig. 3-13 at $Re = 8900$. The figure shows that production and dissipation terms are within the same magnitude, while the peak of the production term is higher than that of the dissipation term, which is consistent with the results from [11] [28] [29]. Viscous dissipation for the outer wall is higher compared with that for the inner wall.

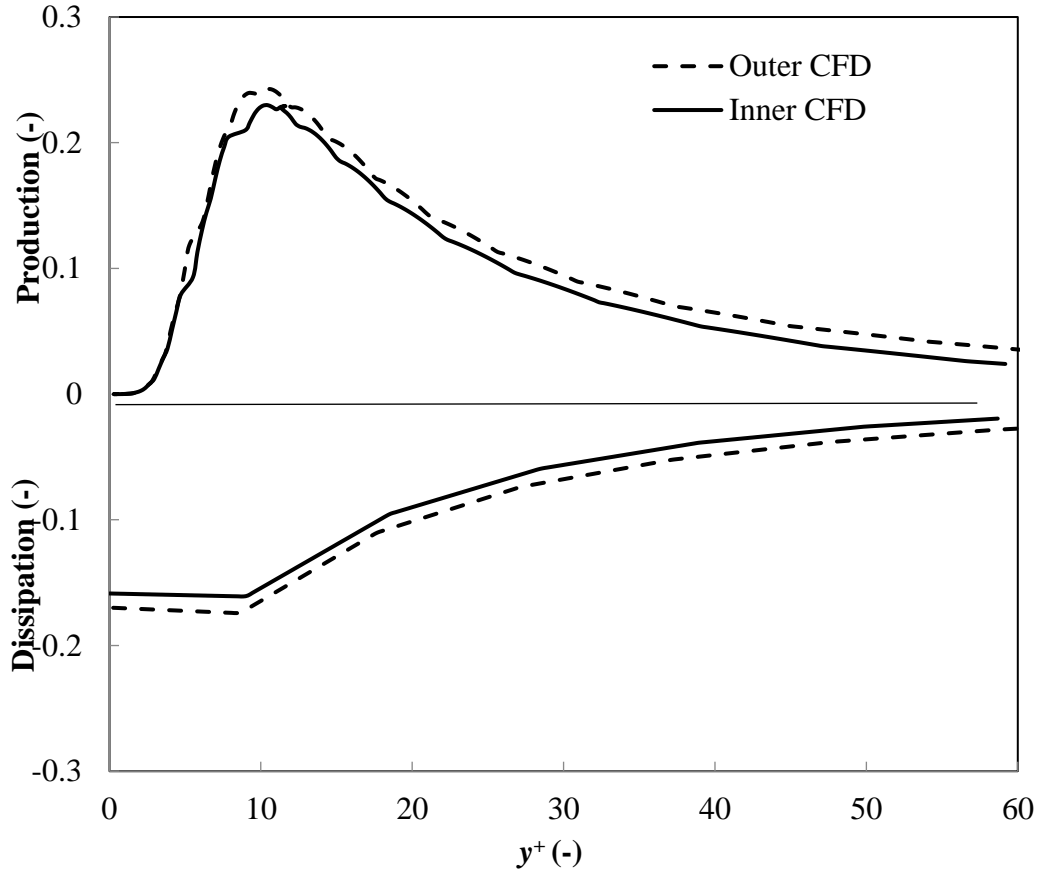


Fig. 3- 13 Turbulent Kinetic Energy Budget for $\theta = 0.5$ and $Re = 8900$

3.3.4.3 Vorticity

Vorticity is closely related to the turbulence production of turbulent kinetic energy [10]. In this study, the average vorticity can be calculated as:

$$\Omega_{xy} = \frac{1}{2} \left(\frac{\partial U_x}{\partial x_y} - \frac{\partial U_y}{\partial x_x} \right) \quad (3-28)$$

The average vorticity normalized by the wall shear stress is shown in Fig. 3-14 and compared to experimental results from [13]. Average vorticity has the highest value at the wall and continuously decreases away from the wall. According to Fig. 3-14, vorticity intensity near the outer wall is higher than that near the inner wall.

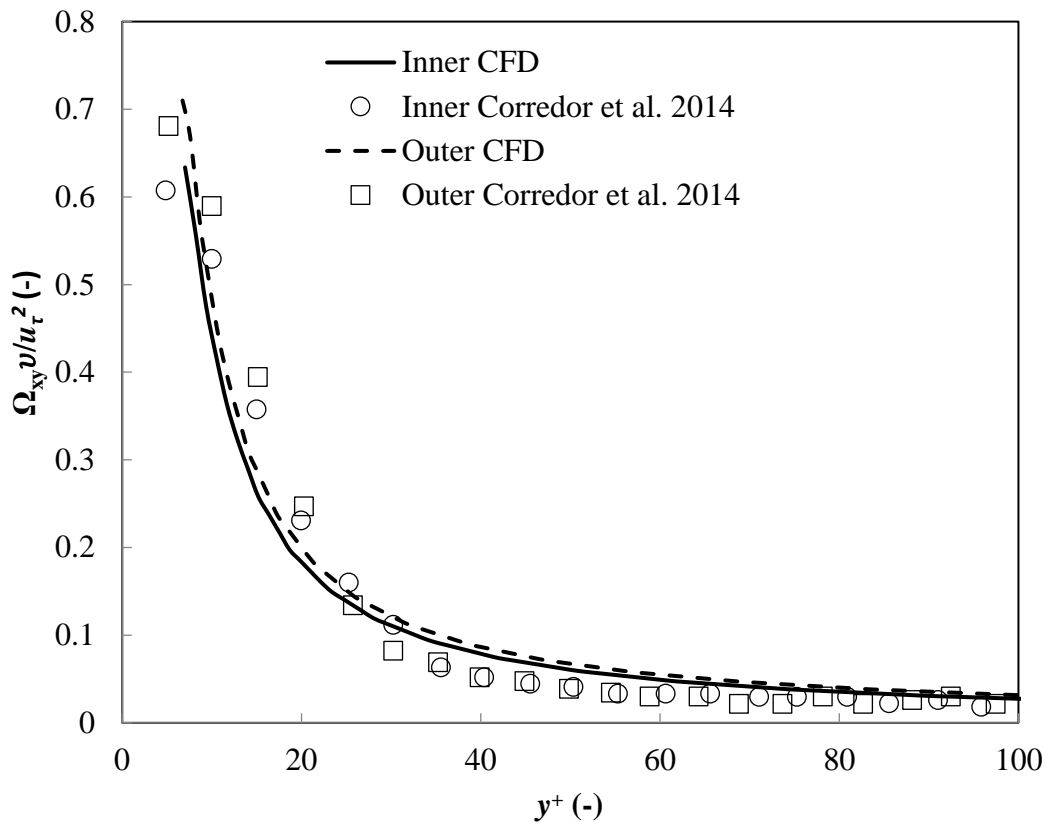


Fig. 3- 14Average Vorticities for $\theta = 0.4$ and $Re = 38700$

In order to relate the average vorticity to turbulence production, a vortex stretching mechanism has been introduced [10]. In this mechanism, for flows in concentric annuli, eddies that obtain energy more efficiently from the mean flow are expected to be vortices that appear more frequently near the outer wall. Since higher vortex intensity is obtained near the outer wall in Fig. 3-14, higher kinetic energy is expected to be generated there. This finding is consistent with the discrepancy between the inner and outer walls in Reynolds stress, and shear production discussed previously in the present study.

3.4 Conclusions

A detailed CFD study has been performed to analyze the near-wall turbulent structures for fully turbulent flow in the concentric annuli. Simulations were carried out for different Reynolds numbers ranging from 8900 to 38700 and with two radius ratios ($\theta = 0.4$ and 0.5). A mesh independent test was conducted prior to the analysis to ensure the accuracy of the meshing method. Mean axial velocity, Reynolds stress, turbulent kinetic energy budget, and average vorticity were discussed in this study.

Simulation results indicate that the RANS model is capable of capturing the curvature effect caused by annuli geometry. Due to this effect, the mean axial velocity profile of fully turbulent flow inside the concentric annuli is asymmetry and tilts towards the inner wall. The shape of the velocity profile is further influenced by the Reynolds number and the inner to outer radius ratio. The change of velocity profile in the near-wall region implies the decay of the viscous sub-layer that is caused by the increase of the Reynolds number. This phenomenon is also noted when investigating the near-wall structure of Reynolds stress. Also, Reynolds stress is estimated to be higher at the outer wall than at the inner wall since a larger surface area exists there to support higher turbulent energy. A minor shift between the position of zero Reynolds shear stress and the position of maximum axial velocity is numerically predicted in this study. Moreover, these locations are predicted to be less dependent on the Reynolds number but much more sensitive to the radius ratio.

Shear production and viscous dissipation terms of the turbulent kinetic energy are investigated in this study to expose the behavior of the kinetic energy field in the

annulus flow. Based on the results, higher Reynolds numbers leads to higher shear production. However, locations of the peak shear production appear to be independent of the Reynolds number as well as the radius ratio. Conversely, these locations are fixed near both the inner and the outer walls between 10 to 13 wall units. Again, shear production at the outer wall is higher than that at the inner wall. Viscous dissipation is predicted to be smaller than the shear production but at the same magnitude. The present RANS model fails to predict the inverse cascade of turbulent kinetic energy in the buffer layer, which is the main reason for the deviation between the viscous dissipation terms predicted by RANS and DNS. Simulation results of average vorticity match well with experimental data.

3.5 References

1. Germaine, E., Mydlarski, E., and Cortelezzi, L.: Evolution of the scalar dissipation rate downstream of a concentrated dye source in turbulent channel flow. *Journal of Fluid Mechanics*, **749**, 227-274 (2014).
2. Brighton, J. A., and Jones, J. B.: Fully developed turbulent flow in annuli. *Journal Basic Engineering D*, **86**, 835-844 (1964).
3. Quarmby, A.: On the use of the Preston tube in concentric annuli. *The Aeronautical Journal* **71**(673), 47-49 (1967).
4. Kjellström, B., and Hedberg, S.: On shear stress distributions for flow in smooth or partially rough annuli. A B Atomenergi, Stockholm Rep., AE-243 (1966).
5. Lawn, C. J., and Elliott, C. J.: Fully developed turbulent flow through concentric annuli. *Journal of Mechanical Engineering Science*, **14**, 195-204 (1972).

6. Rehme, K.: Turbulent flow in smooth concentric annuli with small radius ratios. *Journal of Fluid Mechanics*, **64**(2), 263-287 (1974).
7. Nouri, J. M., Umur, H., and Whitelaw, J. H.: Flow of Newtonian and Non-Newtonian fluids in concentric and eccentric annuli. *Journal of Fluid Mechanics*, **253**, 617-641 (1993).
8. Satake, S. and Kawamura, H.: Large eddy simulation of turbulent flow in concentric annuli with a thin inner rod. *Proceedings of the 9th Symposium on Turbulent Shear Flows*, 5.5.1-5.5.6 (1993).
9. Neves, J.C., Moin, P., Moser, R.D.: Effects of convex transverse curvature on wall-bounded turbulence. Part 1. The velocity and vorticity. *Journal of Fluid Mechanics* **272**, 349-382 (1994).
10. Chung, S.Y., Rhee, G.H., Sung, H.J.: Direct numerical simulation of turbulent concentric annular pipe flow: Part 1: Flow field. *International Journal of Heat and Fluid Flow* **23**(4), 426-440 (2002).
11. Liu, N. S., and Lu, X. Y.: Large eddy simulation of turbulent concentric annular channel flows. *International Journal for Numerical Methods in Fluids*, **45**, 1317-1338 (2004).
12. Kalitzin, G., Medic, G., Iaccarino, G., and Durbin, P.: Near-wall behavior of RANS turbulence models and implications for wall functions. *Journal of Computational Physics*, **204**, 265-291 (2005).
13. Corredor, R. F. F., Bizhani, M., Ashrafuzzaman, M., and Kuru, E.: An experimental investigation of turbulent water flow in concentric annulus using Particle Image

- Velocimetry technique. *Journal of Fluids Engineering*, **136**(5), 051203-051203-11 (2014).
14. François, G. S.: About Boussinesq's turbulent viscosity hypothesis: Historical remarks and a direct evaluation of its validity. *Comptes Rendus Mécanique*, Elsevier, **335**(9-10), 617-627 (2007).
 15. Menter, F. R.: Two-equation eddy-viscosity turbulence models for engineering applications. *AIAA Journal*, **32**(8), 1598-1605 (1994).
 16. Menter, F. R.: Multiscale model computation of turbulent flows. *Proceedings of the 24th Fluid Dynamics Conference*, American Institute of Aeronautics and Astronautics (1993).
 17. Keshmiri, A., Uribe, J., and Shokri, N.: Benchmarking of three different CFD codes in simulating natural, forced, and mixed convection Flows. *Numerical Heat Transfer, Part A: Applications*, **67**(12), 1324-1351 (2015).
 18. Wilcox, D.C.: Multiscale model for turbulent flows. *Proceedings of the AIAA 24th Aerospace Sciences Meeting*, **26**(11), 1311-1325 (1986).
 19. Launder, B. E., and Spalding, D. B.: The numerical computation of turbulent flows. *Computational Methods in Applied Mechanics and Engineering*, **3**, 269-289 (1974).
 20. Härtel, C., and Kleister, L.: Analysis and modelling of subgrid-scale motions in near-wall turbulence. *Journal of Fluid Mechanics*, **365**, 327-352 (1998).
 21. White, F. M.: *Viscous Fluid Flow*, McGraw-Hill Companies, New York (2005).

22. Kármán, Th.: Mechanical similitude and turbulence. Tech. Mem. NACA, No. 611 (1993).
23. Ould, -R. M., Redjem, -S. L., and Lauriat, G.: Direct numerical simulation of turbulent heat transfer in annuli: Effect of heat flux ratio. *International Journal of Heat and Fluid Flow*, **30**, 579-589 (2009).
24. Rehme, K.: Turbulence measurements in smooth concentric annuli with small radius Ratios. *Journal of Fluid Mechanics*, **76**(1), 189-206 (1975).
25. Kolmogorov, A. N.: A refinement of previous hypotheses concerning the local structure of turbulence in a viscous incompressible fluid at high Reynolds number. *Journal of Fluids Mechanics*, **13**, 82-85 (1962).
26. Pope, S.B.: *Turbulent Flows*. IOP Publishing, (2001).
27. Härtel, C., Kleiser, L., Unger, F., and Friedrich, R.: Subgrid-scale energy transfer in the near-wall region of turbulent flows. *Physics of Fluids*, **6**, 3130-3143 (1994).
28. Ptasinski, P. K., Boersma, B. J., Nieuwstadt, F. T. M., Hulsén, M. A., VandenBrule, B. H. A. A., and Hunt, J. C. R.: Turbulent channel flow near maximum drag reduction: Simulations, experiments and mechanisms. *Journal Fluid Mechanics*, **490**, 251-291 (2003).
29. Antonia, R. A., Teitel, M., Kim, J., and Browne, L. W. B.: Low-Reynolds-number effects in a fully developed turbulent channel flow. *Journal Fluid Mechanics*, **236**, 579-605 (1992).

Chapter 4 RANS Simulation of Non-Newtonian Drag Reduction Fluid in Concentric Annulus Using the Power Law Model

This chapter is based on a published conference preceeding: Xiong X., Rahman A., Zhang Y.: Characterization of time-averaged turbulence statistics for shear-thinning fluid in horizontal concentric annulus using RANS based CFD Simulation, Proceedings of ASME 35th Conference on Ocean, Offshore and Arctic Engineering, Busan, South Korea, OMAE2016-54379 (2016). I conducted all the simulations, prepared the manuscript, and made the revisions during the publication process. Dr. Aziz Rahman and Dr. Yan Zhang provide essential supports and suggestions while running the simulations and writing the paper.

4.1 Introduction

A tremendous amount of effort has been spent in the past to expose the drag reduction (DR) phenomenon of the non-Newtonian fluid first reported by Toms [1]. Conventional theory suggests that the friction pressure drop for flow in pipelines is determined by shear stress and turbulent stress, the sum of which is called the total stress. Obviously, on the one hand, as clearly stated by its definition, shear stress is proportional to the fluid viscosity and shear rate, where viscosity has a direct influence. On the other hand, invoking the law of wall for wall-bounded flow, the structure of the viscous sub-layer, closely related to the dissipation of the turbulent kinetic energy, is also heavily dependent on fluid viscosity. Encouraged by this notion, Lumley [2, 3] proposed an elongational-viscosity hypothesis to explain the mechanism of DR, which suggested that there supposed to be an elongational viscosity induced by polymer additives, promoting the extent of the viscous sub-layer in the wall-bounded flow.

However, the experimental results of Virk et al. [4,5], discussing the onset of DR and the existence of maximum DR by analyzing the time-averaged turbulence statistics, suggested that the variance of viscosity is not the only factor that induced the DR. Consequently, Gennes [6] argued that the DR was caused by the elastic instead of the viscous property of the polymers. This idea was also supported by experiments performed by McComb and Rabie [7], which showed that DR could happen even if the polymers were injected in the centre of the pipe. Conclusively, these experimental studies suggested that the elastic property of polymers should be the critical factor that reduced the production of velocity fluctuations in the turbulent flow. Further

experimental studies [8-10] reported that there was a stress void in DR flow, indicating that the total stress no longer equals to the sum of the Reynolds stress and shear stress, and instead a small amount of Reynolds stress was absorbed by the polymer additives and then existed in another stress form ‘‘elastic stress’’. These findings confirmed that the elasticity theory of Gennes is more suitable for characterizing the mechanism of DR in a polymer solution because the elongational-viscosity hypothesis fails to predict the stress void. [9].

Recently, with the rapid increase of computational power, numerical simulations have been widely employed in the investigation of turbulent DR. Orlandi [11] and den Toonder et al. [9] conducted direct numerical simulations (DNS) based on the idea that the polymer is stretched in the direction of the flow and consequently resulted in anisotropic viscous stress in this direction. Their simulations predicted the DR and qualitatively captured the experimental findings. However, these models fail to predict the onset of DR and the stress void. Later, Sureshkumar et al. [12] and Dimitropoulos et al. [13] performed a DNS combined with a more realistic polymer model, the FENE-P model, and successfully predicted the change of turbulent statistics and the onset of DR.

While DNS is the most accurate numerical approach to predict the DR caused by polymer additives, its computational cost is exceptionally high. Thus, the objective of the present study is to reduce that cost by applying the Reynolds-averaged Navier-Stokes (RANS) approach. Since only the average velocity field is directly solved, the computational expense of this approach is significantly reduced. In this study,

simulations for fully developed turbulent flow with non-Newtonian shear-thinning fluid at mass flow rates ranging from 3.92 kg/s to 5.95 kg/s and polymer concentrations varying from 0.07% V/V to 0.12% V/V were performed in the concentric annulus, using the commercial CFD code of ANSYS-CFX.

4.2 Numerical Procedures

4.2.1 Governing Equations

4.2.1.1 Reynolds-averaged Navier-Stokes Equations (RANS)

The conservation of mass and momentum equations as described detailedly in Chapter 3 were solved in this study:

$$\nabla \cdot U = 0 \quad (4-1)$$

$$\frac{\partial}{\partial x_j} (\rho U_i U_j) = -\frac{\partial P}{\partial x_i} + \frac{\partial}{\partial x_j} \left[\mu \left(\frac{\partial U_i}{\partial x_j} + \frac{\partial U_j}{\partial x_i} \right) - \rho \overline{u_i u_j} \right] \quad (4-2)$$

Because the non-Newtonian fluid is considered here instead of water, the dynamic viscosity of non-Newtonian solution in the momentum equation μ , $Pa \cdot s$, is no longer a constant but changing with the shear rate, which needs to be estimated by a non-Newtonian constative model.

4.2.1.2 Shear Stress Transportation (SST) Model

The same turbulence model [14,15] used in Chapter 3 was also employed for the current study. Instead of directly providing the ultimate form of SST model, we hereby focused on the explanation of how the model has been derived, which helps demonstrate how one of the SST model constants is changed later in the present study to achieve DR.

The SST model employs two transportation equations, one for turbulent kinetic energy k and the other for turbulent frequency ω , where k , ε and ω are related as in [17]:

$$\varepsilon = C_\mu k \omega \quad (4-3)$$

The Wilcox model [16]:

$$\frac{\partial}{\partial x_j} (\rho U_j k) = \frac{\partial}{\partial x_j} \left[\left(\mu + \frac{\mu_t}{\sigma_k} \right) \frac{\partial k}{\partial x_j} \right] + P_k - \beta' k \omega \quad (4-4)$$

$$\frac{\partial}{\partial x_j} (\rho U_j \omega) = \frac{\partial}{\partial x_j} \left[\left(\mu + \frac{\mu_t}{\sigma_{\omega 1}} \right) \frac{\partial \omega}{\partial x_j} \right] + \alpha_1 \frac{\omega}{k} P_k - \rho \beta_1 \omega^2 \quad (4-5)$$

Transformed k- ε model:

$$\frac{\partial}{\partial x_j} (\rho U_j k) = \frac{\partial}{\partial x_j} \left[\left(\mu + \frac{\mu_t}{\sigma_k} \right) \frac{\partial k}{\partial x_j} \right] + P_k - \beta' k \omega \quad (4-6)$$

$$\begin{aligned} \frac{\partial}{\partial x_j} (\rho U_j \omega) = \frac{\partial}{\partial x_j} \left[\left(\mu + \frac{\mu_t}{\sigma_{\omega 2}} \right) \frac{\partial \omega}{\partial x_j} \right] + \frac{2\rho}{\omega \sigma_{\omega 2}} \frac{\partial k}{\partial x_j} \frac{\partial \omega}{\partial x_j} \\ + \alpha_2 \frac{\omega}{k} P_k - \rho \beta_2 \omega^2 \end{aligned} \quad (4-7)$$

In CFX, the Wilcox model is multiplied by function F_1 and the transformed k- ε model

by $1-F_1$ in order to form the SST model as follows:

$$\frac{\partial}{\partial x_j} (\rho U_j k) = \frac{\partial}{\partial x_j} \left[\left(\mu + \frac{\mu_t}{\sigma_k} \right) \frac{\partial k}{\partial x_j} \right] + P_k - \beta' k \omega \quad (4-8)$$

$$\begin{aligned} \frac{\partial}{\partial x_j} (\rho U_j \omega) = \frac{\partial}{\partial x_j} \left[\left(\mu + \frac{\mu_t}{\sigma_{\omega 2}} \right) \frac{\partial \omega}{\partial x_j} \right] + (1 - F_1) \frac{2\rho}{\omega \sigma_{\omega 2}} \frac{\partial k}{\partial x_j} \frac{\partial \omega}{\partial x_j} \\ + \alpha_3 \frac{\omega}{k} P_k - \rho \beta_3 \omega^2 \end{aligned} \quad (4-9)$$

The detailed expressions of the unknowns in the SST model, for instance, the blending functions, have been presented in Chapter 3. The default model coefficients are listed in Table 4-1. Particularly, α_3 and β_3 in Eq. 4-9 are dimensionless model constants that need to be calculated using the blending functions.

4.2.1.3 Near-wall Treatment

The same Near-wall treatment, as described in Chapter 3, has been used in this chapter. The detail of the wall function can also be found in the previous chapter.

Table 4- 1 Default Model Coefficients

α_1	β_1	$\sigma_{\omega 1}$	σ_{k1}	c_1	a_1
0.556	0.075	2.0	1.176	0.31	0.31
α_2	β_2	$\sigma_{\omega 2}$	σ_{k2}	β'	C_μ
0.44	0.8282	1.168	1.0	0.09	0.09

4.2.2 Power Law Model

As mentioned before, unlike the water case, where viscosity keeps constant, the viscosity of a non-Newtonian fluid experienced remarkable changes with the change of shear strain. Thus, the viscosity of the non-Newtonian flow needs to be accurately modelled. The shear-thinning fluid discussed in this study and from the literature follows the power-law model as:

$$\tau = aS^b \quad (4-10)$$

where S is the average shear rate, $1/s$, a is the flow consistency index, $Pa \cdot s^b$, and b is the dimensionless flow behavior index (-). Thus, the fluid viscosity used in the momentum equation can be estimated as:

$$\mu = aS^{b-1} \quad (4-11)$$

Note that a and b listed in Table 4-2 are directly obtained from literature [18].

4.2.3 Problem Setups

Steady-state simulations were performed with the turbulence models discussed above in the fully developed flow regime. The finite volume method (FVM) solver available in ANSYS-CFX is used for the discretization of the governing equations. Mass flow rate with 5% turbulence intensity is set for the boundary condition at the inlet while static pressure for the outlet. Both walls of the annulus are set to be no-slip.

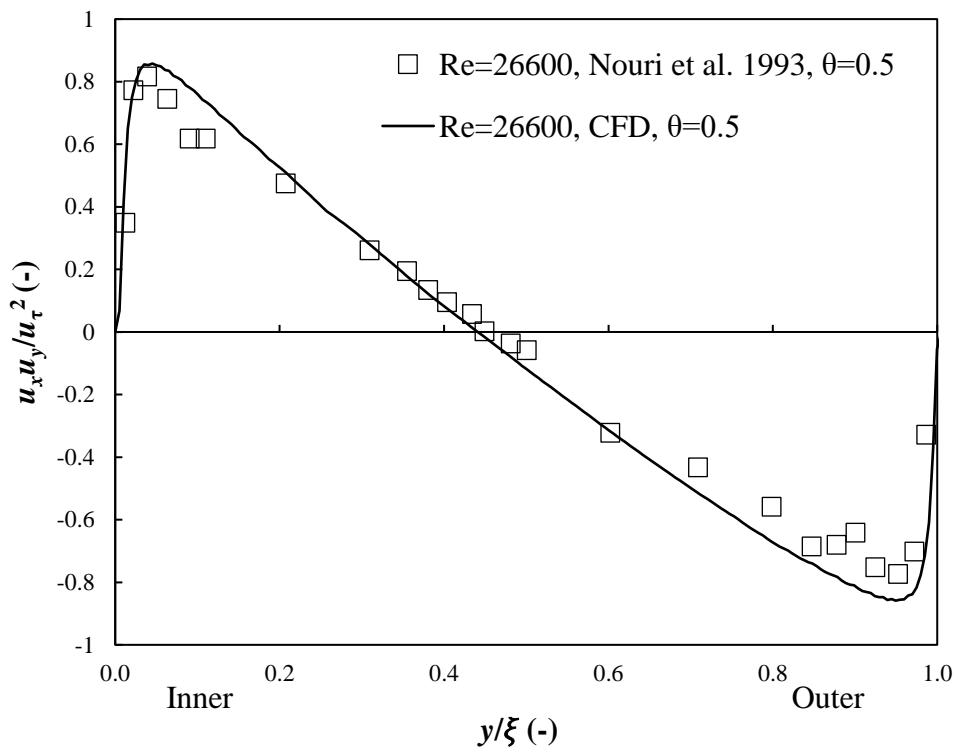


Fig. 4- 1 Reynolds Stress for Water

The same mesh in Chapter 3 is used to support the current study, whose accuracy has already been confirmed by a mesh independence test regarding mean flow velocity. In order to further test its accuracy, simulation results in this study were compared with experimental results reported by Nouri and Whitelaw [19] again, as shown in Fig. 4-1. The Reynolds stress, normalized by frictional velocity u_τ was calculated at $Re = 26600$ based on the bulk velocity and the hydraulic diameter for fully turbulent flow in an

annulus with $\theta = 0.5$. According to this figure, the presented results are in good agreement with the experimental data, which indicates that the present model is sufficient to support the following analysis.

4.3 Results and Discussions

In this study, two groups of simulations were conducted in order to investigate the influence of polymer additives on turbulence statistics, as shown in Table 4-2. In the first group, turbulent flow of non-Newtonian fluid was simulated at three different mass flow rates 3.92, 4.93, and 5.95 kg/s, with fluid viscosity modified by the power-law model. In the second group, in addition to modelling viscosity with the power-law model, one of the turbulence model constants α_1 in the SST model was also adjusted. At last, simulations of water from Chapter 3, which are not listed in Table 4-2, at the same mass flow rates are adopted here for reference purposes. All the simulation results were validated against the experimental study reported by Corredor et al. [18].

Table 4- 2 Control Factors for Different Test Cases

Test group	Polymer Concentration (V/V%)	a	b	α_1
1	0.07	0.010	0.826	
	0.10	0.019	0.776	default
	0.12	0.033	0.704	
2	0.07	0.010	0.826	0.72
	0.10	0.019	0.776	0.88
	0.12	0.033	0.704	0.84

4.3.1 Pressure Drop

Pressure drop is the first to be investigated since it is the most direct reflection of the turbulence intensity of the flow. Here the pressure drop is first compared for flows with

different polymer concentrations at the same mass flow rate and then for flows at different mass flow rates but with the same polymer concentration. A clear over-estimation of pressure drop for shear-thinning fluid can be seen in Table 4-3 and Table 4-4 when the default SST model and power-law model is used, indicating that the turbulence intensity of the flow is not decayed and no DR is achieved. Besides, it can also be noted that deviations between the simulation and experimental results keep increasing with various mass flow rate at constant polymer concentration, and in contrast, such a trend does not hold for the deviation with increasing polymer concentrations at a constant mass flow rate.

Table 4- 3 Pressure Drop by Only Power Law Model at Constant Mass Flow Rate

m=3.93 (kg/s)		Pressure Drop(Pa/m)	
Concentrations(V/V %)	Experiment	Simulation	Deviations
0.07	90.9	119.8	31.7%
0.10	88.1	144.2	63.6%
0.12	92.3	154.8	62.5%

Table 4- 4 Pressure Drop by Only Power Law with Constant Polymer Concentration

Concentration=0.07 (V/V %)		Pressure Drop(Pa/m)	
Mass flow rate (kg/s)	Experiment	Simulation	Deviations
3.92	90.9	119.7	31.7%
4.93	132.3	178.0	34.6%
5.95	171.48	248.3	44.8%

In order to improve model accuracy and better capture the experimental results, the turbulent model constant α_1 was tuned in this study. As can be seen in Eq. 4-5, by increasing α_1 , the turbulent frequency of the flow is manually increased. Since the

dissipation of turbulent kinetic energy (TKE) in the SST model is estimated by Eq. 4-3, by increasing α_1 we artificially enhanced dissipation to decay turbulence and achieve DR. The optimal values of α_1 shown in Table 4-2 for the shear-thinning fluid with different concentrations were obtained by gradually increasing α_1 (other model constants kept constant as default) until satisfactory pressure drops were obtained, and those results are illustrated in Fig. 4-2. Therefore, simulation results with optimal SST model constants are used for further investigation of the DR behavior of the non-Newtonian shear-thinning fluid.

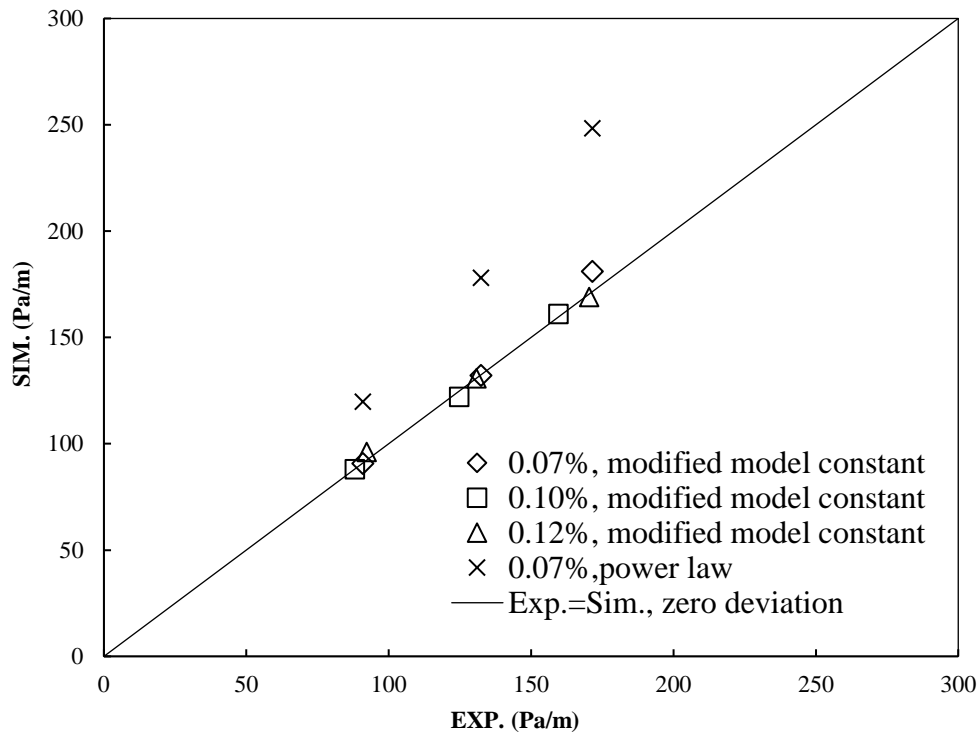


Fig. 4- 2 Pressure Drop for Different Test Cases

4.3.2 Average Axial Velocity

The average axial velocities normalized by the mean bulk velocity for flows with different concentrations at a constant mass flow rate are plotted in Fig. 4-3. Note that the velocity profiles shown here for polymer solutions were obtained by the SST model

with modified model constants. The trends of each profile are consistent with the experimental results reported by [18]. As can be seen in this figure, by adding polymers, the axial velocities in the near-wall region are significantly modified. Specifically, the slope of the velocity profile in the near-wall region increases significantly when the polymer is added, resulting in larger velocities in the core region of the annulus. Additionally, the velocity slope near-wall increase with the increase in the polymer concentration.

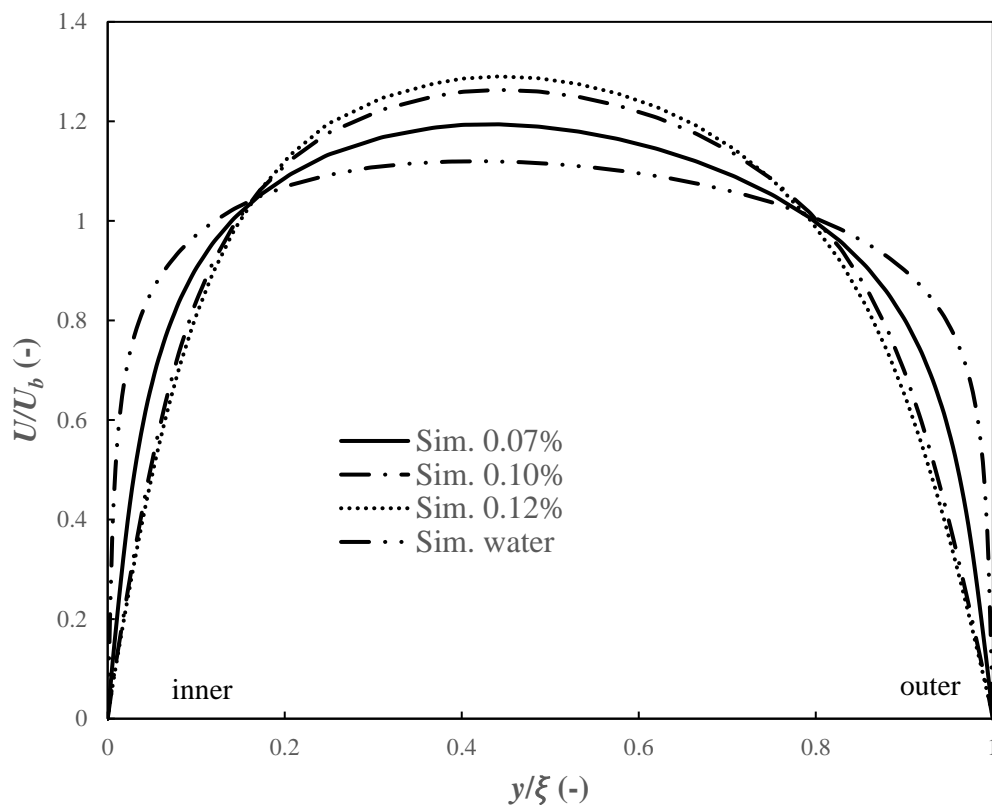


Fig. 4- 3 Axial Velocity for Different Solutions at $m=3.92$ kg/s with Modified Model Constants

4.3.3 Reynolds Stress

As mentioned by [6], the viscous property of the polymer fluid is not the primary reason for DR. Contrarily, it should be the elastic property that leads to the conversion

from the Reynolds stress to the elastic stress [9]. However, since the non-elastic power-law model is used here to characterize the polymer solution, the elastic stress term cannot be solved directly in the current simulation, which is the reason why the DR phenomenon cannot be predicted by the SST model with default model constants. Alternatively, as explained previously, in this study, the elastic effect experienced by the shear-thinning fluid is taken into consideration by manually tuning α_1 in the SST model.

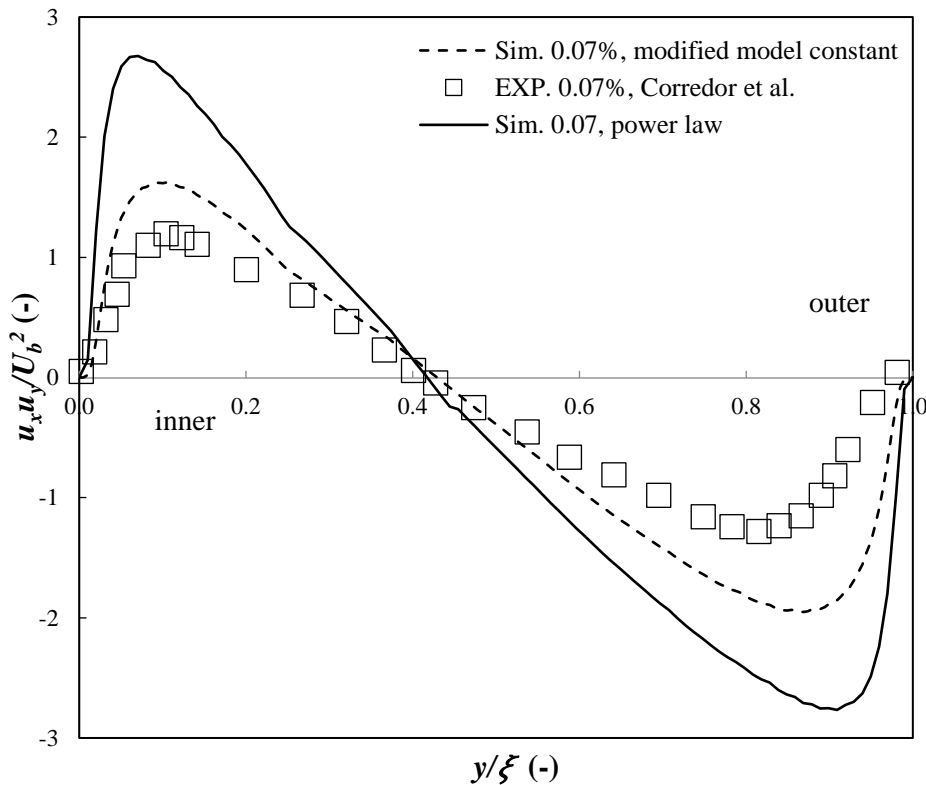


Fig. 4- 4 Reynolds Stresses for 0.07% Fluid at $m=3.92$ kg/s

Therefore, Reynolds stresses normalized by average bulk velocity U_b from experimental study and predicted by simulations with and without modified model constants are compared in Fig 4-4. As clearly shown in this figure, Reynolds stress is severely overestimated by simulations with default model constants. This figure demonstrates that the overestimation of Reynolds stress should be blamed for the

discrepancies existing in pressure drops between simulation and experimental results. In reality, a remarkable amount of Reynolds stress is absorbed and converted to elastic-related stress of the polymer solution, resulting in decreases in pressure drops. Our study shows that by properly adjusting the model constant, this decrease in Reynolds stress can be successfully captured.

Reynolds stresses for different polymer concentrations are further compared in Fig. 4-5. According to this figure, all flows with polymers additives experience much less Reynolds stresses compared with water. Besides, Reynolds stress decreases with the increase in polymer concentration, indicating that the ability of a polymer solution to transfer its Reynolds stress to the elastic stress is highly dependent on the polymer concentration within the range of concentration tested in this study. In the near-wall region, Reynolds stress of polymer solutions is remarkably decreased compared with that of water, with slope decreasing obviously. This trend is also consistent with the change of axial velocity profiles found in Fig. 4-3. Since less Reynolds stress is experienced by the fluid, axial velocity tends to increase more rapidly with regard to the radial distance.

As labeled with a row in this figure, another interesting finding for the Reynolds stress profile is that by increasing the polymer concentration, Reynolds stress seems to shift from the near-wall region to the outer wall region. Reynolds stress for water rises sharply in a very narrow zone near the wall and rapidly reaches its peak value. However, the increase of Reynolds stresses for polymer solutions occurs in the broader region and seems to be smoother. According to the universal law of the wall, a viscous sub-layer

exists in the wall-bounded Newtonian flow, where the flow mechanics are highly dependent on the viscous property of the fluid. Our simulation results imply that this layer tends to be wider for polymer solutions due to a stronger viscous effect experienced by the polymer fluid. Besides, the thickness of this layer increases with an increase in polymer concentration.

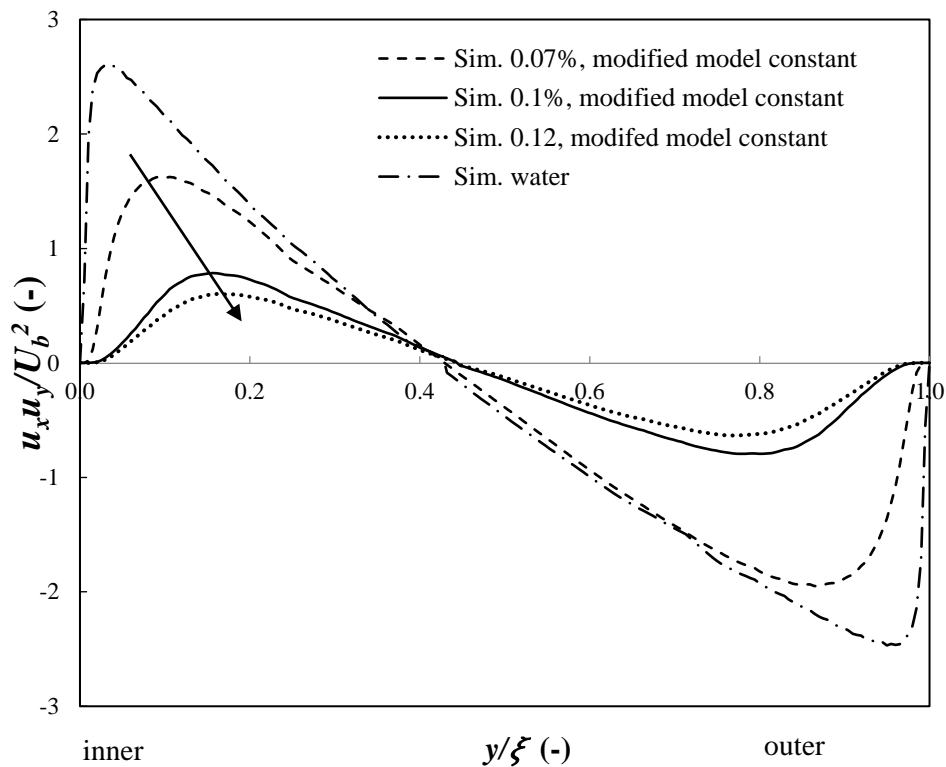


Fig. 4- 5 Reynolds Stress for at $m=3.93$ kg/s for Different Polymer Concentrations

Finally, although the polymer solution with the maximum polymer concentration of 0.12% provides the lowest Reynolds stress, as shown in Table 4-3, it produces the highest pressure drop. This phenomenon supports the existence of an optimal polymer concentration where the maximum DR occurs [5]. Before polymer concentration reaches the optimal value, the elastic effect of the polymer is minor that polymers absorb a large amount of Reynolds stress and generate a small amount of elastic stress.

As a result, the total stress decreases, leading to a decrease in pressure drop. While when the polymer concentration exceeds the optimal value, the elastic effect of the polymer becomes strong enough to influence the turbulence structure, meaning that the fluid absorbs a large portion of Reynolds stress though, it produces even a larger amount of elastic stress. Thus, as a combined effect, the total shear stress increases, increasing the pressure drop. Similar conclusions have also been drawn by Ptasinski et al. [20]

4.3.4 Correlation between α_1 and Polymer Concentration

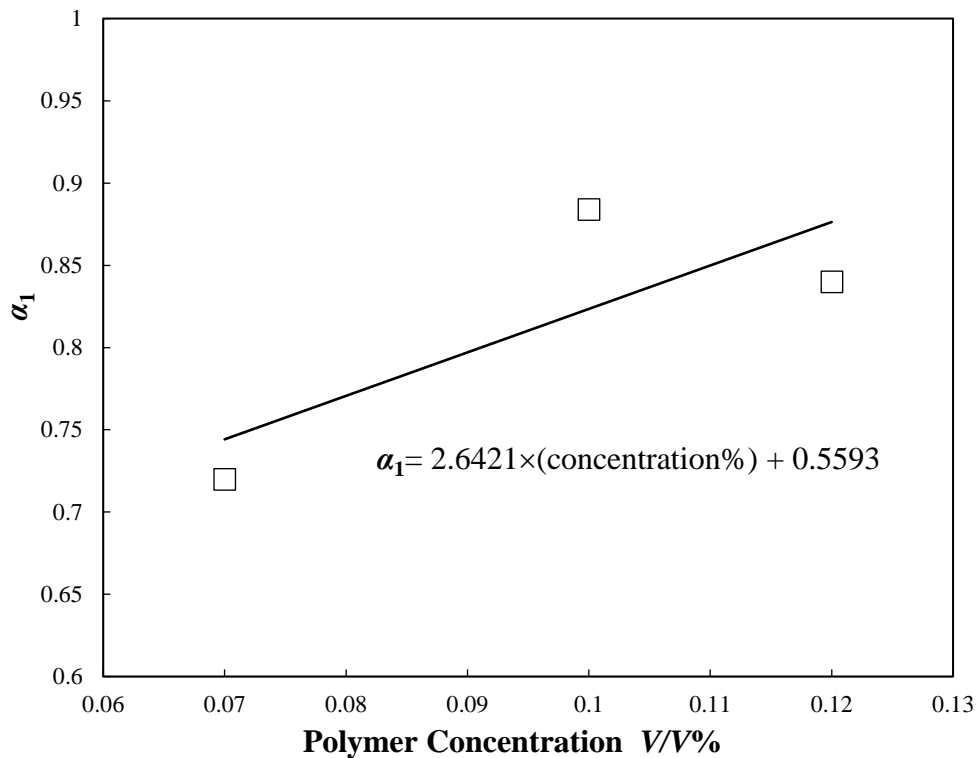


Fig. 4- 6 Relation between α_1 and Polymer Concentration

In this study, a correlation between the turbulent model constant α_1 in the SST model and the concentration of the polymer solution tested in this study is developed. While limited samples are used to configure the fitting curve in Fig. 4-6, its accuracy can be significantly increased with more case studies conducted. Ideally, when applying the same polymer solution for future works, the present turbulent model can be used to

predict the pressure drop at certain polymer concentration as long as this correlation is pre-determined with satisfactory accuracy.

4.4 Conclusions

A RANS based shear stress transportation (SST) model was employed in this chapter to validate experimental results from recent literature, which investigated the fully developed turbulent flow for a non-Newtonian shear-thinning fluid in a horizontal concentric annulus (inner to outer radius $\theta=0.4$). The concentrations of the polymers in the polymer solution varied from 0.07% V/V to 0.12% V/V, and three mass flow rates from 3.92 kg/s to 5.95 kg/s were analyzed, with the viscous property of the polymer solution characterized by the non-elastic power-law model, the same one used by the experimental study.

Simulations performed with the commercial code of ANSYS-CFX indicate that the SST model with default model constants is not able to characterize the DR nature of the shear-thinning fluid in the turbulent flow. It instead overestimated its turbulence statistics in the near-wall region where $y^+ < 60$ compared with experimental results. As an effort to improve simulation results, one of the model constants, α_1 , in the SST model was tuned in this study to enhance the dissipation of turbulent kinetic energy manually and generate DR, leading to satisfactory predictions of pressure drop for the tested shear-thinning fluid.

While the present study provides a simple approach to predict turbulent statistics for non-Newtonian DR flow in the concentric annulus, its application is limited since the current model lacks the molecular representation of the polymer that is most relevant

to the DR feature of the polymer solution. Thus, to use a more reliable model that is capable of characterizing the elastic feature of the non-Newtonian fluid will be more beneficial and will be the target for the rest of the thesis.

4.5 References

1. Toms, B. A.: Some observations on the flow of linear polymer solutions through straight tubes at large Reynolds numbers. Proceedings of the 1st International Congress on Rheology, 135-141 (1949).
2. Lumley, J.L.: Drag reduction by additives. Annual Review of Fluid Mechanics **1**(1), 367-384 (1969).
3. Lumley, J.L.: Drag reduction in turbulent flow by polymer additives. Journal of Polymer Science: Macromolecular Reviews **7**, 263-290 (1973).
4. Virk, P., Mickley, H., and Smith, K.: The ultimate asymptote and mean flow Structure in Toms' phenomenon. Journal of Applied Mechanics, **37**, 480-493 (1979).
5. Virk, P. S.: Drag reduction fundamentals. AIChE Journal, **21**, 626-656 (1975).
6. Gennes, P. G.D. Introduction to polymer dynamics, Cambridge University Press, UK (1990).
7. McComb, W. D., and Rabie, L. H.: Development of local turbulent drag reduction due to nonuniform polymer concentration. Physics of Fluids, **22**, 183-186 (1979).
8. Gyr, A. and Tsinober, A.: On the rheological nature of drag reduction phenomena. Journal Non-Newtonian Fluid Mechanics, **73**, 153-162 (1997).

9. den Toonder, J. M. J., Hulsen, M. A., Kuiken, G. D. C., and Nieuwstadt, F. T. M.: Drag reduction by polymer additives in a turbulent pipe flow: Numerical and laboratory experiment. *Journal Fluid Mechanics*, **337**, 193-231 (1997).
10. Warholic, M. D., Massah, H., and Hanratiy, T. J.: Influence of drag-reducing polymers on turbulence: Effects of reynolds number, centration, and mixing. *Experiments in Fluids*, **27**, 461-472 (1999).
11. Orlandi, P.: A Tentative Approach to the direct simulation of drag reduction by polymers. *Journal Non-Newtonian Fluid Mechanics*, **60**, 277-301 (1995).
12. Sureshkumar, R., Beris, A. N., and Handler, R. A.: Direct numerical simulation of the turbulent channel flow of a polymer solution. *Physics of Fluids*, **9**, 743-755 (1997).
13. Dimitropoulos, C. D., Sureshkumar, R., and Beris, A. N.: Direct Numerical simulation of viscoelastic turbulent channel flow exhibiting drag reduction: Effect of the variation of rheological parameters. *Journal Non-Newtonian Fluid Mechanics*, **79**, 433-468 (1998).
14. Menter, F. R.: Two-equation eddy-viscosity turbulence models for engineering applications. *AIAA Journal*, **32**(8), 1598-1605 (1994).
15. Menter, F. R.: Multiscale model computation of turbulent flows. *Proceedings of the 24th Fluid Dynamics Conference, American Institute of Aeronautics and Astronautics* (1993).
16. Wilcox, D.C.: Multiscale model for turbulent flows. *Proceedings of the AIAA 24th Aerospace Sciences Meeting*, **26**(11), 1311-1325 (1986).

17. Keshmiri, A., Uribe, J., and Shokri, N.: Benchmarking of three different CFD codes in simulating natural, forced, and mixed convection Flows. *Numerical Heat Transfer, Part A: Applications*, **67**(12), 1324-1351 (2015).
18. Corredor, R. F. F., Bizhani, M., Ashrafuzzaman, M., and Kuru, E.: An experimental investigation of turbulent water flow in concentric annulus using Particle Image Velocimetry technique. *Journal of Fluids Engineering*, **136**(5), 051203-051203-11 (2014).
19. Nouri, J., Umur, H., Whitelaw, J.: Flow of Newtonian and non-Newtonian fluids in concentric and eccentric annuli. *Journal of Fluid Mechanics* **253**, 617-641 (1993).
20. Ptasinski, P. K., Boersma, B. J., Nieuwstadt, F. T. M., Hulsen, M. A., VandenBrule, B. H. A. A., and Hunt, J. C. R.: Turbulent channel flow near maximum drag reduction: Simulations, experiments and mechanisms. *Journal of Fluid Mechanics*, **490**, 251-291 (2003).

Chapter 5 Estimation of the Drag Reduction for Fully Developed Turbulent Flow in Cylindrical Geometries Using RANS Modelling with the FENE-P Model

5.1 Introduction

Since first reported by Toms [1], the drag reduction (DR) phenomenon in a turbulent flow, induced by adding an appropriate amount of high molecular weight, long-chain polymers, has attracted many researchers' attention due to its widespread applications to energy loss prevention, naval structure design, and long-distance fluid transport [2-5].

The experimental study was the primary tool for researchers to shed lights on how polymers can achieve DR. Two of the most important findings from a vast number of experimental studies are those of Virk et al. [6,7], showing the existences of the onset and upper limit of DR, suggesting that DR is not solely caused by viscous effect [8]. Their observations imply that a numerical model that only focus on properly characterizing the viscous features of the polymer solutions is not sufficient to recast the entire mechanism relevant to DR dynamics, even if the DR can be numerically achieved [9,10]. Such models fail to produce the stress deficit in turbulent DR flow that has been widely reported by experimental studies [10-12]

Sureshkumar et al. [13] were the first to utilize a proper viscoelastic constitutive model to conduct a direct numerical study (DNS). Compared with experimental results, their study demonstrated that the FENE-P model, which has become the most widely used model since and was also adopted in the present study, is efficient to characterize

the DR dynamics. Since detailed measurements of turbulence variables in an experiment for turbulent flow are difficult, especially for polymer solutions, where rheological properties of the fluid are extremely complex, DNS became the preferred tool for analyzing DR behaviors and was widely used in the following studies [14-19]. Despite advancing the understanding of polymer-induced DR, the recent expansion of DNS studies supplies an abundance of databases for researchers to develop more cost-effective numerical approaches, for instance, the Reynolds-averaged-Navier-Stokes (RANS) approach, which is well-known for its high capability and low computational expense.

Consequently, many studies have been conducted in the past decade to incorporate the FENE-P model into the RANS approach [20-22]. The outstanding work completed by Iaccarino et al. [23] and Masoudian et al. [24,25] developed RANS approaches based on the $k-\varepsilon-\overline{v^2}-f$ model, with closures derived by analysis of DNS results from channel flow. The additions of the velocity variance term $\overline{v^2}$ and the turbulence redistribution function f overcomes the defect of using the isotropic turbulence assumption of the standard $k-\varepsilon$ model, leading to proper characterization of the anisotropic turbulence near the solid wall, which plays a crucial role in DR behavior in wall bounded flows, and making their models capable of predicting the entire ranger of turbulent DR in channel flow.

However, to the best of the authors' knowledge, no numerical study has been conducted in the cylindrical geometry so far for DR in turbulent flows using a viscoelastic model, despite its wide engineering applications to heat exchangers,

nuclear reactors, and drilling operation systems in oil and gas industry [26-28]. On the other hand, although Iaccarino [23] et al. and Masoudian et al. [25] successfully built models for channel flow, they only validated the results against DNS data, lacking direct validations against experimental studies. It is relatively challenging to do so since the viscosity of the tested solution was measured by most of the experimental studies in the past, while the elasticity, which is essential to using the viscoelastic model for numerical study, was barely discussed [29].

As a result, the objective of this study is to propose a RANS approach that is reliable to predict turbulent DR in the cylindrical geometry and to find a proper way to relate the experimentally measured fluid properties to elastic parameters that can be used in viscoelastic models, so that direct comparison between numerical and experimental studies becomes achievable. Polymer solutions in this study are characterized by the FENE-P model and the $k-\varepsilon-\overline{v^2}-f$ model is used to model the turbulence. Simulations were realized by the commercial solver available in ANSYS-FLUENT, with additional models coded in using the User-Defined-Function (UDF). Simulation results were validated against experimental results from literature.

5.2 Numerical Models

5.2.1 Governing Equations

The steady-state Reynolds-averaged transport equations of the turbulent flow for incompressible DR fluid in the cylindrical geometry can be expressed as follows:

Continuity:

$$\nabla \cdot \mathbf{U} = 0 \tag{5-1}$$

Momentum:

$$\rho \nabla \mathbf{U} \cdot \mathbf{U} = -\nabla P + \nabla \cdot \bar{\boldsymbol{\tau}} \quad (5-2)$$

and the shear stress tensor can be expressed as:

$$\bar{\boldsymbol{\tau}} = -\rho \overline{\mathbf{u}\mathbf{u}} + \bar{\boldsymbol{\tau}}_s + \bar{\boldsymbol{\tau}}_p \quad (5-3)$$

where \mathbf{U} is the velocity, m/s , ρ is the fluid density, kg/m^3 , P is the pressure, Pa , and $\rho \overline{\mathbf{u}\mathbf{u}}$ is the Reynolds stress caused by turbulence, Pa , which will be solved by the turbulence model. The last two terms on the right-hand side of Eq. (5-3) are the shear stresses in the polymer solution that are contributed by its Newtonian solvent $\bar{\boldsymbol{\tau}}_s$, Pa and the polymer solute $\bar{\boldsymbol{\tau}}_p$, Pa , respectively, which can be solved by proper constitutive models. In particular, $\bar{\boldsymbol{\tau}}_s$ is estimated by the Boussinesq's approximation $\bar{\boldsymbol{\tau}}_s = \mu_s [\nabla \mathbf{U} + (\nabla \mathbf{U})^T]$, which is the well-known constitutive model for Newtonian fluid, where μ_s is the dynamic viscosity of the water solvent, $Pa \cdot s$; whereas the constitutive model required for the computation of $\bar{\boldsymbol{\tau}}_p$ needs further investigation.

5.2.2 Constitutive model: FENE-P model:

One of the viscoelastic constitutive models, the finite extensible non-linear elastic model with Peterlin closure (FENE-P), is used to solve the shear stress contributed by polymers, where polymers are believed to follow the elastic dumbbell model that experience a "coil-stretch" process, absorbing and releasing the turbulent kinetic energy in a turbulent flow, leading to DR. In this model, the polymer stress $\bar{\boldsymbol{\tau}}_p$ is solved explicitly by the following expression:

$$\bar{\tau}_{i,j,p} = -\frac{\mu_p}{\lambda} (\delta_{ij} - C_{ij} F^p - \overline{c_{ij} f^p}) \quad (5-4)$$

where F^p is the dimensionless Peterlin function defined by:

$$F^p = F^p(C_{nn}) = \frac{L^2}{L^2 - C_{nn}} \quad \text{and} \quad F^p(L) = 1 \quad (5-5)$$

and $\mu_p = \mu_0(1 - \beta)$ is the polymeric viscosity, $Pa \cdot s$, $\mu_0 = \mu_s + \mu_p$ is the dynamic viscosity of solution at zero shear stress, $Pa \cdot s$, β is the ratio between μ_p and μ_0 , (-), λ is the polymer relaxation time, s, and L is the dimensionless maximum extension length of the polymer chains, (-). Note that Eq. (5-4) is expressed in its Reynolds-averaged form in which C_{ij} and c_{ij} are the time-averaged and time-fluctuating components of the dimensionless polymer conformation, (-), respectively. Particularly, their traces C_{nn} and c_{nn} appearing in Eq. (5-4) represent the elongation of the polymer chains.

Both terms on the right-hand side of Eq. (5-4) have been evaluated [21,23], and conclusions have been drawn that $C_{ij}F^p$ is nearly 20 times larger than $\overline{c_{ij}f^p}$. Thus, $\overline{\hat{\tau}}_p$ is accurate enough to be modelled by $-\frac{\mu_p}{\lambda}(\delta_{ij} - C_{ij}F^p)$, the leading term in its Taylor expansion. Obviously, by using this approximation, the time-averaged component of the conformation tensor C_{ij} is the only variable left unknown in Eq. (5-4) in order to calculate the polymer stress.

Within the FENE-P framework, C_{ij} obeys a hyperbolic differential equation with its form in the RANS approach expressed as:

$$\nabla \cdot (\mathbf{U}C_{ij}) + \overline{\nabla \cdot (\mathbf{u}c_{ij})} = \underbrace{C_{kj} \cdot \nabla \mathbf{U}_{ik} + [\nabla \mathbf{U}_{jk}]^T \cdot C_{ik}}_{M_{ij}} + \underbrace{c_{kj} \cdot \nabla \mathbf{u}_{ik} + [\nabla \mathbf{u}_{jk}]^T \cdot c_{ik}}_{NLK_{ij}} + \frac{1}{\lambda}(\delta_{ij} - C_{ij}F^p) \quad (5-6)$$

Starting from the left-hand side of Eq. (5-6), the first two terms represent the advection transport of the polymer conformation by the average and instantaneous flow fields; the third and fourth terms, M_{ij} and NLT_{ij} , correspond to the stretching and releasing of

polymer chains due to the mean and fluctuating velocities, respectively; and the last term on the right-hand side is the restoration term that limits the elongation of the polymer chains.

Note that the first term on the left-hand side of this equation is negligible [30,31]. Additionally, in a fully developed streamwise-dominating flow considered in this study, only the average streamwise velocity is non-zero, and all average flow variables only change in the wall-normal direction, representing a one-dimensional shear flow. As a result, the second term on the left side of Eq. (5-6) is always zero, leaving M_{ij} and NLK_{ij} on the right-hand side of the equation the only unknowns in order to solve this equation.

Specifically, aiming at reducing the computational expense and improving the stability of the numerical method for solving the tensor evolution equation, Iaccarino et al. [23]'s idea has been followed. It is based on the assumption that the effect of polymers in the turbulent flow can be solely characterized by their stretching effect, responsible for the energy storage property of polymers, which is of crucial importance in a RANS based simulation, whereas the orientation of polymer chains represented by the shear components of C_{ij} , which only alter the energy transfer, can be neglected. Such simplification considerably reduces the computational expense, since only the transportation equation of the trace of the conformation tensor C_{mn} needs to be solved. Besides, M_{ij} is modelled by its solution of the 1-D laminar shear flow, instead of being directly solved in this study.

In detail, assuming laminar flow and neglecting all the fluctuating terms, the evolution equation of the conformation tensor reads:

$$\overbrace{C_{ki} \cdot \nabla \mathbf{U}_{jk} + [\nabla \mathbf{U}_{ik}]^T \cdot C_{jk}}^{M_{ij}} + \frac{1}{\lambda} (\delta_{ij} - C_{ij} F^p) = 0 \quad (5-7)$$

where M_{ij} in the cylindrical geometry can be expressed as:

$$M_{ij} = \begin{bmatrix} C_{zz} & C_{\vartheta z} & C_{rz} \\ C_{z\vartheta} & C_{\vartheta\vartheta} & C_{r\vartheta} \\ C_{zr} & C_{\vartheta r} & C_{rr} \end{bmatrix} \cdot \begin{bmatrix} \frac{\partial U_z}{\partial z} & \frac{\partial U_\vartheta}{\partial z} & \frac{\partial U_r}{\partial z} \\ \frac{1}{r} \frac{\partial U_z}{\partial \vartheta} & \frac{1}{r} \frac{\partial U_\vartheta}{\partial \vartheta} + \frac{U_r}{r} & \frac{1}{r} \frac{\partial U_r}{\partial \vartheta} - \frac{U_\vartheta}{r} \\ \frac{\partial U_z}{\partial r} & \frac{\partial U_\vartheta}{\partial r} & \frac{\partial U_r}{\partial r} \end{bmatrix} \\ + \begin{bmatrix} \frac{\partial U_z}{\partial z} & \frac{1}{r} \frac{\partial U_z}{\partial \vartheta} & \frac{\partial U_z}{\partial r} \\ \frac{\partial U_\vartheta}{\partial z} & \frac{1}{r} \frac{\partial U_\vartheta}{\partial \vartheta} + \frac{U_r}{r} & \frac{\partial U_\vartheta}{\partial r} \\ \frac{\partial U_r}{\partial z} & \frac{1}{r} \frac{\partial U_r}{\partial \vartheta} - \frac{U_\vartheta}{r} & \frac{\partial U_r}{\partial r} \end{bmatrix} \cdot \begin{bmatrix} C_{zz} & C_{\vartheta z} & C_{rz} \\ C_{z\vartheta} & C_{\vartheta\vartheta} & C_{r\vartheta} \\ C_{zr} & C_{\vartheta r} & C_{rr} \end{bmatrix} \quad (5-8)$$

Invoke the assumption that the main flow happens in the streamwise direction, $U_\vartheta = U_r = 0$ and $U_z = U_z(r)$, M_{ij} can be simplified as:

$$M_{ij} = \begin{bmatrix} C_{rz} \frac{\partial U_z}{\partial r} & 0 & 0 \\ C_{r\vartheta} \frac{\partial U_z}{\partial r} & 0 & 0 \\ C_{rr} \frac{\partial U_z}{\partial r} & 0 & 0 \end{bmatrix} + \begin{bmatrix} C_{rz} \frac{\partial U_z}{\partial r} & C_{r\vartheta} \frac{\partial U_z}{\partial r} & C_{rr} \frac{\partial U_z}{\partial r} \\ 0 & 0 & 0 \\ 0 & 0 & 0 \end{bmatrix} \quad (5-9)$$

Consequently, the ultimate form of the evolution equation can be expressed as:

$$\begin{bmatrix} 2C_{rz} \frac{\partial U_z}{\partial r} & C_{r\vartheta} \frac{\partial U_z}{\partial r} & C_{rr} \frac{\partial U_z}{\partial r} \\ C_{r\vartheta} \frac{\partial U_z}{\partial r} & 0 & 0 \\ C_{rr} \frac{\partial U_z}{\partial r} & 0 & 0 \end{bmatrix} = \\ - \begin{bmatrix} \frac{1}{\lambda} (1 - C_{zz} F^p) & \frac{1}{\lambda} (-C_{\vartheta z} F^p) & \frac{1}{\lambda} (-C_{rz} F^p) \\ \frac{1}{\lambda} (-C_{\vartheta z} F^p) & \frac{1}{\lambda} (1 - C_{\vartheta\vartheta} F^p) & \frac{1}{\lambda} (-C_{r\vartheta} F^p) \\ \frac{1}{\lambda} (-C_{zr} F^p) & \frac{1}{\lambda} (-C_{\vartheta r} F^p) & \frac{1}{\lambda} (1 - C_{rr} F^p) \end{bmatrix} \quad (5-10)$$

Once each component of the conformation tensor is sorted out by solving these algebraic equations, M_{ij} is available. Therefore, NLK_{ij} becomes the only term in the evolution equation that remains unknown.

Due to the lack of DNS results, no model can be proposed for this term in the cylindrical geometry. However, since the test flow in this study is one dimensional, identical to its channel flow counterpart, it is rational to use the model for NLK_{ij} developed from DNS analysis in channel flow to estimate this term [25]:

$$NLK_{ij} = 0.04\sqrt{L^2}M_{ij}\frac{\mu_p}{\mu_0} \quad (5-11)$$

Thus, with M_{ij} and NLK_{ij} determined, the evolution equation of conformation tensor in the turbulent flow Eq. (5-5) can be closed to solve for the conformation tensor, which will then be used to calculate the polymer stress by Eq. (5-4).

5.2.3 Turbulence model: modified $k-\varepsilon-\overline{v^2}$ - f model

As discussed previously, the $k-\varepsilon-\overline{v^2}$ - f model developed by Durbin and Lien [6,7] has become the base model to incorporate with the FENE-P model to simulate turbulent DR flow, justified by the fact that it predicts accurate wall-induced turbulence anisotropy at the near-wall region, where DR mainly occurs. This is achieved by introducing two additional transportation equations to the standard $k-\varepsilon$ model, one for the wall-normal fluctuating velocity variance $\overline{v^2}$, m^2/s^2 , and the other for the turbulence redistribution function, f , (-). However, the standard $k-\varepsilon-\overline{v^2}$ - f model cannot be directly used to model DR, since it is developed and validated for Newtonian fluid only. Consequently, closures proposed by Masoudian et al. [25] are also adopted in the

present study to account for the interactions between polymers and turbulence. The governing equations of the modified k - ε - $\overline{v^2}$ - f model are shown as follows:

$$\rho \nabla \cdot \mathbf{U} k = \rho P_k - \rho \varepsilon + \left(\mu_s + \frac{\mu_t}{\sigma_k} \right) \nabla^2 \cdot k - \frac{\mu_p}{2\lambda} F^p \cdot NLK_{nn} \quad (5-12)$$

$$\rho \nabla \cdot \mathbf{U} \varepsilon = \left(\frac{\rho P_k C_{\varepsilon 1} - \rho C_{\varepsilon 2} \varepsilon}{T_t} \right) + \left(\mu_s + \frac{\mu_t}{\sigma_\varepsilon} \right) \nabla^2 \cdot \varepsilon - \frac{C_{\varepsilon 1} \mu_p}{2\lambda T_t} F^p \cdot NLK_{nn} \quad (5-13)$$

$$\rho \nabla \cdot \mathbf{U} \overline{v^2} = \rho k f + \left(\mu_s + \frac{\mu_t}{\sigma_k} \right) \nabla^2 \cdot \overline{v^2} - 6 \frac{\rho \varepsilon}{k} \overline{v^2} - 0.002 \rho L [f(C_{nn})]^2 k f \quad (5-14)$$

$$\rho f - \rho L_t^2 \nabla^2 \cdot f = \frac{\rho}{T_t} \left[\left(\frac{2}{3} (C_1 - 1) - (C_1 - 6) \frac{\overline{v^2}}{k} \right) \right] + C_2 \frac{\rho P_k}{k} \quad (5-15)$$

where k is the turbulent kinetic energy (TKE), m^2/s^2 , ε is the dissipation rate of TKE, m^2/s^3 , T_t , s , and L_t , m , are the turbulent time and length scales, respectively, and are defined as:

$$T_t = \max \left\{ \frac{k}{\varepsilon}, 6 \sqrt{\frac{v_s}{\varepsilon}} \right\} \text{ and } L_t = C_L \max \left\{ \frac{k^{3/2}}{\varepsilon}, C_\eta \sqrt{\frac{v_s^{3/2}}{\varepsilon^{1/2}}} \right\} \quad (5-16)$$

and P_k represents the production of TKE, m^2/s^3 :

$$P_k = \frac{\mu_t}{2\rho} [\nabla \mathbf{U} + (\nabla \mathbf{U})^T]^2 \quad (5-17)$$

The necessity of using the k - ε - $\overline{v^2}$ - f model to simulate the turbulence for DR fluid and the details of how the standard turbulence model is modified to characterize the interactions between polymers and turbulence can be found in [23]. All the governing equations listed here are identical to their counterparts for Newtonian fluid except for the last terms in the first three equations, ε_p , E_p , and $\varepsilon_{p,vv}$, m^2/s^3 , representing the closures proposed by [25] for each turbulence variables. Once all the turbulence variables are determined by solving the turbulence model, the eddy viscosity can be calculated by the following expression:

$$\mu_t = \rho C_\mu \overline{v^2} T_t \quad (5-18)$$

Eventually, the present model becomes available to predict DR in turbulent flows with all the standard model constants from Durbin [32] listed in Table 5-1.

Table 5- 1 Coefficients of Turbulence model

$C_{\epsilon 1}$	$C_{\epsilon 2}$	C_{μ}	σ_k	σ_{ϵ}	C_1	C_2	C_L	C_{η}
$C_{\epsilon 1} = 1.4 \times (1 + 0.05 \sqrt{k/\nu^2})$	1.9	0.19	1.0	1.3	1.4	0.3	0.23	70.0

5.2.4 Numerical Method

Steady-state simulations were conducted in the flow domain by using the commercial code of ANSYS-FLUENT, with the viscoelastic model for the DR solution and additional closures required in this study coded in by utilizing the User Defined Function (UDF). As seen in Fig. 5-2, 128 computational cells were allocated in the wall-normal direction for both pipe and annular geometry. Note that the pipe geometry can be considered as a special case for annulus with a zero radius for the inner wall. Starting from the solid wall, the thickness of each cell increased by a constant factor of 1.08912, the same ratio used by Zheng et al. [33], to assure the mesh accuracy. Governing equations of interest were discretized by using a finite volume (FV) based method with numerical variables at the face centre of each numerical cell, estimated by the second-order upwind scheme. The Semi-implicit method for pressure linked equations (SIMPLE) algorithm was used to solve the coupling between velocity and pressure, and all the transportation equations were solved in a segregated manner: those of velocity and pressure first and then turbulence and polymer conformation, while flow properties were updated at the beginning and end of each iteration. Periodic boundary conditions

were applied in the axial and the spanwise direction of the flow. No-slip conditions were applied for velocity, k and $\overline{v^2}$ at the solid walls, while for ε and f , the standard boundary conditions reported in [34] were used. The Neumann boundary condition with zero flux suggested by [23,35] was applied for the polymer conformation at the wall. Finally, convergence criteria of 10^{-6} were used for all flow variables.

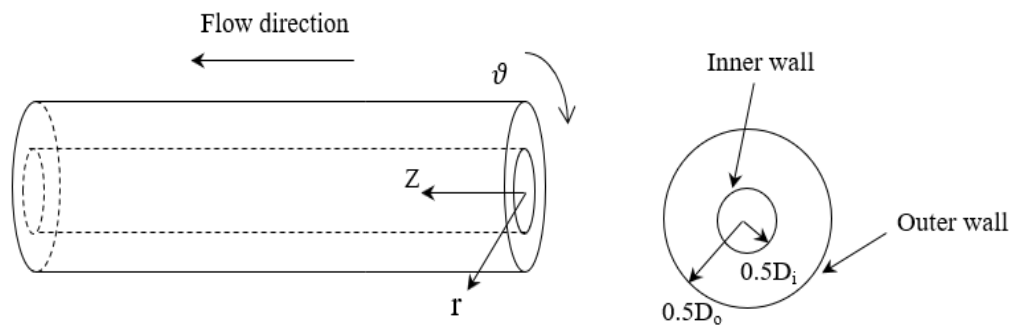


Fig. 5- 1 Scheme of the Flow Coordinate

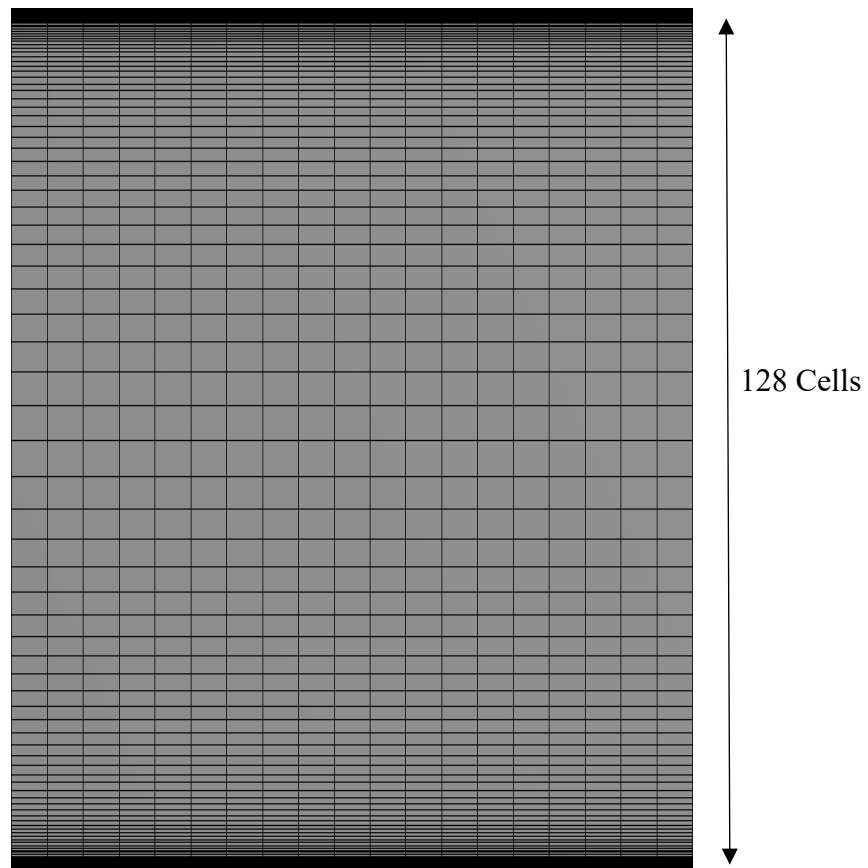


Fig. 5- 2 Mesh in the Wall-normal Direction

5.3 Model Validation and Discussions

DR predictions of the proposed model have been first validated against three independent experimental studies. The first study was carried out by Owolabi et al. [36], where the polyacrylamide was used to achieve DR. Note that the relaxation time of polymer solutions was measured and reported in their study, making it possible to use their measurements directly as inputs in the present model. However, in the second study conducted by Japper et al. [37], the relaxation time of the tested solution containing scleroglucan was not measured as the measurement of this term can be very challenging. Therefore, one of the major contributions of this chapter is that the proper way to estimate the polymer relaxation time of different polymer solution has been clarified, so that the proposed numerical model can be used to validate DR results for a wider experimental database. Specifically, this term of the polymer solutions with rigid polymers can be estimated by definition available from the literature [38]:

$$\lambda = \frac{\mu}{G} \quad (5-19)$$

where G is defined as the elasticity, Pa , and μ is the in-situ viscosity of the polymer solution, $Pa \cdot s$. Since the loss and storage modulus G' and G'' of the polymer solution were measured in their study, G can be calculated by using the following expression:

$$G = \sqrt{G'^2 + G''^2} \quad (5-20)$$

Similarly, an additional calculation of polymer relaxation time is needed in the third validation against Ptaisinski et al. [39]'s study. However, it cannot be fulfilled by using Eq. (5-19), since a non-rigid polymer, partially hydrolyzed polyacrylamide, different

from the second study, was used in the experimental study. Thus, an alternative definition suggested by Wedgewood et al. [40] was applied:

$$\lambda = \frac{\mu_p(L^2+3)}{nk_bTL^2} \quad (5-21)$$

where n is the number of polymers per unit volume (-), k_b is the Boltzmann constant, $m^2kg/(s^2K)$, and T is the absolute temperature, K . The detail of the polymer solutions used in these experimental studies are listed in Table 5-2.

Table 5- 2 Detail of Polymer Solution used for Validations

Case	Polymers	Concentration
Owolabi et al. [36]	Polyacrylamide	225 ppm
Japper et al. [37]	Scleroglucan	50 ppm 75 ppm
Ptaisinski et al. [39]	Partially Hydrolyzed Polyacrylamide	20 ppm 103 ppm 175 ppm 435 ppm
Costalonga et al. [41]	Xanthan Gum	200 ppm

The bulk velocity U_b , m/s , was the controlled variable in all simulations, which was either obtained directly from experimental studies or calculated by the general definition of the Reynolds number as

$$Re = \frac{\rho U_b D}{\mu_0} \quad (5-22)$$

where D is the diameter of the pipe. Due to additions of the new terms to the standard transport equations, the present model tends to diverge easily, unless careful numerical strategies are taken. In this study, all simulations involving DR dynamics were first run without the viscoelastic model to generate a Newtonian flow field, which was then used as the initial condition for simulations of its non-Newtonian counterpart. While solving the non-Newtonian flow, the step-length of the iterative algorithm was initially set small enough to successfully proceed the simulation, which converges well but slowly, and then gradually increased to improve the converging speed, until a fully resolved flow field could be obtained in a time-effective manner.

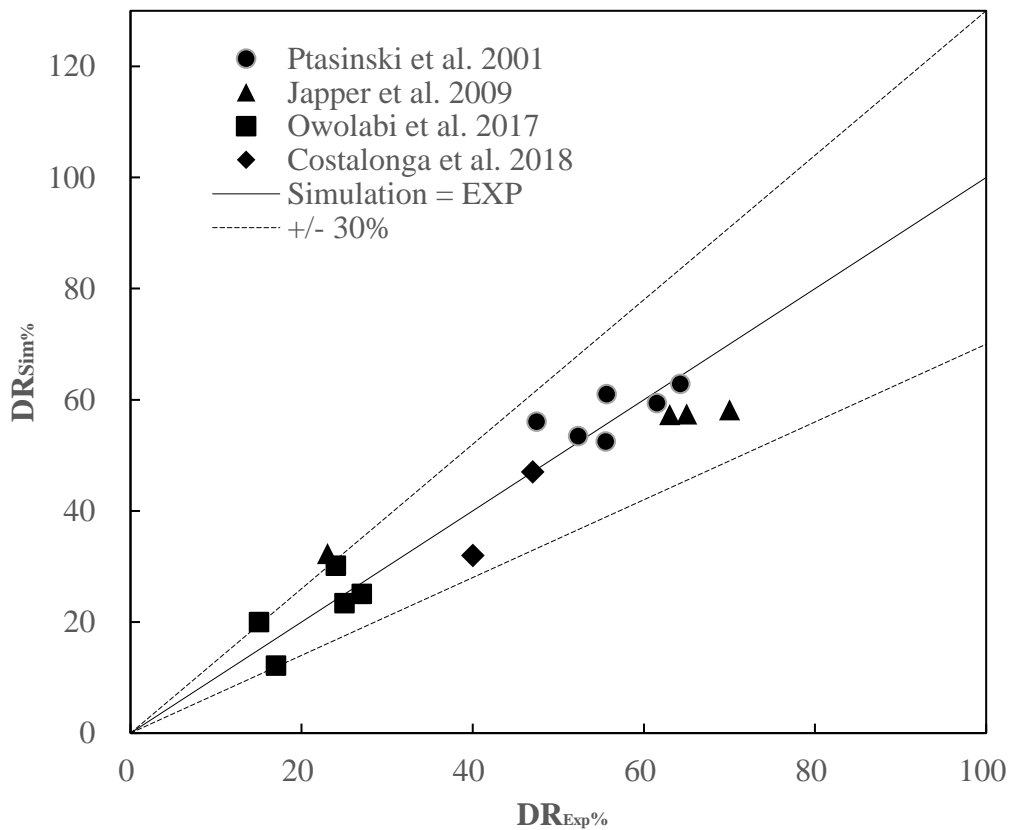


Fig. 5- 3 Comparison of DR between Numerical Prediction and Experimental Study

All predicted DR results are illustrated in Fig. 5-3 and as shown in this figure, satisfactory agreement has been found between numerical results and experimental data for all three validations, with DR defined by the following expression:

$$\%DR = 100 \times \frac{\Delta P_{Newtonian} - \Delta P_{non-Newtonian}}{\Delta P_{Newtonian}} \quad (5-23)$$

By organizing these validations, the we aim to emphasize the broad adaption of the present model to predict DR of non-Newtonian solutions containing different types of polymers (as seen in Table 5-2) with rheological parameters determined by different methods (Eq. (5-19) and Eq. (5-21)), and the figure clearly demonstrates this. Besides, Fig. 5-3 also shows that the present model is capable of predicting the whole range of DR.

Another investigation has been conducted in the present study regarding the polymer induced DR, inspired by one of the most recent experimental studies reported by Costalonga et al. [41]. In their study, the authors stated that using the hydraulic diameter $D_h = D_{out} - D_{in}$ as the length scale to define the Reynolds number in the annular as

$$Re_h = \frac{\rho U_b D_h}{\mu_0} \quad (5-24)$$

over-estimate the inertial force in a turbulent flow. As a result, to compare DR at the same Reynolds number defined by Eq. (5-24) in annular spaces and Eq. (5-22) in cylindrical pipes is inherently improper, and contrarily a modified Reynolds number proposed by Jones [42] needs to be used in the annular geometry:

$$Re_{annular} = \frac{\rho U_b D_h}{\mu} \Phi \quad (5-25)$$

where Φ is called the shape factor and expressed as:

$$\Phi = \frac{1}{(1 - D_i/D_o)} \left[1 + \left(\frac{D_i}{D_o}\right)^2 - \frac{1 - (D_i/D_o)^2}{\ln(D_o/D_i)} \right] \quad (5-26)$$

By using this expression to define Reynolds number in the annular geometry instead, they argued that DR is more pronounced in annular spaces compared with cylindrical pipes at the same Reynolds number. Their finding is confirmed in the current study, by using the proposed viscoelastic model to predict DR in a concentric annulus, with the inner to outer radius ratio of 0.4 and a shape factor of 0.405. Flow with the Reynolds number of 30000 defined by Eq. (5-22) in a pipe has only 31.7% DR, whereas flow in the annulus at the same Reynolds number defined by Eq. (5-25) has pronounced DR of 47.9%.

To better explain such finding in the viscoelastic theory, it is beneficial to invoke the Weissenberg number, which represents the ratio between the elastic force and the viscous force in the DR flow and can be defined by the diameter of the pipe D (or the hydraulic diameter of the annulus D_h):

$$We = \lambda \frac{8U_b}{D} \quad (5-27)$$

Suppose an annular geometry has a hydraulic diameter, D_h , equating to the diameter of a pipe, having the same Reynolds number in the annulus and cylindrical pipes determined by Eq. (5-25) and Eq. (5-22), respectively, guarantees the flow in the annulus to have a larger bulk velocity, since the shape factor is always less than 1 [41]. Thus, with the same polymer solution (the same relaxation time λ), a larger Weissenberg number defined by Eq. (5-27) always exists in the annular space, representing more severe elasticity of polymers, and doubtlessly leading to pronounced DR. Current study confirms the finding of Costalonga et al. though, it raises another question: whether a shape factor is needed in the definition of the Weissenberg number,

in order to reflect the dependence of the polymer elasticity on the geometry of the flow path for the viscoelastic theory, which warrants attention for future studies.

5.4 Conclusions

This chapter provides an accurate and cost-effective numerical model to estimate polymer induced turbulent drag reduction (DR) in cylindrical geometries using the RANS approach. Rheological features of the non-Newtonian fluid are characterized by the finitely extensible non-linear elastic model with Peterlin's closure (FENE-P constitutive model), and the turbulence of the flow is modelled by a modified low-Reynolds-number $k-\varepsilon-\overline{v^2}-f$ model.

Simulation results show the ability of the proposed model to predict the whole range of DR with satisfactory agreement against experimental studies, and the model is also proved capable of predicting the pronounced DR in the annulus compared to tubes, which has been experimentally observed and reported in the literature.

The current study shows how experimental studies with only viscosity related measurements can be used to validate numerical simulations needing elastic inputs for modelling non-Newtonian DR. Following proper numerical procedures suggested in this study, the present model is extremely time-efficient compared to DNS modelling, making it an ideal tool for parametric studies for engineering problems regarding turbulent DR.

5.5 References

1. Toms, B.A.: Some observations on the flow of linear polymer solutions through straight tubes at large Reynolds numbers. Proceedings of the 1st International Congress on Rheology, 135-141. North-Holland Amsterdam (1948)
2. Graham, M.D.: Drag reduction in turbulent flow of polymer solutions. *Rheology Reviews* **2**(2), 143-170 (2004).
3. Huang, X.X., Moayedi, H., Gong, S., Gao, W.: Application of metaheuristic algorithms for pressure analysis of crude oil pipeline. *Energy Sources, Part A: Recovery, Utilization, and Environmental Effects*, 1-19 (2019).
4. Nesyn, G.V., Sunagatullin, R., Shibaev, V., Malkin, A.Y.: Drag reduction in transportation of hydrocarbon liquids: From fundamentals to engineering applications. *Journal of Petroleum Science and Engineering* **161**, 715-725 (2018).
5. Eskin, D.: Modeling an effect of pipe diameter on turbulent drag reduction. *Chemical Engineering Science* **162**, 66-68 (2017).
6. Virk, P.S., Merrill, E., Mickley, H., Smith, K., Mollo-Christensen, E.: The Toms phenomenon: turbulent pipe flow of dilute polymer solutions. *Journal of Fluid Mechanics* **30**(2), 305-328 (1967).
7. Virk, P.: An elastic sublayer model for drag reduction by dilute solutions of linear macromolecules. *Journal of Fluid Mechanics* **45**(3), 417-440 (1971).
8. Gennes, P.G.D.: Introduction to polymer dynamics. Cambridge University Press, (1990)

9. Orlandi, P.: A tentative approach to the direct simulation of drag reduction by polymers. *Journal of Non-Newtonian Fluid Mechanics* **60**(2-3), 277-301 (1995).
10. Den Toonder, J., Hulsen, M., Kuiken, G., Nieuwstadt, F.: Drag reduction by polymer additives in a turbulent pipe flow: numerical and laboratory experiments. *Journal of Fluid Mechanics* **337**, 193-231 (1997).
11. Gyr, A., Tsinober, A.: On the rheological nature of drag reduction phenomena. *Journal of Non-Newtonian Fluid Mechanics* **73**(1-2), 153-162 (1997).
12. Warholic, M., Massah, H., Hanratty, T.: Influence of drag-reducing polymers on turbulence: effects of Reynolds number, concentration, and mixing. *Experiments in fluids* **27**(5), 461-472 (1999).
13. Sureshkumar, R., Beris, A.N., Handler, R.A.: Direct numerical simulation of the turbulent channel flow of a polymer solution. *Physics of Fluids* **9**(3), 743-755 (1997).
14. Dimitropoulos, C.D., Sureshkumar, R., Beris, A.N.: Direct numerical simulation of viscoelastic turbulent channel flow exhibiting drag reduction: effect of the variation of rheological parameters. *Journal of Non-Newtonian Fluid Mechanics* **79**(2-3), 433-468 (1998).
15. Dimitropoulos, C.D., Sureshkumar, R., Beris, A.N., Handler, R.A.: Budgets of Reynolds stress, kinetic energy and streamwise enstrophy in viscoelastic turbulent channel flow. *Physics of Fluids* **13**(4), 1016-1027 (2001).

16. Sibilla, S., Baron, A.: Polymer stress statistics in the near-wall turbulent flow of a drag-reducing solution. *Physics of Fluids* **14**(3), 1123-1136 (2002).
17. De Angelis, E., Casciola, C., Piva, R.: DNS of wall turbulence: dilute polymers and self-sustaining mechanisms. *Computers & fluids* **31**(4-7), 495-507 (2002).
18. Min, T., Yoo, J.Y., Choi, H., Joseph, D.D.: Drag reduction by polymer additives in a turbulent channel flow. *Journal of Fluid Mechanics* **486**, 213-238 (2003).
19. Ptasinski, P., Boersma, B., Nieuwstadt, F., Hulsen, M., Van den Brule, B., Hunt, J.: Turbulent channel flow near maximum drag reduction: simulations, experiments and mechanisms. *Journal of Fluid Mechanics* **490**, 251-291 (2003).
20. Leighton, R., Walker, D.T., Stephens, T., Garwood, G.: Reynolds stress modeling for drag-reducing viscoelastic flows. *Proceedings of ASME/JSME 4th Joint Fluids Summer Engineering Conference*, 735-744. American Society of Mechanical Engineers (2003).
21. Pinho, F., Li, C., Younis, B., Sureshkumar, R.: A low Reynolds number turbulence closure for viscoelastic fluids. *Journal of Non-Newtonian Fluid Mechanics* **154**(2), 89-108 (2008).
22. Resende, P., Kim, K., Younis, B., Sureshkumar, R., Pinho, F.: A FENE-P $k-\varepsilon$ turbulence model for low and intermediate regimes of polymer-induced drag reduction. *Journal of Non-Newtonian Fluid Mechanics* **166**(12), 639-660 (2011).

23. Iaccarino, G., Shaqfeh, E.S., Dubief, Y.: Reynolds-averaged modeling of polymer drag reduction in turbulent flows. *Journal of Non-Newtonian Fluid Mechanics* **165**(7), 376-384 (2010).
24. Masoudian, M., Kim, K., Pinho, F., Sureshkumar, R.: A viscoelastic turbulent flow model valid up to the maximum drag reduction limit. *Journal of Non-Newtonian Fluid Mechanics* **202**, 99-111 (2013).
25. Masoudian, M., Pinho, F., Kim, K., Sureshkumar, R.: A RANS model for heat transfer reduction in viscoelastic turbulent flow. *International Journal of Heat and Mass Transfer* **100**, 332-346 (2016).
26. Nouri, J., Umur, H., Whitelaw, J.: Flow of Newtonian and non-Newtonian fluids in concentric and eccentric annuli. *Journal of Fluid Mechanics* **253**, 617-641 (1993).
27. Escudier, M., Gouldson, I., Jones, D.: Flow of shear-thinning fluids in a concentric annulus. *Experiments in Fluids* **18**(4), 225-238 (1995).
28. Xiong, X., Rahman, M.A., Zhang, Y.: RANS Based Computational Fluid Dynamics Simulation of Fully Developed Turbulent Newtonian Flow in Concentric Annuli. *Journal of Fluids Engineering* **138**(9), 091202 (2016).
29. Zhang, X., Duan, X., Muzychka, Y.: Analytical upper limit of drag reduction with polymer additives in turbulent pipe flow. *Journal of Fluids Engineering* **140**(5) (2018).

30. Li, C., Gupta, V., Sureshkumar, R., Khomami, B.: Turbulent channel flow of dilute polymeric solutions: drag reduction scaling and an eddy viscosity model. *Journal of Non-Newtonian Fluid Mechanics* **139**(3), 177-189 (2006).
31. Housiadas, K.D., Beris, A.N., Handler, R.A.: Viscoelastic effects on higher order statistics and on coherent structures in turbulent channel flow. *Physics of Fluids* **17**(3), 035106 (2005).
32. Durbin, P.A.: Near-wall turbulence closure modeling without “damping functions”. *Theoretical and Computational Fluid Dynamics* **3**(1), 1-13 (1991).
33. Zheng, Z.-Y., Li, F.-C., Li, Q.: Reynolds-averaged simulation on turbulent drag-reducing flows of viscoelastic fluid based on user-defined function in FLUENT package. In: ASME 4th Joint US-European Fluids Engineering Division Summer Meeting collocated with the ASME 12th International Conference on Nanochannels, Microchannels, and Minichannels, V01AT03A010-V001AT003A010 (2014).
34. Lien, F., Durbin, P.: Non-linear $k-v^2$ modelling with application to high-lift. *Proceedings of 1996 Summer Programme*, 5-22 (1996).
35. Dubief, Y., White, C.M., Terrapon, V.E., Shaqfeh, E.S., Moin, P., Lele, S.K.: On the coherent drag-reducing and turbulence-enhancing behavior of polymers in wall flows. *Journal of Fluid Mechanics* **514**, 271-280 (2004).
36. Owolabi, B.E., Dennis, D.J., Poole, R.J.: Turbulent drag reduction by polymer additives in parallel-shear flows. *Journal of Fluid Mechanics* **827** (2017).

37. Japper-J, A., Escudier, M., Poole, R.: Turbulent pipe flow of a drag-reducing rigid “rod-like” polymer solution. *Journal of Non-Newtonian Fluid Mechanics* **161**(1-3), 86-93 (2009).
38. Malkin, A.Y., Isayev, A.: *Viscoelasticity. In.*, 43-120. ChemTec Publishing, Toronto, (2006)
39. Ptasinski, P., Nieuwstadt, F., Van Den Brule, B., Hulsen, M.: Experiments in turbulent pipe flow with polymer additives at maximum drag reduction. *Flow, Turbulence and Combustion* **66**(2), 159-182 (2001).
40. Wedgewood, L.E., Bird, R.B.: From molecular models to the solution of flow problems. *Industrial & Engineering Chemistry Research* **27**(7), 1313-1320 (1988).
41. Luiz Costalonga, M., Venturini Loureiro, B., Soares, E.J.: Drag reducing flows by polymer solutions in annular spaces. *Journal of Fluids Engineering* **140**(5) (2018).
42. Jones Jr.,: An improvement in the calculation of turbulent friction in rectangular ducts. *Journal of Fluids Engineering*, **98**(2), 173-180 (1976).

Chapter 6 Reynolds-averaged Simulation of the Fully Developed Turbulent Drag Reduction Flow in Concentric Annuli Using the FENE-P Model

This chapter is based on a published journal article: Xiong X., Zhang Y., Rahman A.: Reynolds-averaged simulation of the fully developed turbulent drag reduction flow in concentric annuli, *ASME Journal of Fluids Engineering*, **142**(10), 101209 (2020). I conducted all the simulations, prepared the manuscript, and made the revisions during the publication process. Dr. Aziz Rahman and Dr. Yan Zhang provide essential supports and suggestions while running the simulations and writing the paper.

6.1 Introduction

Modifying the turbulence character of Newtonian fluid by adding an appropriate amount of high molecular weight, long-chain polymer has been a major approach for reducing the frictional pressure drop in wall-bounded flow since it was first reported by Toms [1]. This phenomenon, regarded as drag reduction (DR), has attracted a plethora of research interest, attributed to its significance both from the practical and fundamental points of view for the engineering community.

Despite an abundance of studies conducted in the past, the two most important experimental findings were reported by Virk [2,3], showing the existences of the onset and the upper limit of DR [4]. These studies contributed significantly to the establishments of the two principle concepts that have been widely cited to explain polymer-induced DR theoretically. The first, proposed by Lumley [5,6] and widely referred to as the extensional viscosity hypothesis, is based on the polymer extension mechanism, suggesting that DR is mainly caused by the stretching of randomly coiled polymers that primarily occurs in the highly deformed region, such as the buffer layer in a wall-bounded flow. Such stretching increases the effective viscosity of polymer solutions, leading to the thickening of the viscous sublayer. This thickened viscous sublayer suppresses the turbulent eddies near the wall and enhances DR. Contrarily, Gennes [4] proposed an elastic theory, claiming that the elastic features of the polymers are the primary cause of DR. He argued that the extensional-viscosity theory can explain neither the onset nor the upper limit of DR and that DR can occur even before the polymer molecules have reached the solid wall after they are injected far away from

the wall in a pipe or channel. Nevertheless, both theories are qualitative and fail to explain the dynamics of turbulent DR quantitatively [7].

Improvements of computational capability and advances in numerical methods have made it possible to investigate turbulent DR both qualitatively and quantitatively by direct numerical simulation (DNS), which helps expose more details of the mechanisms underlying the behavior of the polymer-induced DR. Interactions between a turbulent flow field and polymer additives have recently been investigated extensively by DNS lately, by which the finitely extensible non-linear elastic-Peterlin (FENE-P) model gains its popularity, characterizing both the viscous and elastic features of the polymers directly. This constitutive model allows each individual parameter of polymer additives to be investigated independently, such as the relaxation time, the polymer elasticity, and the viscosity, making it possible to reveal their sole contributions to the DR behaviors [8].

Although significant progress has been made in DNS for modeling turbulent DR, its drawbacks are obvious and have been discussed in detail by Pinho et al.[9]. Specifically, the extremely high computational expenses required for conducting such a simulation is the main obstacle to its being applied to most practical engineering problems. Therefore, an alternative approach, such as the Reynolds-averaged Navier-Stokes (RANS) type, needs to be developed for solving real engineering problems with relatively high Reynolds numbers. Pioneer research in this area, for example, that of Poreh et al. [10], proposed empirical correlations to tune the model constants in the standard $k-\varepsilon$ model, and successfully achieved DR by controlling the average velocity

profiles in the buffer layer. However, their method fails to include any rheological input in the turbulence model to represent the presence of polymers.

Fortunately, a recent expansion of DNS studies in this field has made it possible to apply the FENE-P model to the RANS framework, where proper model closures have been proposed by analyzing the DNS results so that interactions between the polymer additives and the turbulence variables can be modelled for turbulent DR flow. Generally, a RANS based approach involving the FENE-P model bridges the flow field and polymers numerically by adding additional polymer stress to the original momentum equation, where the added stress term is estimated by solving a transportation equation of the polymer conformation, which describes the extension and orientation of the polymer chains at the microscopic level [11]. Nonetheless, the introduction of the FENE-P model to the RANS approach leads to unsolved non-linear terms, containing either the polymer stress or the conformation tensor of the polymers that require additional closures. Hence, to develop corresponding closures that are most reliable in the RANS approach has been one of the main topics in the past decade to reduce the cost of simulating turbulent flow with DR behaviors.

The primary effort involved developing such closures within the framework of the standard low Reynolds number (LRN) k - ε model [9,10,12] until Resende et al. [12] concluded that the traditional k - ε based turbulence model cannot properly predict the flow field of polymer solutions at high DR. They explained that in DR polymer solutions, the magnitude of turbulence anisotropy increased dramatically with the increase in DR, while the k - ε model is limited by its inherent isotropic turbulence

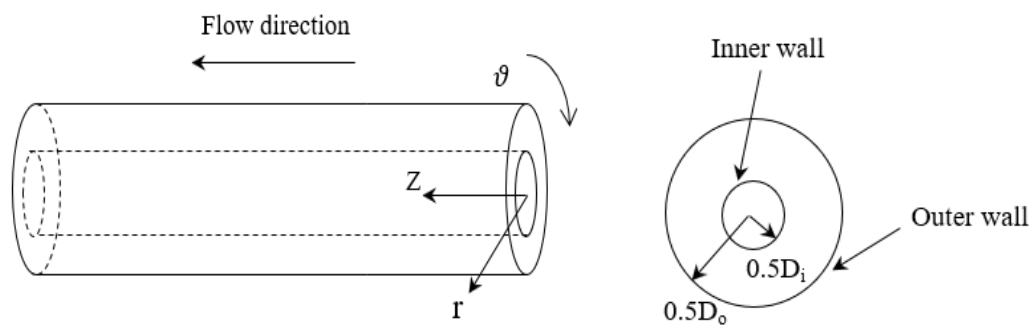
assumption, leading to unrealistic predictions of turbulence at high DR. To this end, Iaccarino et al. [13] developed closures for polymer-induced turbulent DR flow based on the $k-\varepsilon-\overline{v^2}$ - f model, where the velocity variance $\overline{v^2}$ has been specially designed to characterize the near-wall anisotropic turbulence. Their closures were reported to successfully capture the behavior of turbulent channel flow up to the maximum DR. Further they demonstrated that the postulation of the $k-\varepsilon-\overline{v^2}$ - f model [14] for Newtonian fluids is also suitable for polymer solutions, emphasizing the dominant role played by the wall-normal fluctuation of turbulence on the eddy viscosity in the near-wall region. Thus, no damping function is needed to reduce turbulence activity at the wall. Their model was later tested and improved by Masoudian et al. [8] with new closures. However, this model only considers the extension of polymer chains, neglecting the effects of its orientation. Most recently, Masoudian et al. [15] addressed this issue by further improving their closures, providing the most reliable RANS model to date for modelling turbulent DR flow with polymer additives.

Despite being extensively analyzed in the channel, polymer-induced Turbulent DR in an annulus has not been sufficiently investigated. This scenario is essential to drilling operations, as the flow path for circulating the drilling mud formed by the drill string and the well casing is extremely similar to a concentric annulus. Turbulent flow in such geometry also widely exists in gas-cooled nuclear reactors and heat exchangers [16]. Given that most drilling fluids express non-Newtonian behavior, DR flow in the annulus deserves more attention. In general, two different boundary layers exist in the annulus due to the transverse curvature of this geometry. Xiong et al. [17] analyzed the

fully developed turbulent flow for Newtonian fluid in the concentric annulus with the RANS approach at various Reynolds numbers and with different radius ratios, and they reported that the transverse curvature of the annulus affected the flow field significantly. Since the DR feature of polymers is highly dependent on the geometry of the flow path [18,19], how polymers additives behave with the transverse curvature of an annulus needs to be accurately accessed in order to successfully characterize the DR flow in the annulus. However, to the best of the author's knowledge, no such numerical study has been conducted. Therefore, the present study aims to fill the gap in this area and shed light on how the interactions between polymer additives and the curved walls of the annulus affect the turbulent flow field and the DR behaviors of polymers.

6.2 Numerical Models

The same numerical models presented in Chapter 5 were employed to carry out the simulations for polymer induced DR in the annulus. The behavior of the polymer solution is characterized by the FENE-P model and the modified $k-\varepsilon-\overline{v^2}-f$ model is used to model the turbulence.



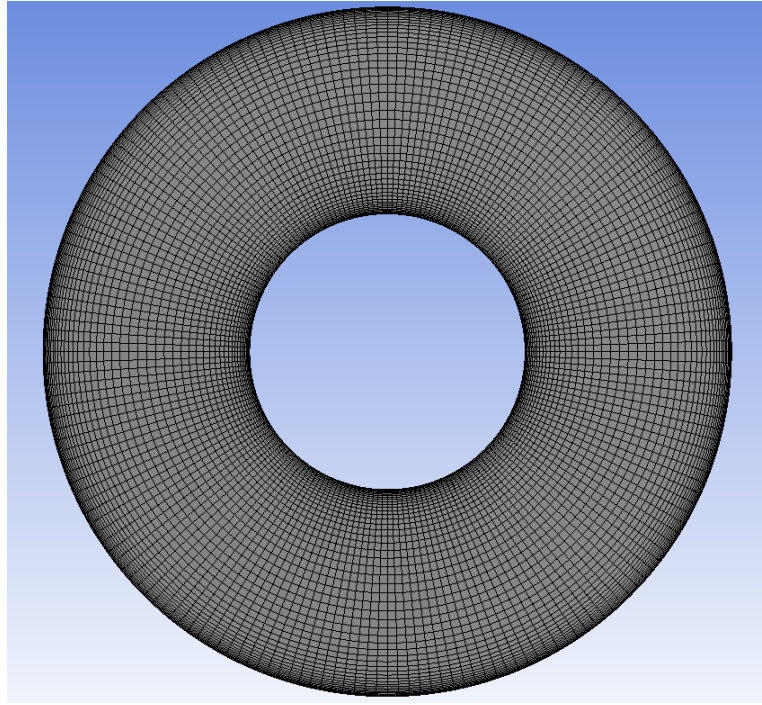


Fig. 6- 1 Scheme and Mesh of the Flow Domain

Table 6- 1 Mesh Independence Test

No. of Layers	DR (%)
64	17
100	25
128	31
168	31
200	31

The commercial software of ANSYS-FLUENT was used to solve the numerical models. Governing equations were discretized using a finite volume method with 128 computational cells in the wall-normal direction, as shown in Fig. 6-1. In the simulation, a radius ratio between the inner and outer cylinders of $\theta = R_1/R_2 = 0.4$, the same as that used by Xiong et al. [17] and Rodriguez-C et al. [20], was adopted. To further

ensure the accuracy of the simulation results, a mesh independency test has been performed, and the results are shown in Table 6-1 with the cell numbers ranging from 63 to 199 in the wall-normal direction, suggesting the sufficiency of the present mesh for predicting accurate DR.

6.3 Results and Discussions

Before proceeding further, simulation results from the current study are validated against DNS from Masoudian et al. [15] at close DR. The properties of flow scenarios from which the present simulation results were obtained are listed in Table 6-2, in which Re and We are the Reynolds number and the Weissenberg number, relating the viscous force to the inertial and elastic forces of the flow respectively, $u_\tau = \sqrt{\frac{\tau_w}{\rho}}$ is the frictional velocity, m/s , τ_w is the wall shear stress, Pa , and $D_h = D_{out} - D_{in}$ is the hydraulic diameter of the annulus [21]. In this validation, simulations were conducted at constant Re and L , as can be seen in Table 6-2, where L is the dimensionless maximum elongation length of polymers, while We was tuned in each scenario until the anticipated DR was achieved. As the reference for the near-wall comparison, turbulent flow of the Newtonian fluid is also simulated and plotted, together with asymptotes representing the universal law of the wall for Newtonian fluid suggested by Kármán [22]:

$$U^+ = \begin{cases} Y^+, Y^+ < 10 \\ 2.5 \ln Y^+ + 5.5, Y^+ > 30 \end{cases} \quad (6-1)$$

along with the empirical profile of non-Newtonian DR fluid at maximum DR suggested by Virk [3]:

$$U^+ = 11.7 \ln Y^+ - 17, Y^+ > 30 \quad (6-2)$$

where $U^+ = U/U_\tau$, $Y^+ = \rho y U_\tau / \mu_0$, and y is the distance from the test location to the nearest wall. Satisfactory agreement is reached in Fig. 6-2 for DR fluid, where velocity profiles for the present study match well with the ones predicted by DNS, both positioning well above the universal law for Newtonian fluid in the log-law region ($Y^+ > 30$), indicating the existence of DR. Validations are also conducted for the turbulent kinetic energy k and the velocity various term v^2 in Fig. 6-3 with complementary agreement. This preliminary validation confirms the efficiency of the present simulations for predicting accurate turbulent DR flow with corresponding DR. Consequently, as the primary objective of the present study, simulation results are further analyzed to expose the behavior of the modeled DR fluid in the annular geometry.

Table 6- 2 Summary of Flow Parameters

Case	$Re =$	$We = \frac{4\lambda U_b}{D_h}$	$Re_{\tau_0} = \frac{\rho U_\tau D_h}{4\mu_0}$		L^2	β	DR (%)
	$\frac{\rho U_b D_h}{4\mu_0}$	In	Out				
Newtonian	10587		648	620		1	0
(a)	10587	1.7	539	489	900	0.9	19
(b)	10587	4.4	467	436	900	0.9	38
(c)	10587	6.8	414	391	900	0.9	51
(d)	10587	1.7	494	445	10000	0.9	34
(e)	10587	4.4	447	410	10000	0.9	44
(f)	10587	6.8	370	344	10000	0.9	61

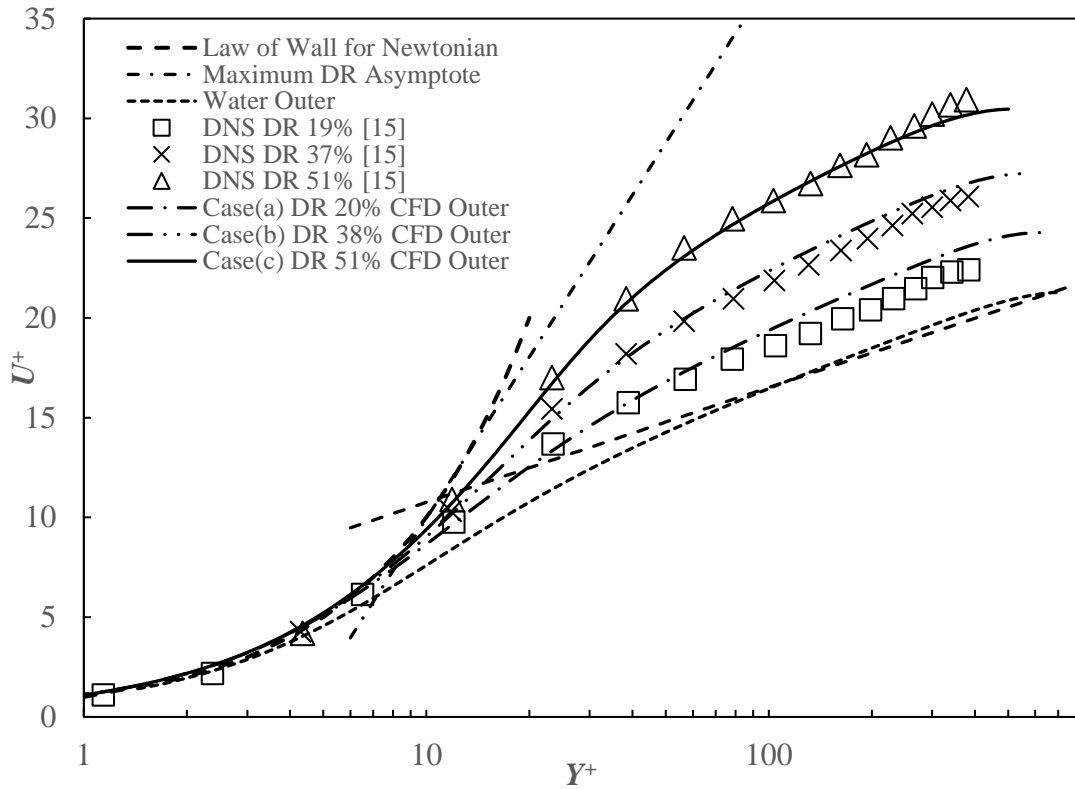
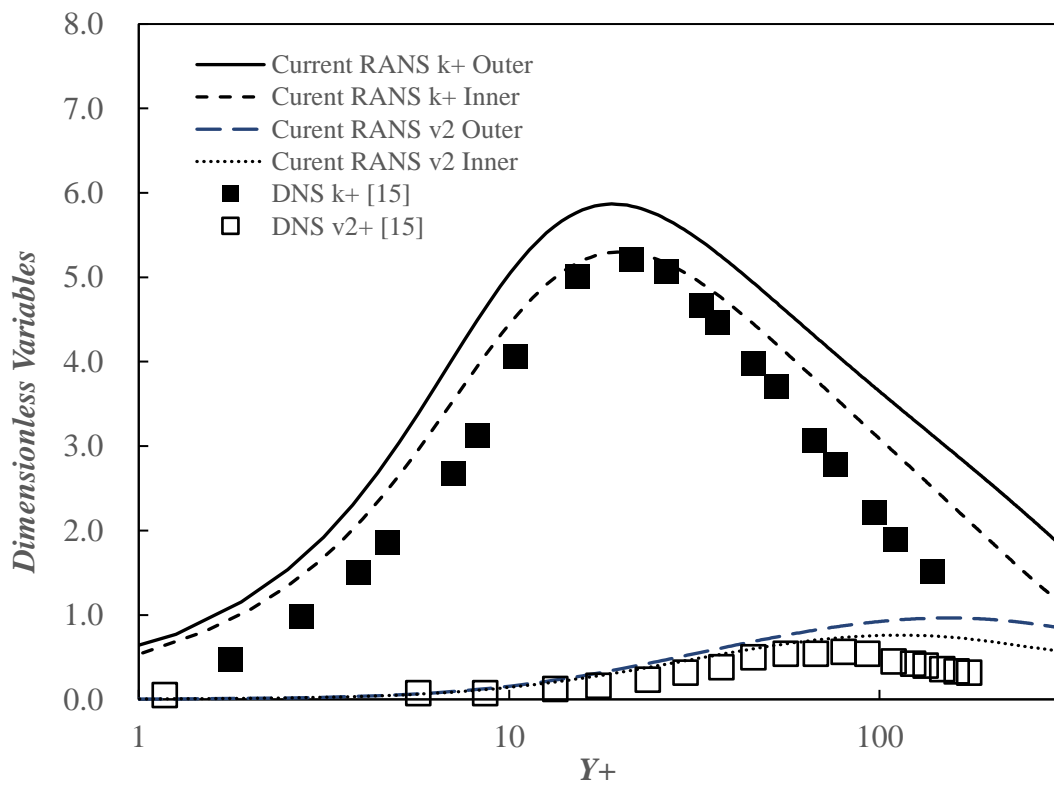
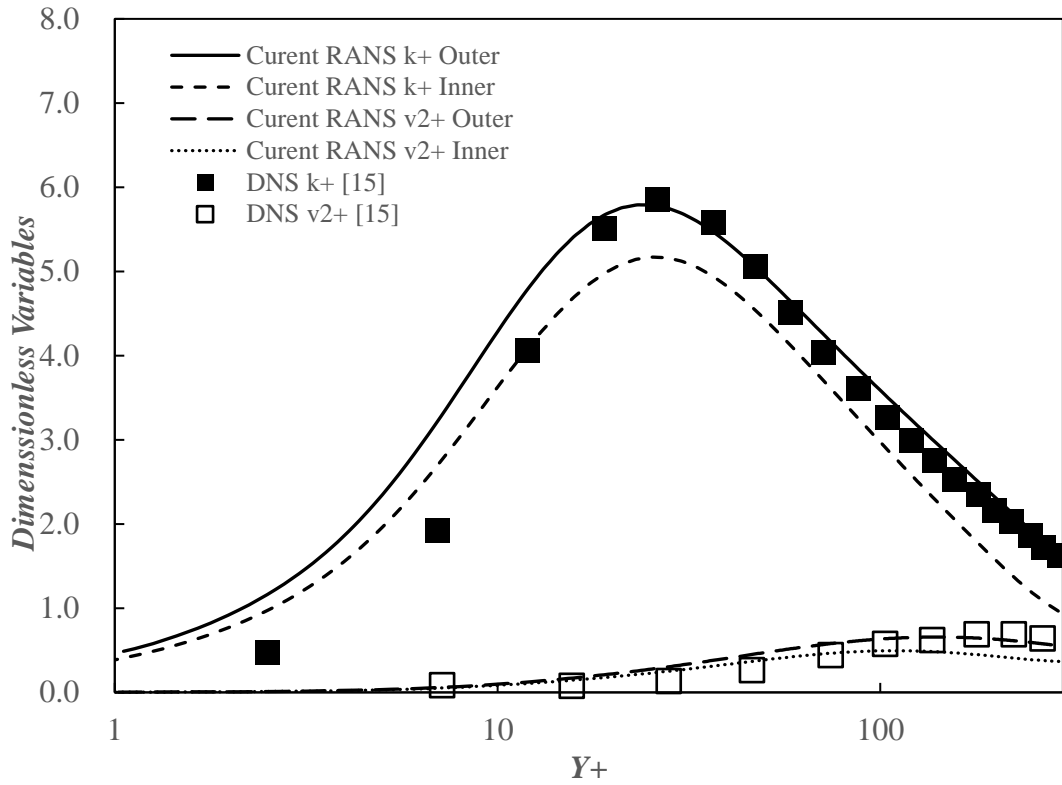


Fig. 6- 2 Validation of Current Simulation Results towards DNS at Different DR

(I) Case(a) DR=19% We=1.7 L=30



(II) Case(b) DR=38% We=4.4 L=30



(III) Case(c) DR=51% We=6.8 L=30

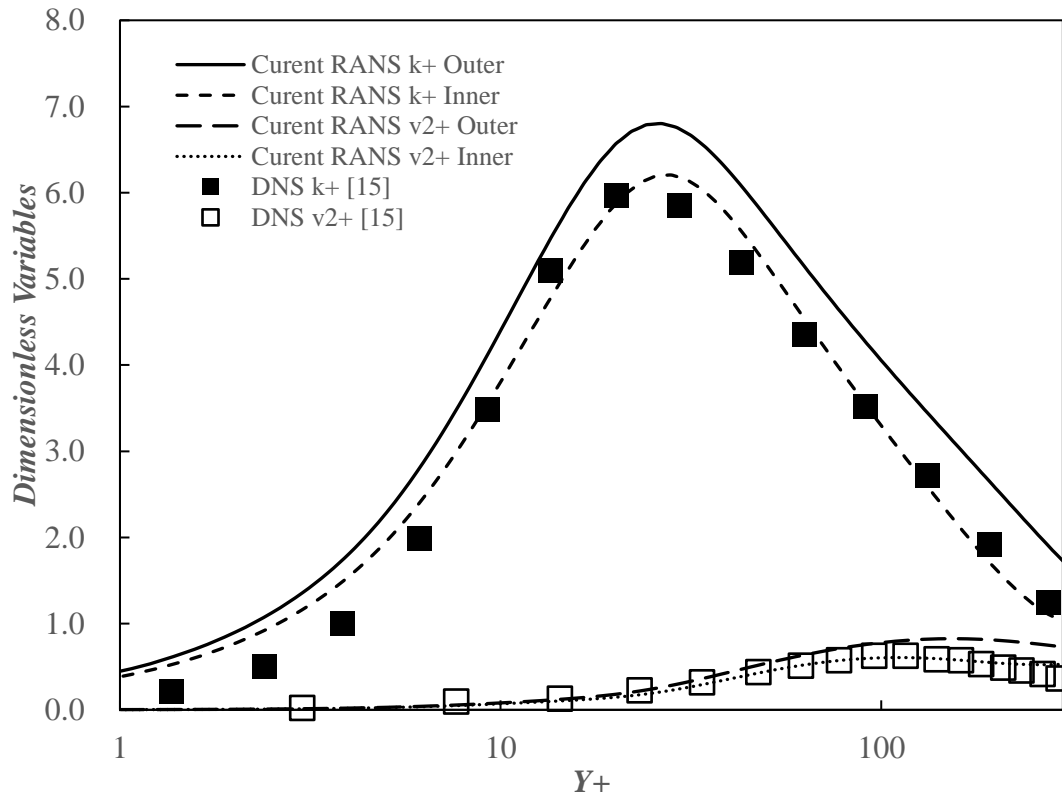


Fig. 6- 3 Comparison of TKE and $\overline{v^2}$ with Different DR

6.3.1 Mean Velocity profiles

First, the mean streamwise velocity profiles near both walls of the annulus are compared, with (DR fluid) and without (Newtonian fluid) polymer additives, in Fig. 6-4. As can be seen in this figure, the velocity profile of the DR fluid at the inner wall is positioned clearly below its outer wall counterpart, expressing the same behavior of the Newtonian fluid, mainly due to the transverse curvature feature of the annular geometry [16, 21]. However, a much more pronounced discrepancy can be seen in the figure for DR fluid, suggesting a strengthened consequence of the curvature effect being experienced by the DR fluid, leading to the redistribution of velocity profiles. Since the comparison is conducted in the same annulus with the same Reynolds number, this phenomenon must be caused by the elastic feature of the polymer additives. Hence, further comparison has been conducted for the velocity profiles with different Weissenberg numbers, with the aim of showing how the strengthened consequence of the curvature effect is influenced by the rheological properties of the polymers.

Fig. 6-5 illustrates the near-wall velocity profiles of DR fluid with various Weissenberg numbers We but with the same maximum elongation $L = 30$. According to the results, DR surges with the boost in Weissenberg number though as anticipated [8,13,15,23], the discrepancy between the inner and outer velocity profiles found in Fig. 6-4, which represents the impact of the transverse curvature on the flow field, seems to have a reverse trend. Particularly, as seen in this figure, with a relatively lower Weissenberg number $We = 1.7$ and lower DR=19% in case (a), the velocity profiles of the flow are shown to have a larger discrepancy, while the flow in case (b), with

relatively larger Weissenberg number $We=4.4$ and higher DR=38%, is shown to have a smaller discrepancy. This trend further extends to case (c), where the Weissenberg number is even higher. A separate comparison has also been conducted in Fig 6-6, for flows with the same range of Weissenberg numbers but containing polymers with a larger maximum elongation of $L=100$, and the results are consistent. Since the transverse curvature effect of an annular geometry on the turbulent flow field can be properly revealed by the redistribution of the velocity profile [16,17,21,24], these two figures demonstrate how the consequence of such an effect is dependent on the rheological properties of the polymer. However, by what mechanism it achieves this remains to be unknown and requires further assessment.

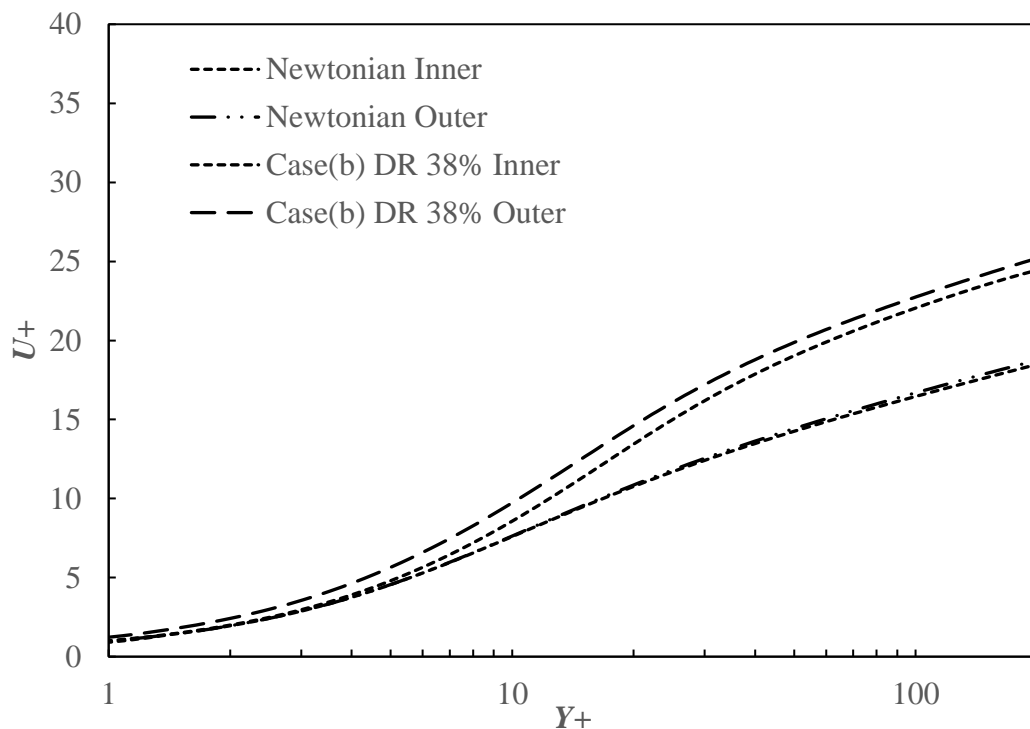


Fig. 6- 4 Comparison of Near-wall Velocity Profiles with and without Polymer Additives

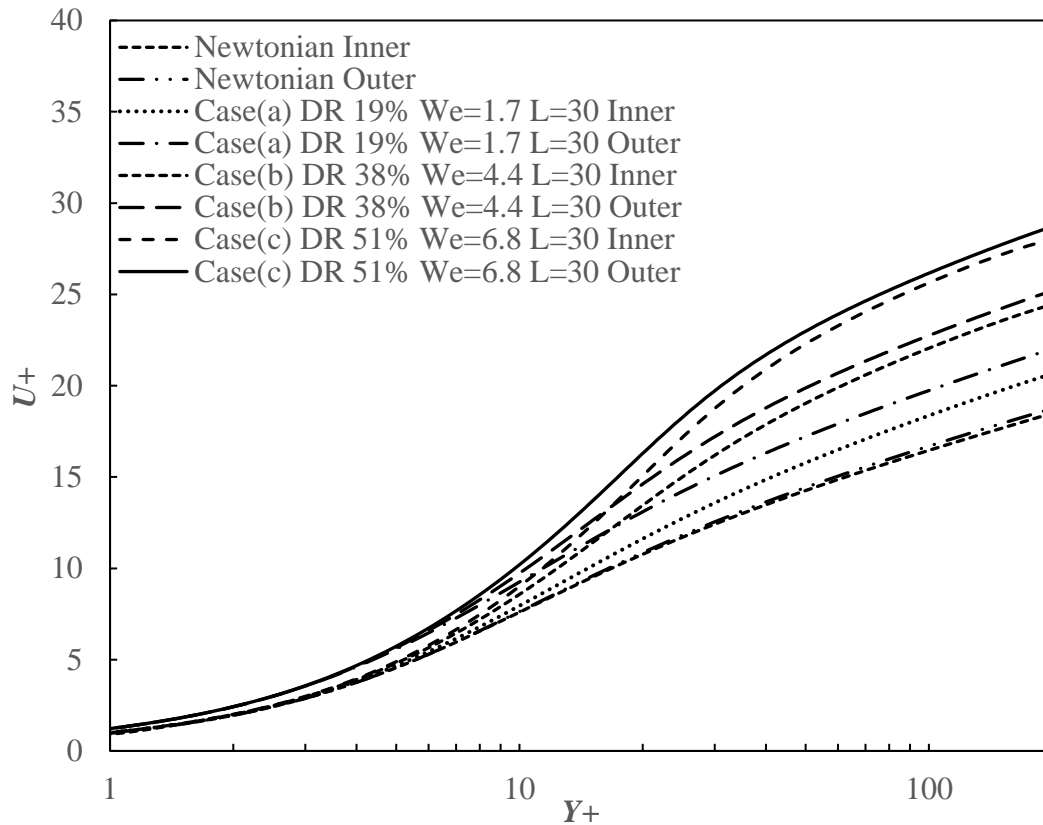


Fig. 6- 5 Comparison of Near-wall Velocity Profiles at $L=30$

6.3.2 Reynolds Stress

As shown in the discussion of the near-wall velocity, and also well-known from the literature [17,21,24], the essential role played by the transverse curvature of the annular geometry in a turbulent flow is attributed to its ability to support two different turbulent boundary layers (TBL), which, in the present study of a concentric annulus, is mainly due to the different surface areas of the two curved walls that support different strengths of turbulence. In the RANS simulation of turbulent flow, Reynolds stress represents the explicit effect of turbulence on the momentum equation and thus should be next to be investigated, as an effort to expose the mechanism by which the polymer additives are utilized to modify the velocity field in the annulus.

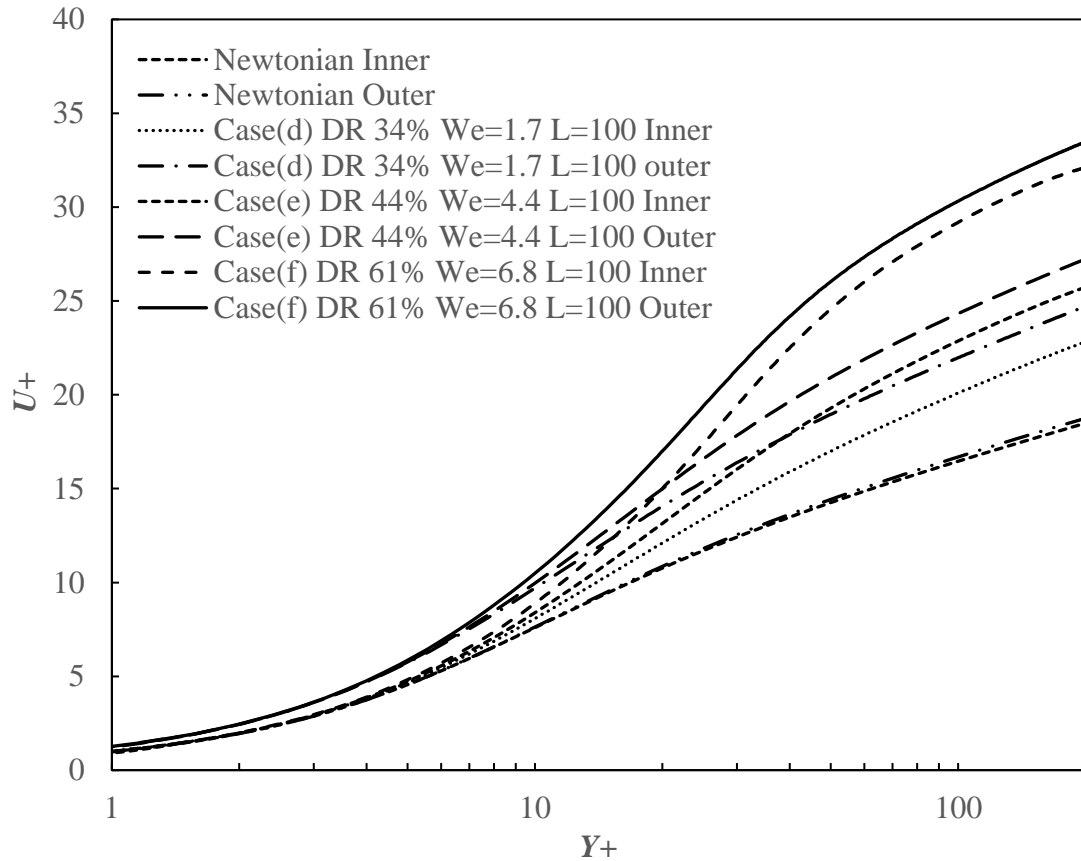
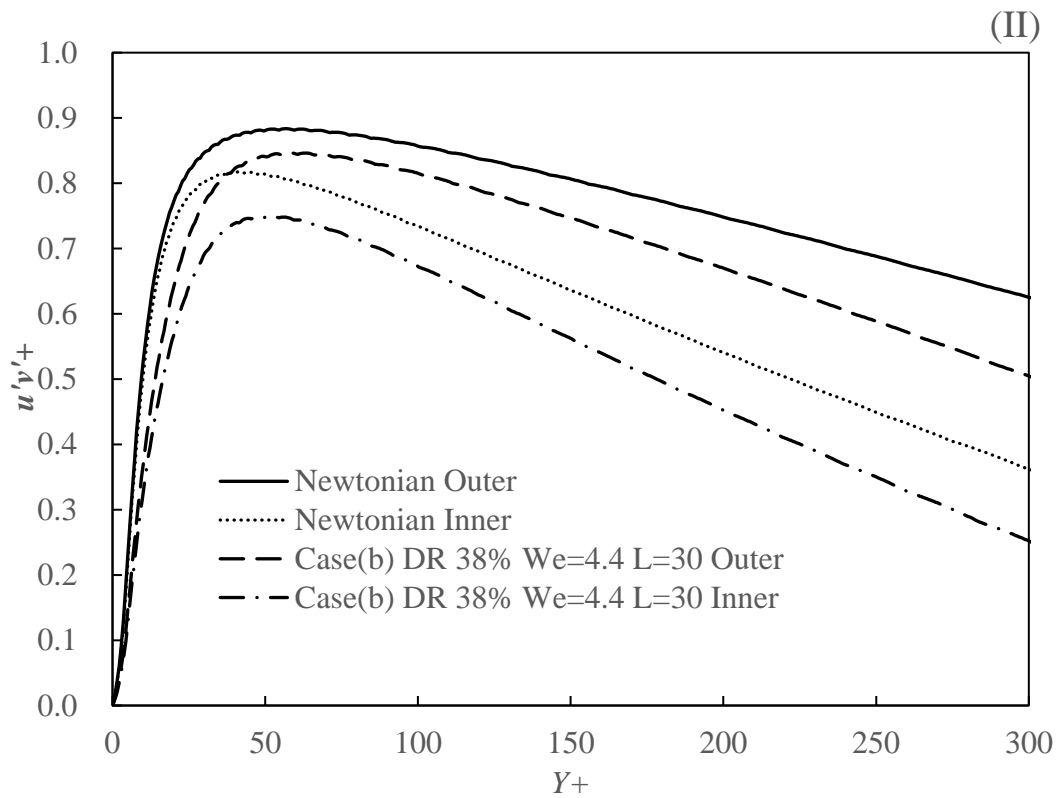
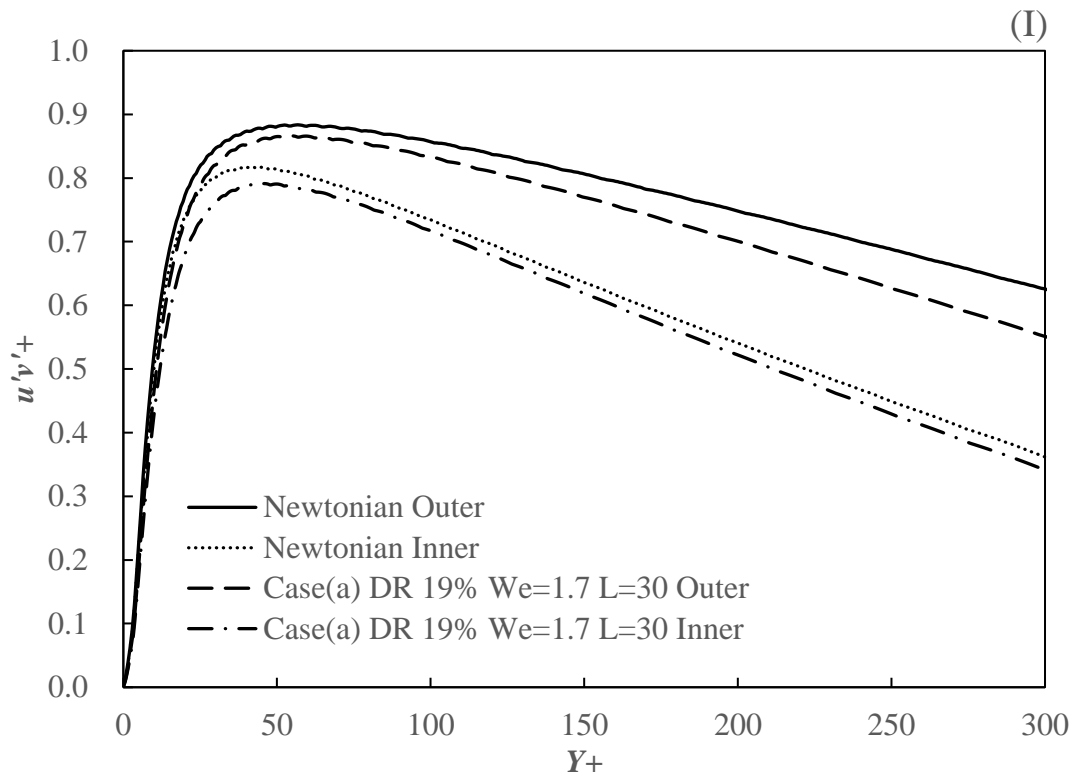


Fig. 6- 6 Comparison of Near-wall Velocity Profiles at L=100

Consequently, a similar comparison has been conducted for the Reynolds stress, and the results are shown in Fig. 6-7 and Fig. 6-8. According to Dubief et al. [23], polymer additives dampen the streamwise vortices in the buffer layer, the main source of turbulence and frictional drag, leading to DR. Thus, flow cases with larger Weissenberg numbers, and thus higher DR, are supposed to carry lower Reynolds stresses, which is well illustrated in these two figures. Also, flows with higher DR are also shown to have thicker viscous sublayers, as the peaks of Reynolds stresses shift away from the wall for flows with higher DR, compared to the ones with lower DR. Both findings for the Reynolds stress in the annulus are consistent with the ones reported by [8, 15] for the plane channel flow.



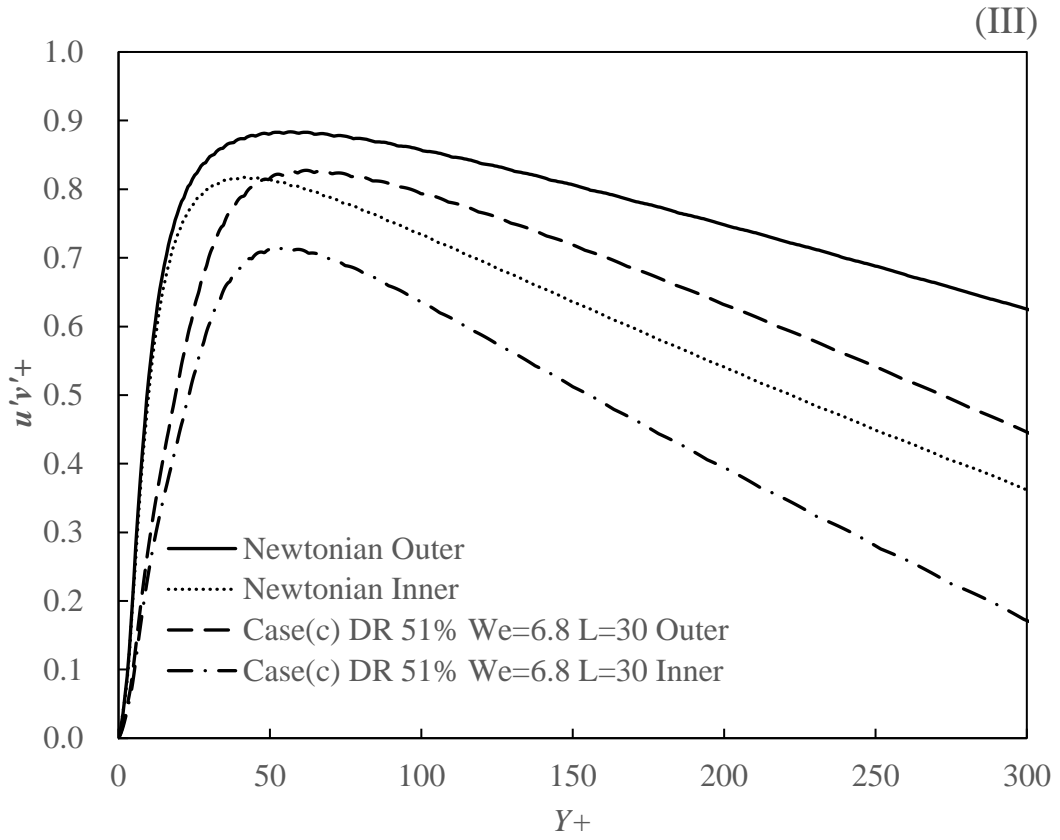
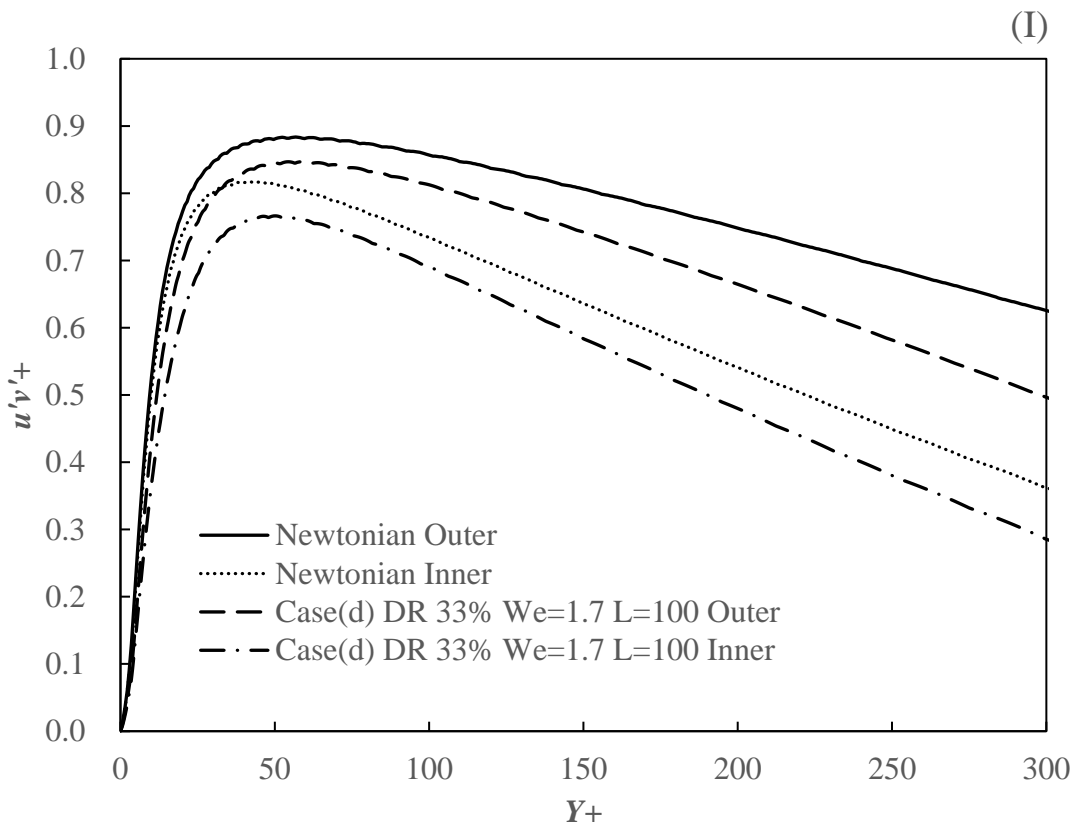


Fig. 6- 7 Comparison of Reynolds Stress Profiles at L=30



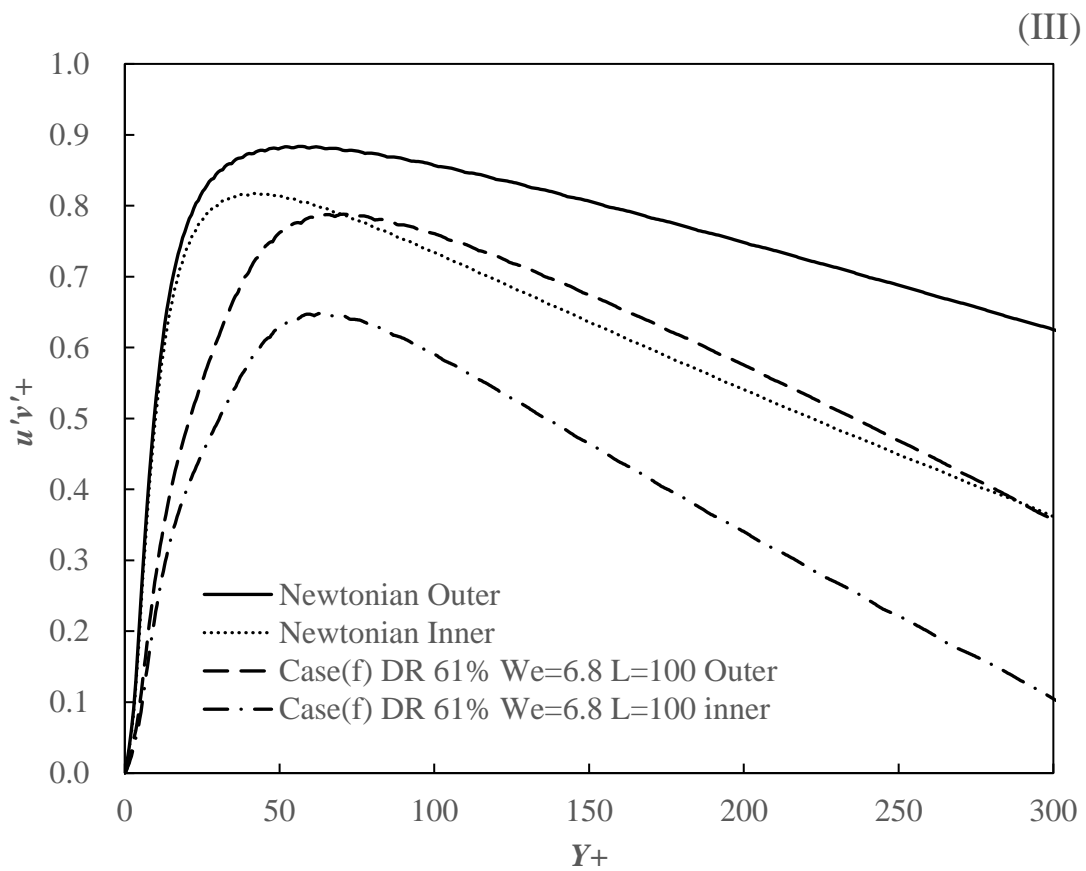
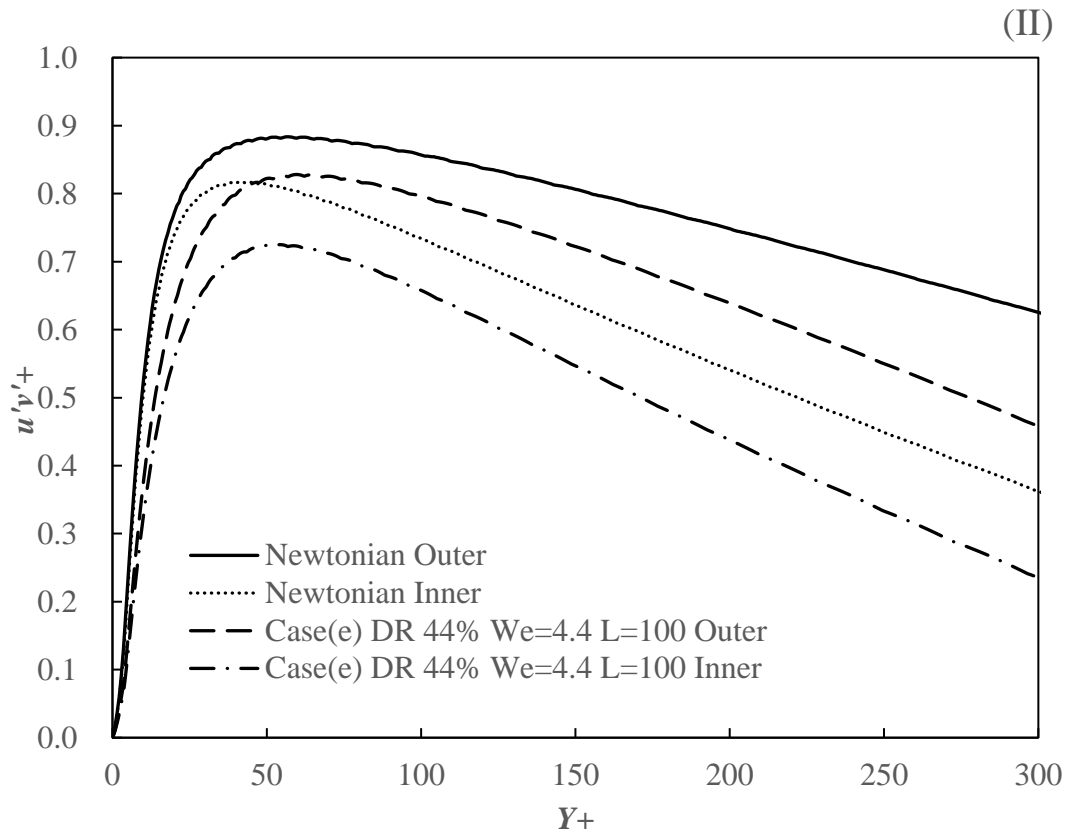


Fig. 6- 8 Comparison of Reynolds Stress Profiles at L=100

The more important finding for the Reynolds stress profile, however, for the annulus, is that it has a similar trend as the near-wall velocity as it pertains to the change in the rheological properties of the polymer. As demonstrated in Fig. 6-7(I), when relatively lower DR in flow case (a) is achieved by a smaller Weissenberg number, We , the Reynolds stress at the outer wall is found to be dampened more significantly than its inner wall counterpart, increasing the difference in the flow; while in Fig. 6-7(III), when We is increased in case (c) to achieve a relatively higher DR, the decay of the Reynolds stress near both walls of the annulus becomes comparable, and obviously less distinguishable compared to case (a). This finding successfully explains why the corresponding movement of velocity profiles has been found in Fig. 6-5 and Fig. 6-6 regarding the increase in Weissenberg number. Again, the same trend has also been found for the Reynolds stress profile in Fig. 6-8 for a polymer with a larger maximum elongation length.

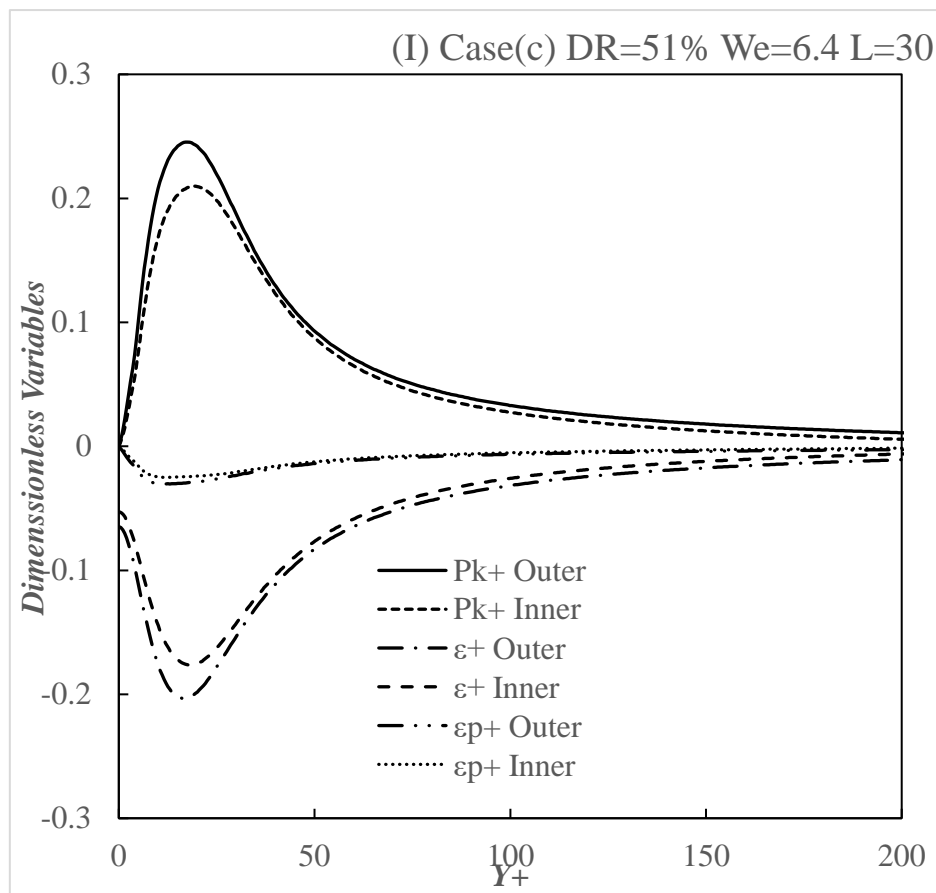
With the aim to further investigate the main causes behind the corresponding behavior of the Reynolds stress profile, the FENE-P model characterizing the polymer solution is invoked. As explained in the introduction section, the DR feature of the polymer additives is associated with the “coil-stretching” mechanism of its polymer chains, leading to the absorption of turbulent energy. Evidently, a more chaotic flow field existing near the outer wall, as a result of the transverse curvature effect in the annular geometry, is likely to enhance the stretching of the polymer chains, resulting in a larger decay of the Reynolds stress. Current results suggest that this effect is obvious at relatively low DR in case (a) and case (d) in their separate control groups, as an

observable larger dampening of Reynolds stress can be seen in Fig. 6-7(I) and Fig. 6-8(I), respectively. However, when more DR is anticipated from the flow, by increasing the Weissenberg number, We , it becomes relatively harder for the polymers near the outer wall to be further stretched, compared to the inner wall, since the polymer has already been stretched more intensely and the maximum elongation length of the polymer is held constant, as the controlling variable. Consequently, when the Weissenberg number is increased to enhance DR in case (c) and case (f), the continued decay of the Reynolds stress near the outer wall tends to be weaker, offsetting its strength seen at lower DR, and ultimately leading to a similar magnitude of dampening of the Reynolds stress profile near both walls, as shown in Fig. 6-7(III) and Fig. 6-8(III). This presents an idea about how the DR fluid, which can be most accurately characterized by a FENE-P model, interacts with the inherent transverse curvature feature of the annular geometry and modifies the flow field.

6.3.3 Turbulent Kinetic Energy Budget

While the turbulent kinetic energy (TKE) profile has already been briefly compared in the preliminary study, it is beneficial to show the whole sketch of its budget. As seen in the transport equation Eq (11), for a turbulent DR flow modeled with the viscoelastic model, the source terms of the TKE consist of the turbulence production P_k , m^2/s^3 , the viscous dissipation ε , m^2/s^3 , and the turbulent stretching ε_p , m^2/s^3 , instead of only the first two terms in a Newtonian flow, while the two remaining terms in this equation represent the diffusions of the TKE by the average and turbulent flow fields, which are self-conserved. Thus, all these three source terms, normalized as $P_k^+ = \frac{G_k \mu_s}{\rho^2 U_\tau^4}$,

$\varepsilon^+ = \varepsilon \mu_s / \rho U_\tau^4$, and $\varepsilon_p^+ = \varepsilon_p \mu_s / \rho U_\tau^4$, are compared and plotted in Fig. 6-9. A similar feature to the DR flow in the channel, the thickening of the viscous sublayer for flow with enhanced DR, is also predicted in the annulus, as the peaks of all the source terms shift away from the wall, due to the redistribution of the turbulence caused by the absorption-releasing mechanism of polymers [23].



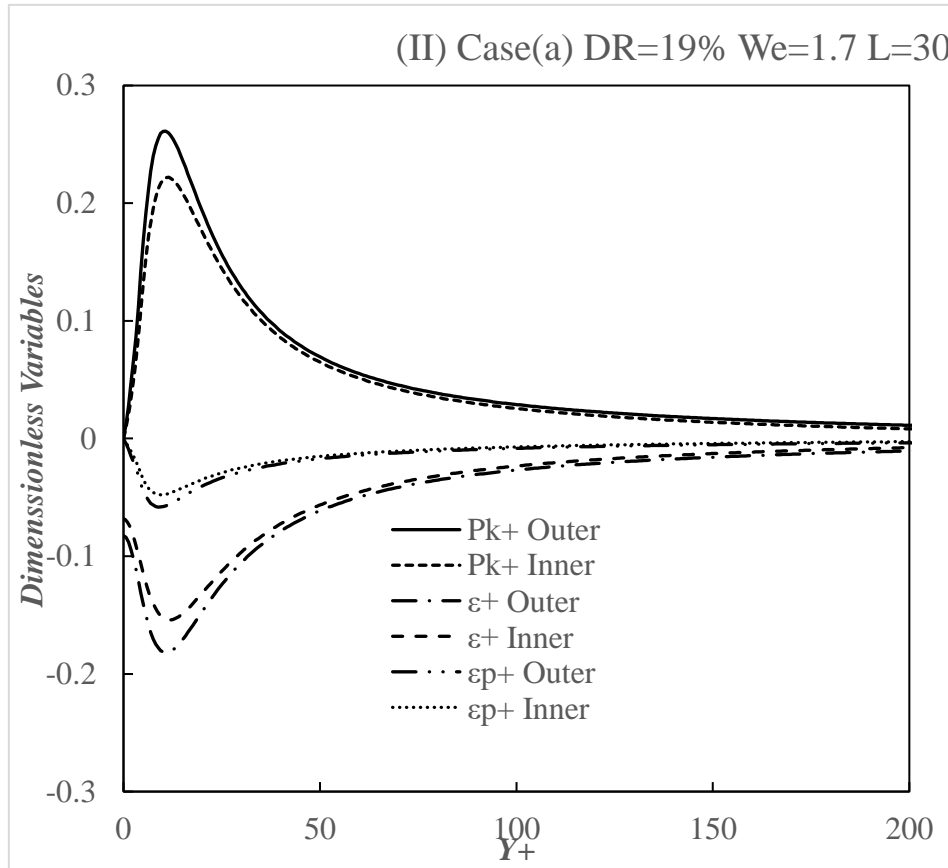


Fig. 6- 9 Comparison of TKE Budgets

Additionally, in this figure, a positive value means a boost for the TKE, while a negative value denotes a deficit. Therefore, the turbulence production is the only term making a positive contribution in this simulation, while both the turbulent stretching induced by the polymers and the viscous dissipation terms are making negative contributions to the TKE budget. Due to the curvature effect, higher magnitudes of all the source terms are present near the outer wall compared to those near the inner one. Also, as expected, with an increased Weissenberg number at larger DR, the turbulence production decreases, producing less TKE, and at the same time, the viscous dissipation increases, dampening more TKE. However, the turbulent stretching term shows a reverse trend, with case (a) at higher DR in Fig. 6-9 to have a relatively lower magnitude. This trend is not enough to change the ultimate trend of the TKE or the DR, in regards

to the change in the Weissenberg number, or, in other words, the rheological properties of the polymer, since it has a much weaker effect on the TKE budget compared to the other two source terms. However, it can play a major role in determining other characteristics, such as the discrepancy between the inner and outer flow fields in the annular geometry, which is inherently minor, as observed previously, and thus is more sensitive to even a slight change. This finding implies that the turbulent stretching term might be the key factor from the TKE budget to diversify the flow fields near the inner and outer walls in the annulus, by weighing more in the TKE budget at lower DR; and to eliminate the difference by weighing less in the TKE budget at higher DR, which, together with the findings from the previous sections, further explains how the polymers alter the turbulent flow field in the concentric annulus.

6.4 Conclusions

Drag reduction (DR) behavior of the non-Newtonian fluid in a concentric annulus is investigated numerically in this study at the fully developed flow regime, with a fixed inner to outer radius ratio of $\theta = 0.4$. The DR feature of the fluid is characterized by the FENE-P model and a modified $k-\varepsilon-\overline{v^2}$ - f model is used to estimate the interactions between the polymer additives and the turbulent flow field. Overall, the present model shows a robust performance of predicting turbulent DR, with satisfactory agreement obtained between current simulations and available DNS results. The near-wall axial velocity, Reynolds stress, and turbulent kinetic energy (TKE) budget near both walls of the annulus (fixed radius ratio of 0.4) are compared in detail at a constant Reynolds

number ($Re = 10587$) and various rheological parameters (Weissenberg number We in the range of 1 to 7 and the maximum polymer elongation $L = 30$ and 100).

The objective of this work is to uncover the DR flow field in the concentric annulus, with the essential focus on exposing how the effect of transverse curvature is altered by the DR features of the polymers. In order to do so, simulations were conducted in the RANS framework at the same Reynolds number and different Weissenberg numbers, to account for the changes in the rheological parameters. According to the simulation results, the two different turbulent boundary layers (TBL) sustained along the cross-section of the annulus tend to redistribute with the presence of the polymers. By investigating the average near-wall velocity, the Reynolds stress, and the turbulent kinetic energy (TKE) of the flow, it has been demonstrated that this change is mainly induced by the elongation feature of the polymers. Near the outer wall, since the turbulence is stronger, the polymers are stretched more intensely, decaying more turbulence; whereas near the inner wall, the polymers will be stretched less intensely due to the weaker turbulence, decaying less turbulence. Additionally, the redistribution of the turbulent flow field is found to be dependent on the rheological properties. The current study provides a benchmark work, showing how the evolution of turbulent flow fields among different DR fluids in the annulus can be numerically predicted by using an available RANS model.

6.5 References

1. Toms, B.A.: Some observations on the flow of linear polymer solutions through straight tubes at large Reynolds numbers. Proceedings of the 1st International Congress on Rheology, 135-141. North-Holland Amsterdam (1948).
2. Virk, P.S., Merrill, E., Mickley, H., Smith, K., Mollo-Christensen, E.: The Toms phenomenon: turbulent pipe flow of dilute polymer solutions. *Journal of Fluid Mechanics* **30**(02), 305-328 (1967).
3. Virk, P.: An elastic sublayer model for drag reduction by dilute solutions of linear macromolecules. *Journal of Fluid Mechanics* **45**(03), 417-440 (1971).
4. Gennes, P.G.D.: Introduction to polymer dynamics. Cambridge University Press (1990)
5. Lumley, J.L.: Drag reduction by additives. *Annual Review of Fluid Mechanics* **1**(1), 367-384 (1969).
6. Lumley, J.L.: Drag reduction in turbulent flow by polymer additives. *Journal of Polymer Science: Macromolecular Reviews* **7**, 263-290 (1973).
7. Ptasinski, P., Boersma, B., Nieuwstadt, F., Hulsen, M., Van den Brule, B., Hunt, J.: Turbulent channel flow near maximum drag reduction: simulations, experiments and mechanisms. *Journal of Fluid Mechanics* **490**, 251-291 (2003).
8. Masoudian, M., Kim, K., Pinho, F., Sureshkumar, R.: A viscoelastic $k-\varepsilon-\overline{\sqrt{2}}-f$ turbulent flow model valid up to the maximum drag reduction limit. *Journal of Non-Newtonian Fluid Mechanics* **202**, 99-111 (2013).

9. Pinho, F., Li, C., Younis, B., Sureshkumar, R.: A low Reynolds number turbulence closure for viscoelastic fluids. *Journal of Non-Newtonian Fluid Mechanics* **154**(2), 89-108 (2008).
10. Poreh, M., Hassid, S.: Mean velocity and turbulent energy closures for flows with drag reduction. *Physics of Fluids* **20**(10), S193-S196 (1977).
11. Bird, R., Dotson, P., Johnson, N.: Polymer solution rheology based on a finitely extensible bead—spring chain model. *Journal of Non-Newtonian Fluid Mechanics* **7**(2-3), 213-235 (1980).
12. Resende, P., Kim, K., Younis, B., Sureshkumar, R., Pinho, F.: A FENE-P $k-\epsilon$ turbulence model for low and intermediate regimes of polymer-induced drag reduction. *Journal of Non-Newtonian Fluid Mechanics* **166**(12), 639-660 (2011).
13. Iaccarino, G., Shaqfeh, E.S., Dubief, Y.: Reynolds-averaged modeling of polymer drag reduction in turbulent flows. *Journal of Non-Newtonian Fluid Mechanics* **165**(7), 376-384 (2010).
14. Durbin, P.A., Near-wall turbulence closure modelling without damping functions. *Theoretical and Computational Fluid Dynamics* **3**(1), 1-13 (1991).
15. Masoudian, M., Pinho, F., Kim, K., Sureshkumar, R.: A RANS model for heat transfer reduction in viscoelastic turbulent flow. *International Journal of Heat and Mass Transfer* **100**, 332-346 (2016).
16. Nouri, J., Umur, H., Whitelaw, J.: Flow of Newtonian and non-Newtonian fluids in concentric and eccentric annuli. *Journal of Fluid Mechanics* **253**, 617-641 (1993).

17. Xiong, X., Rahman, M.A., Zhang, Y.: RANS Based Computational Fluid Dynamics Simulation of Fully Developed Turbulent Newtonian Flow in Concentric Annuli. *Journal of Fluids Engineering* **138**(9), 091202 (2016).
18. Cadot, O., Bonn, D., Douady, S.: Turbulent drag reduction in a closed flow system: Boundary layer versus bulk effects. *Physics of Fluids* **10**(2), 426-436 (1998).
19. Min, T., Yoo, J.Y., Choi, H., Joseph, D.D.: Drag reduction by polymer additives in a turbulent channel flow. *Journal of Fluid Mechanics* **486**, 213-238 (2003).
20. Rodriguez, -C. F. F., Bizhani, M., Ashrafuzzaman, M., Kuru, E.: An experimental investigation of turbulent water flow in concentric annulus using particle image velocimetry technique. *Journal of Fluids Engineering* **136**(5), 051203 (2014).
21. Chung, S.Y., Rhee, G.H., Sung, H.J.: Direct numerical simulation of turbulent concentric annular pipe flow: Part 1: Flow field. *International Journal of Heat and Fluid Flow* **23**(4), 426-440 (2002).
22. Kármán, Th.: Mechanical similitude and turbulence. Tech. Mem. NACA, No. 611 (1993).
23. Dubief, Y., White, C.M., Terrapon, V.E., Shaqfeh, E.S., Moin, P., Lele, S.K.: On the coherent drag-reducing and turbulence-enhancing behaviour of polymers in wall flows. *Journal of Fluid Mechanics* **514**, 271-280 (2004).
24. Liu, N.S., Lu, X.Y.: Large eddy simulation of turbulent concentric annular channel flows. *International Journal for Numerical Methods in Fluids* **45**(12), 1317-1338 (2004).

Chapter 7 Summary of Thesis and Future Works

7.1 Summary

In this thesis, the turbulent flows of Newtonian and non-Newtonian drag reduction fluids are investigated numerically in cylindrical geometries. The main contributions of this study are summarized as follows:

- A benchmark CFD study is provided using the commercial software of ANSYS-CFX to show for the first time how the powerful commercial code can be used to investigate the turbulent flow field influenced by the transverse curvature in the cylindrical annular geometry. By conducting simulations of turbulent flows in the annulus with different radius ratios and different Reynolds numbers, present results successfully reveal the more pronounced dependence of flow statistics on the curvature effect than the Reynolds number.
- One of the default non-Newtonian models in ANSYS-CFX, the power-law model, is tested and shown unable to predict the turbulent drag reduction feature of shear-thinning fluid. The test confirmed that this group of models, lacking rheological representations of the polymer solution, is not capable of properly reflecting the change of stress term caused by polymer additives in the non-Newtonian fluid and thus predict inaccurate friction drags. However, the present study found that improved prediction can be achieved by adjusting constants of the standard turbulence model to manually achieve DR, which serves as a sound approach in

engineering applications, where simulations of drag reduction involving more complicated models could be too difficult to realize.

- A RANS method with proper molecular representations of polymer solutions using the FENE-P model is proposed with the $k-\varepsilon-\overline{v^2}-f$ turbulence model for simulating the turbulent drag reduction in cylindrical geometries and provides satisfactory friction drags compared to experimental results of various polymer solutions. More reliable validations of simulation results obtained using the commercial solvers of ANSYS-FLUENT against experimental studies are realized by correlating rheological parameters used in the proposed drag reduction model to viscous parameters directly measured in the laboratory.
- The proposed RANS model is further used to investigate the interactions between polymer additives and the turbulent flow field in the cylindrical annulus, where the geometrical transverse curvature plays an important role. By analyzing the simulation results of the drag reduction flow field at the same Reynolds number with different rheological parameters, we found that the polymers near the inner and outer walls of the annulus tend to behave differently, leading to relatively more decay of turbulence at the outer wall than the inner. The possible mechanism is suggested to explain such a phenomenon based on the elongation theory of the FENE-P model. Due to the inherent transverse curvature, the outer wall of the cylindrical annular geometry supports more turbulence, resulting in a more chaotic flow field, which has been explained in detail in the Newtonian study of this thesis. Therefore, when the same polymer is added into the flow, its molecules near the

outer wall are stretched more intensely than the inner, leading to more drag reduction behavior. Besides, by changing the rheological parameters of the polymer solutions in this study, the differentiated behavior of polymers in the annulus is also shown to depend on their own rheological properties.

7.2 Future Works

The present research shows how the drag reduction behavior of the polymers can be affected by the geometrical features of the flow pass. Such an effect discussed in this thesis is indirect through the flow field though, it arouses our interests to ask if there could be interactions between the solid surface and polymers that the geometry of the flow pass directly influence the molecular expression of the polymers, for instance, if the flow pass restricts how long the polymer chains can be stretched. This type of interaction is highly possible in microflows, such as the blood flows, where the length scale of the flow pass becomes comparable to the length of the polymers chains. Since the polymer induced drag reduction is potentially a good method to ease high blood pressure [1-3], such investigations are of great importance.

To find out the direct geometrical dependence of polymer behaviors could also advance the research on designing special flow passes that potentially increase drag reduction. Huang et al. [4] have experimentally shown that the drag reduction of surfactant solutions can be enhanced in longitudinal grooved channels. By using the particle image velocimetry (PIV), they explained that the special grooved design helped further decay the near-wall vortices, leading to enhanced drag reduction. However, similar to the present research in this thesis, their study is not able to either support or

oppose the idea that the grooved surface might have directly changed the molecular structure of the surfactant to enhance drag reduction. Therefore if future works can somehow verify this idea, the efficiency of the polymer induced drag reduction in fluid transport industry might be dramatically increased by smart pipeline designs.

Additionally, DNS studies of polymer induced drag reduction in the cylindrical geometries are highly recommended. In the present thesis, due to lack of such DNS databases, the FENE-P based RANS model proposed for modeling drag reduction in the annulus has adopted closures from channel flow, which is inherently not as accurate as the one possibly derived from DNS results from annulus flows. As a result, future DNS studies in this research area will significantly improve the accuracy of RANS modeling for this topic.

Finally, drag reduction in multi-phase flows has promising engineering applications. For example, cutting transports in the drilling system involving multi-phase slurry flow will become more efficient if the friction loss along the wellbore can be reduced by drag reduction techniques. Also, in bioreactors where solid enzymes react dynamically with the liquid broth, proper use of drag reduction techniques can prevent the deactivation of the bio-enzymes by excessive turbulence. While most studies are still focused on single-phase drag reduction, Habla [5] has made great contributions to building a RANS based multi-phase drag reduction model with the open-source software of OpenFoam. It will be beneficial to see similar work fulfilled using ANSYS.

7.3 List of Publications

Peer-reviewed journals:

- Xiong X., Rahman A., Zhang, Y.: RANS based CFD simulation of fully developed turbulent Newtonian flow in concentric annuli, ASME Journal Fluids Engineering, **138**(9), 091202 (2016).
- Xiong X., Zhang, Y., Rahman A: Reynolds-averaged simulation of the fully developed turbulent drag reduction flow in concentric annuli, ASME Journal of Fluids Engineering, **142**(10), 101209 (2020).
- Xiong X., Zhang, Y., Rahman A: Estimation of the polymer induced drag reduction for fully developed turbulent flow in cylindrical geometries using RANS modelling, under review by a peer-reviewed journal.

Conference Proceedings:

- Xiong X., Rahman A., Zhang, Y.: Pressure gradient estimation for two-phase gas/liquid flow in a vertical pipe using CFD, Proceedings of MTS/IEEE OCEANS 14, St. John's, Newfoundland, Canada, September 14-19 (2014).
- Xiong X., Rahman A., Zhang, Y.: Characterization of time-averaged turbulence statistics for shear thinning fluid in horizontal concentric annulus using RANS based CFD simulation, Proceedings of ASME 35th International Conference on Ocean, Offshore and Arctic Engineering, Jun 19-24, Busan, Korea (2016).

7.4 References

1. Abdulbari, H.A., Ling, F.W.: Hibiscus mucilage for enhancing the flow in blood-stream-like microchannel system. *Chemical Engineering Communications* **204**(11), 1282-1298 (2017).
2. Ding, Z., Joy, M., Kameneva, M.V., Roy, P.: Nanomolar concentration of blood-soluble drag-reducing polymer inhibits experimental metastasis of human breast cancer cells. *Breast Cancer: Targets and Therapy* **9**, 61 (2017).
3. Zhang, X., Wang, X., Hu, F., Zhou, B., Chen, H.-B., Zha, D., Liu, Y., Guo, Y., Zheng, L., Xiu, J.: A novel hydrodynamic approach of drag-reducing polymers to improve left ventricular hypertrophy and aortic remodeling in spontaneously hypertensive rats. *International Journal of Nanomedicine* **11**, 6743 (2016).
4. Huang, C., Liu, D., Wei, J.: Experimental study on drag reduction performance of surfactant flow in longitudinal grooved channels. *Chemical Engineering Science* **152**, 267-279 (2016).
5. Habla, F.: Modeling and CFD simulation of viscoelastic single and multiphase flows. Technische Universität München (2015)